

Phenomenological Extension to Black Hole Ringdown

Author:

SPYRIDON THOMOPOULOS

Supervisor

KONSTANTINOS N.
ANAGNOSTOPOULOS

Τομέας Φυσικής

Σχολή Εφαρμοσμένων Μαθηματικών και Φυσικών Επιστημών



Εθνικό Μετσόβιο Πολυτεχνείο

Αθήνα

2024

“Όπου δεν πέφτει φως είναι σκοτάδι,
μα όπου δεν πέφτει σκοτάδι δεν είναι φως.”
- Κ. Μόντης

ACKNOWLEDGMENTS

I would like to express my gratitude to Professors Konstantinos Anagnostopoulos and Harald Pfeiffer for their willingness to serve as supervisor and co-supervisor for this thesis.

Above all, I want to thank Sebastian Völkel. Thanks, for effectively being my supervisor. For always being available for advice and more to that for kindly bringing me to the correct path at times when I had the false impression that everything was going fine. Also, for giving me the opportunity to stay at the Max Planck Institute for Gravitational Physics (Albert Einstein Institute) in Potsdam.

I would like to thank Professor Alessandra Buonanno for visiting her division for the most part of this thesis. This was a very enlightening experience which provided valuable, yet very preliminary, insights on how physics research is carried out and partially dissolved my strong student's naiveness. My thanks also go to Professor Kostas Kokkotas for the kind invitation to his Theoretical Astrophysics Group in Tübingen to present parts of this work.

Finally, thanks to the long anonymous list of people. To fellow students at NTUA that constantly served as bright examples with the admirable persistence and dedication to the understanding of physics. To people unrelated to physics that, unexpectedly, found aspects of the thesis interesting and ignited their curiosity and interesting conversations. To close friends and family for self-explanatory reasons.

ABSTRACT

The recent Gravitational Wave detections provided us with direct observations of Black Hole merger events. The final stage of this merger, known as the ringdown, is the phase in which the remnant Black Hole relaxes to a final stable state. This phase is notably the simplest among all the phase of the merger. However, recent studies on Black Hole ringdown illustrated novel challenges in extracting accurately the parameters from the time-domain ringdown signal. In this thesis, to explore some of the challenges of this method, we firstly apply it to General Relativity cases. Specifically, we evolve the linear perturbation equations for the ringdown of spherically symmetric Black Holes in the time-domain and afterwards, we analyze the results with various models.

With the continuous advancements in gravitational wave detectors, high-precision Black Hole spectroscopy becomes increasingly feasible. Assuming that any deviations from General Relativity, if existent, are small, their impact on the Black Hole spectrum would also be expected to be small. For that reason, a phenomenological extension on the level of the linear perturbation equations was proposed some years ago. This extension does not assume any specific modified theory. However, it can be mapped to modifications predicted by specific theories beyond General Relativity, or be used in a theory-agnostic way. In this thesis, we also examine this extension in the time domain by evolving the linearized modified time-domain equations of spherically symmetric Black Holes. In doing so, the Quasi-Normal Modes are excited, then extracted from the time-domain signal and compared with the theoretical predictions.

ΠΕΡΙΛΗΨΗ

Η πρόσφατη ανίχνευση Βαρυτικών Κυμάτων μας παρείχε άμεση παρατήρηση ενός γεγονότος συγχώνευσης Μελανών Οπών. Το τελικό στάδιο αυτής της συγχώνευσης, γνωστό ως **ring-down**, είναι φάση, κατά την οποία η εναπομείνουσα Μελανή Οπή καταλήγει σε μια τελική σταθερή κατάσταση. Αυτή η φάση είναι η πιο απλή από όλες τις φάσεις της συγχώνευσης. Ωστόσο, πρόσφατες μελέτες πάνω στο **ringdown** των Μελανών Οπών ανέδειξαν νέες προκλήσεις στην ακριβή εξαγωγή των παραμέτρων από το χρονικά εξαρτημένο σήμα **ringdown**. Σε αυτήν την εργασία, για να αντιμετωπίσουμε ορισμένες από αυτές τις προκλήσεις, αρχικά εφαρμόζουμε αυτή τη μέθοδο σε περιπτώσεις Γενικής Σχετικότητας. Συγκεκριμένα, εξελίσσουμε τις εξισώσεις γραμμικής διαταραχής για το **ringdown** σφαιρικά συμμετρικών Μελανών Οπών στο πεδίο του χρόνου και κατόπιν αναλύουμε τα αποτελέσματα με διάφορα μοντέλα.

Με τη συνεχή πρόοδο στους ανιχνευτές βαρυτικών κυμάτων, η υψηλής ακρίβειας φασματοσκοπία Μελανών Οπών καθίσταται ολοένα και πιο εφικτή. Υποθέτοντας ότι τυχόν αποκλίσεις από τη Γενική Σχετικότητα, αν υπάρχουν, είναι μικρές, η επίδρασή τους στο φάσμα των Μελανών Οπών θα αναμενόταν επίσης να είναι μικρή. Για αυτόν τον λόγο, μια φαινομενολογική επέκταση σε επίπεδο των γραμμικών εξισώσεων διαταραχής προτάθηκε πριν από κάποια χρόνια. Αυτή η επέκταση δεν υποθέτει κάποια συγκεκριμένη τροποποιημένη θεωρία. Ωστόσο, μπορεί να απεικονιστεί σε τροποποιήσεις που προβλέπονται από συγκεκριμένες θεωρίες πέρα από τη Γενική Σχετικότητα ή να χρησιμοποιηθεί με θεωρητικά αγνωστικό τρόπο. Σε αυτήν την εργασία, εξετάζουμε επίσης αυτή την επέκταση στο πεδίο του χρόνου, εξελίσσοντας τις γραμμικοποιημένες τροποποιημένες χρονικά εξαρτημένες εξισώσεις σφαιρικά συμμετρικών Μελανών Οπών. Έτσι, οι χαρακτηριστικοί τρόποι ταλάντωσης διεγείρονται, έπειτα εξάγονται από το χρονικά εξαρτημένο σήμα και συγκρίνονται με τις θεωρητικές προβλέψεις.

CONTENTS

Acronyms	1
Thesis outline	3
I Theoretical Background and Methods	5
1 GENERAL RELATIVITY, BLACK HOLES AND GRAVITATIONAL WAVES	7
1.1 Interface Between Old and New Theory	7
1.2 Black Hole Preliminaries	9
1.2.1 Derivation of Spherically Symmetric Metric	9
1.2.2 Singularities	10
1.3 Gravitational Waves	12
1.3.1 Electromagnetic and Gravitational Waves	12
1.3.2 Stages and Regimes of Coalescence	13
1.3.3 Ringdown	15
2 BLACK HOLE PERTURBATION THEORY	17
2.1 Scalar Perturbations	17
2.2 Gravitational Perturbations	21
3 QUASI NORMAL MODES	31
3.1 Normal Modes	31
3.2 Quasi-Normal Modes Definition - Frequency Domain	32
3.3 Time Domain	36
3.4 How to compute Quasinormal Modes	40
3.4.1 Frequency-Domain Integration	41
3.4.2 Time-Domain Integration	41
3.4.3 Continued Fraction	41
3.4.4 WKB Method	42
3.4.5 Inverted Potential	42
4 PARAMETRIZED FRAMEWORK	45
4.1 Motivation	45
4.2 Definition	46
4.3 Examples	49
4.3.1 Example I: Uncoupled Case	49
4.3.2 Example II: Coupled Case - dynamical Chern-Simons gravity	51
5 NUMERICAL TECHNIQUES	55
5.1 Solve the Equations	55
5.1.1 Uncoupled Case: Staggered Leapfrog Method	55
5.2 Fit the Functions	60

II Applications and Results	63
6 APPLICATIONS & RESULTS I	65
6.1 Methods	65
6.2 Pöschl-Teller Potential	71
6.3 Regge-Wheeler Potential	75
6.4 Impact of the Fitting Window End Time	80
7 APPLICATIONS & RESULTS II	85
7.1 Single modification at a time	85
7.2 Multiple modifications at a time	90
Appendix	97
A ADDITIONAL MATERIAL FOR THE EXTRACTED PHASES AND ACCURACY OF THE	97
A.1 Pöschl Teller Potential	97
A.2 Regge-Wheeler potential	97
B ADDITIONAL MATERIAL FOR THE SINGLE K MODIFICATION	99
Extensive Greek Abstract	103
BIBLIOGRAPHY	121

ACRONYMS

AEI	Albert Einstein Institute
BC	Boundary Condition
BH	Black Hole
CFL	Courant-Friedrichs-Lewy
dCS	dynamical Chern-Simons
EFE	Einstein's Field Equations
EP	Equivalence Principle
GR	General Relativity
GW	Gravitational Wave
IC	Initial Condition
LM	Levenberg–Marquardt
NM	Normal Mode
PF	Parametrized Quasi-Normal Mode Framework
PT	Pöschl-Teller
QNM	Quasi-Normal Mode
RW	Regge-Wheeler
SBH	Schwarzschild Black Hole
SSE	Sum of Square Error Function
TA	Theory Agnostic
TS	Theory Specific
WKB	Wentzel–Kramers–Brillouin
PDE	Partial Differential Equation

THESIS OUTLINE

This thesis is organized in two parts. Part I provides the theoretical background mainly for the Quasi-Normal Modes and the techniques employed thereafter. Part II presents the methods used (applied techniques), and the results obtained by them. More specifically:

Part I

Chapter 1: Introduces the key concepts and prerequisites for the following chapters, these are the spherically symmetric Black Hole and Gravitational Waves specifically produced by a binary Black Hole system.

Chapter 2: Provides the derivation of scalar perturbations and an outline of gravitational perturbations around a Schwarzschild Black Hole.

Chapter 3: Provides the definitions of the Quasi-Normal Modes, the properties of the time-domain signal and various ways of computing them.

Chapter 4: Introduces the Parametrized Quasi-Normal Mode Framework for the ring-down, which is a general and phenomenological way to extend the General Relativity Black Hole ringdown and can be mapped to the theory-specific modifications.

Chapter 5: Provides information about the techniques which are applied in Part II, namely, the numerical solution of the wave equation and the fitting of the time-domain ring-down signals.

Part II

Chapter 6: Provides information about the fitting method. Its main part focuses on the first set of results, which involve analysis of waveforms generated by Pöschl-Teller and Regge-Wheeler potentials by adjusting the fitting window that is taken into account. At first we treat only one limit of the window as a free parameter and as a last application we vary both.

Chapter 7: Presents the second set of results involving the Parametrized Quasi-Normal Mode Framework. At first we consider single modifications of $1/r$ powers at a time and consequently multiple modifications simultaneously.

Part I

Theoretical Background and Methods

GENERAL RELATIVITY, BLACK HOLES AND GRAVITATIONAL WAVES

This Chapter provides a brief introduction to some preliminaries for the next parts of the thesis. In Sec. 1.1 we discuss the connection of the old Newtonian theory with General Relativity, in Sec. 1.2 we derive the spherically symmetric solution of the Einstein's Field Equations and discuss about its singularities. Finally, in Sec. 1.3, we discuss about Gravitational Waves and specifically about a multi-messenger detection of a Binary Neutron Star Merger, the various stages of a Binary BH coalescence and we focus on the last, the ringdown.

1.1 INTERFACE BETWEEN OLD AND NEW THEORY

Allgemeine Relativitätstheorie is the state-of-the-art theory of gravity that we currently have. Its foundations were published by Albert Einstein in 1915 in the proceedings of the Prussian Academy of Sciences [1]. Steps towards the experimental verification of General Relativity (GR) came quite early, with the first correct quantitative explanation and prediction of the perihelion precession of Mercury's orbit in 1916, a phenomenon that Newtonian theory could not account for. While this success was a crucial step to validating GR, as expected, it was not enough to dispel all the skepticism at the time [2].

The theory did more than just refining its predecessor. It served as a paradigm shift in our view of gravity. Instead of treating gravity as a force, as the old theory did, Einstein's theory described gravity as the curvature of spacetime. This new perspective fundamentally changed our approach to gravitational phenomena and led to both qualitative and quantitative advancements.

To stress out the magnitude of the shift, consider a historical parallel: the transition from the Ptolemaic geocentric view to the Copernican heliocentric view of the solar system. By degrading Earth from the center of the universe to just a marginal planet, this revolution had profound implications, influencing not only science but also philosophy, religion, political thought, and the arts [2]. In the case of GR, the shift was from the Newtonian consideration of gravity, as an instantaneous and direct force, to the view of gravity as a curvature of spacetime where objects follow paths determined by this curvature. In the new framework, when two bodies interact, one curves the spacetime, while the other is guided from that curvature and vice versa.

The old theory is described by Newton's law of universal gravitation

$$\mathbf{F} = -\frac{Gm_1m_2}{r^2}\hat{e}_{(r)}, \quad (1.1)$$

which provides a radial inverse-square force between two particles with mass m_1 and m_2 . Due to the conservative nature of this force, it can be expressed as a gradient of a gravitational potential Φ which obeys a Poisson equation

$$\nabla^2\Phi = -4\pi G\rho, \quad (1.2)$$

where ρ is the mass density. These equations state that the action of Newtonian gravity is instant and universal, that is, all possible observers sense space and time in the same way; therefore, there is an absolute space and an absolute time.

The equations of motion of the new theory read

$$R_{\mu\nu} - \frac{1}{2}Rg_{\mu\nu} = \frac{8\pi G}{c^4}T_{\mu\nu}. \quad (1.3)$$

On the left-hand side we have the Ricci curvature tensor $R_{\mu\nu}$, the Ricci curvature scalar $R = g^{\mu\nu}R_{\mu\nu}$, and the metric tensor $g_{\mu\nu}$. Ricci tensor and scalar depend on the metric tensor, and the metric shows how the space is deformed due to the presence of mass. On the right-hand side, we have the stress-energy tensor $T_{\mu\nu}$ which describes the distribution and flux of energy and momentum in spacetime. So, objects from differential geometry that describe the curvature are connected with the description of matter. The objective is to solve these equations with respect to the metric tensor and therefore define the spacetime of the system under examination.

One indispensable requirement for GR is that it must reproduce the equations of Newtonian gravity in the weak-field and small velocity regime. The trajectory, called worldline in the new theory, of a free particle moving in a curved spacetime is described by the geodesic equation

$$\frac{d^2x^\mu}{d\tau^2} + \Gamma_{\nu\sigma}^\mu \frac{dx^\nu}{d\tau} \frac{dx^\sigma}{d\tau} = 0, \quad (1.4)$$

where τ is the proper time and $\Gamma_{\nu\sigma}^\mu$ are the Christoffel symbols which are used to generalize derivatives in curved spacetime and are directly related to the metric

$$\Gamma_{\nu\sigma}^\mu = \frac{1}{2}g^{\mu\alpha} (\partial_\nu g_{\alpha\sigma} + \partial_\sigma g_{\alpha\nu} - \partial_\alpha g_{\nu\sigma}). \quad (1.5)$$

In the weak-field and small-velocity regime the geodesic becomes

$$\frac{d^2\vec{x}}{d\tau^2} = -\frac{1}{2}c^2\nabla h_{00}, \quad (1.6)$$

where h is the small correction to the flat metric $g_{\mu\nu} = \eta_{\mu\nu} + h_{\mu\nu}$. So, in order to agree with the old theory, it should be $g_{00} = 1 - 2\Phi/c^2$.

We emphasize that while Newtonian theory agrees with GR within this specific regime, this *does not* imply that the Newtonian theory is simply a subset of GR. The fact that the mathematical equations are the same does not imply that their meaning is the same. One stems from a theory that embeds instant action from a distance and universality of time and space, whereas the other one is based on the equivalence principle. The Einstein equivalence principle consists of three parts. First, it assumes the validity of the equality between the gravitational and the inertial mass, which was already included in Newtonian theory. The other two are related to non-gravitational experiments, stating that their outcome should be independent of the velocity of the freely-falling frame in which they are performed and also independent of its temporal and spatial location in the Universe [3, 4].

1.2 BLACK HOLE PRELIMINARIES

References used for this section: [5–9].

Large enough stars with masses $M \gtrsim 2 - 3M_{\odot}$ can form a Black Hole (BH) during their collapse [10]. These BHs possess a mass and a spin, thus their behavior is described by the Kerr solution [11]. The Kerr hypothesis states that *all* isolated astrophysical BHs can be described by the Kerr solution whose only free parameters are the mass and the spin [12]. This implies that astrophysical BHs are relatively simple objects since they require the specification of only these two parameters in order to be fully described. The purpose of this section is to provide the background for the simpler, non-rotating case of Schwarzschild Black Hole (SBH) that is a preliminary for the next parts of the thesis.

1.2.1 Derivation of Spherically Symmetric Metric

Einstein's Field Equations (EFEs) are non-linear coupled Partial Differential Equations (PDEs) coupling the ten independent components of the metric. Solving these equations reveals how space is structured in the specific configuration being studied. We start from the simplest possible case. That is a spherically symmetric and static spacetime which describes the spacetime *outside* of highly idealized objects such as non-spinning BHs and stars. This solution was derived by Karl Schwarzschild in 1916 [13].

To begin solving the EFE, we guess an ansatz for the metric. By choosing an appropriate coordinate system we can diagonalize the metric, so a reasonable ansatz for symmetric and stationary spacetime¹ would be

$$ds^2 = -A(r)dt^2 + B(r)dr^2 + r^2d\theta^2 + r^2\sin^2\theta d\phi^2. \quad (1.7)$$

¹ Stationary means time independent metric (admitting everywhere a timelike Killing vector field $K: g_{\mu\nu}K^{\mu}K^{\nu} < 0$, which after assigning (t, x_i) coordinates it becomes $K = \partial_t$ or $K^{\mu} = \delta_t^{\mu}$) [7].

Since this metric describes a vacuum solution, it must obey the vacuum Einstein Equation which read

$$R_{\mu\nu} = \partial_\nu \Gamma_{\mu\kappa}^\kappa - \partial_\kappa \Gamma_{\mu\nu}^\kappa + \Gamma_{\mu\kappa}^\rho \Gamma_{\rho\nu}^\kappa - \Gamma_{\mu\nu}^\rho \Gamma_{\rho\kappa}^\kappa = 0. \quad (1.8)$$

Using the Christoffel symbols ², one can calculate the independent components of the Riemann Curvature Tensor, $R_{00}, R_{11}, R_{22}, R_{33}$ ³. By combining R_{00} and R_{11} we find

$$0 = BR_{00} + AR_{11} = \frac{1}{rB}(AB)' \Rightarrow B = \frac{c_1}{A}, \quad (1.9)$$

now from R_{22} we obtain

$$A + rA' = c \Rightarrow A = c_1 \left(1 + \frac{c_2}{r}\right). \quad (1.10)$$

We have specified the solution except for two constants. These can be obtained by the Newtonian limit, by demanding that when gravity is weak, a particle's motion should be the same as if it were moving by the influence of a symmetric mass M in the Newtonian theory. By this demand we get

$$\frac{A(r)}{c^2} = 1 - \frac{2}{c^2} \frac{GM}{r}. \quad (1.11)$$

So $c_1 = 1$ and $c_2 = -2GM/c^2$. Finally, in natural units and expressed in Schwarzschild coordinates, the *Schwarzschild metric* is

$$ds^2 = - \left(1 - \frac{r_H}{r}\right) dt^2 + \left(1 - \frac{r_H}{r}\right)^{-1} dr^2 + r^2 \underbrace{(d\theta^2 + \sin^2\theta d\phi^2)}_{d\Omega^2}, \quad (1.12)$$

where $r_H = 2M$ is the Schwarzschild radius. This will be our concern in the following subsection. From now on, we are going to denote the factor in front of $-dt^2$ as $f(r) = 1 - r_H/r$.

1.2.2 Singularities

There are some peculiar features of the metric (1.12) for $r = r_H$ and $r = 0$. Specifically, for $r = r_H$, the component $g_{11} \rightarrow \infty$ diverges, while for $r = 0$, we observe the divergence of $g_{00} \rightarrow \infty$.

The metric is a geometric object which determines the geometry of the spacetime by defining a distance between two events (points in spacetime). Its components have different expressions depending on the coordinate system that we choose to use. This dependence suggests that the singularities of (1.12) might be artifacts of the chosen coordinates.

² They can be found on pg. 200 of [5].

³ $R_{00} = A''/2B + A'(A'/A + B'/B)/4B - A'/rB, R_{11} = A''/2A - A'(A'/A + B'/B)/4A - B'/rB, R_{22} = 1/B - 1 + r(A'/A - B'/B)/2B$. They can be found on pg. 200 of [5]

Therefore, there might be two types of singularities: *coordinate* (nonphysical) and *curvature* (physical).

An identification of these singularities can be achieved by examining a curvature invariant such as the *Kretschmann scalar*, $K_1 = R_{\mu\nu\kappa\lambda}R^{\mu\nu\kappa\lambda} = 48M^2/r^6$. From this expression, we observe that a divergence at $r = 0$ still exists whereas the other, for $r = r_H$, vanishes. This indicates that the first is a true curvature singularity of the underlying manifold, whereas the second is due to a poor choice of coordinates in which the metric is expressed. In

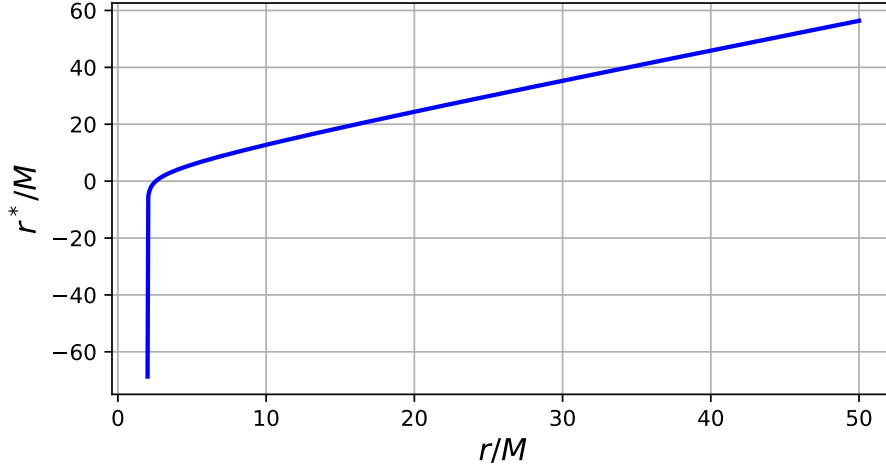


Figure 1.1: Relation between radial r and tortoise r_* for $r > r_H$. Note that the curvature singularity at $r = 2M$ is being mapped to $r_* \rightarrow -\infty$.

simple terms, by changing the coordinate system, one can in principle get rid of the non-physical coordinate singularities. For example, we begin from the transformation $r \rightarrow r_*$ where r_* is given by

$$dr_* = \left(1 - \frac{r_H}{r}\right)^{-1} dr \Rightarrow \quad (1.13)$$

$$r_* = r + r_H \log \left(\left| \frac{r}{r_H} - 1 \right| \right), \forall r \in (0, r_H) \cup (r_H, \infty). \quad (1.14)$$

This expression maps the region outside the Schwarzschild radius from (r_H, ∞) to $(-\infty, \infty)$ and the region inside r_H from $(0, r_H)$ to $(-\infty, 0)$. In other words, it moves the horizon to $-\infty$, as shown in Figure 1.1 for $r > r_H$. This plays a very important role when we want to work numerically on problems defined in that region and will become more obvious in later parts of this thesis. Additionally, it serves as the basis for unveiling some structural properties of Schwarzschild metric. This new coordinate r_* , is called *tortoise coordinate*. The elimination of the $r = r_*$ singularity becomes obvious in the transformed metric.

$$ds^2 = - \left(1 - \frac{r_H}{r}\right) dt^2 + \left(1 - \frac{r_H}{r}\right) dr_*^2 + r^2 d\Omega^2 \quad (1.15)$$

1.3 GRAVITATIONAL WAVES

1.3.1 *Electromagnetic and Gravitational Waves*

Astrophysical objects reveal their properties through various ways, with electromagnetic and gravitational waves being two of the most significant [14]. These two types of waves are fundamentally different, each probing distinct and complementary aspects of the objects under investigation.

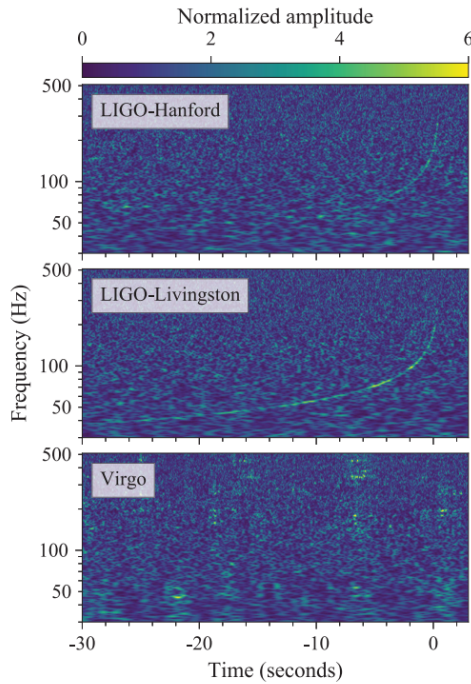
Electromagnetic radiation is emitted by accelerating charged elementary particles such as electrons. Since astrophysical objects are generally electrically neutral, this radiation typically originates from small, localized regions within the object, leading to short wavelengths. Electromagnetic waves, provide detailed information about these localized regions. Also, if they manage to reach the Earth by avoiding absorption or scattering from intervening matter, it is relatively easy to detect since they couple strong enough with electrical charges [14].

In contrast, *GWs* are emitted from the system as a whole, resulting in longer wavelengths. They carry information about the global dynamics and structure of the system. Their weak coupling to matter makes the detection extremely challenging. Once detected, though, they have almost the same waveform as emitted from the source, as their interaction with objects in their journey is weak [14].

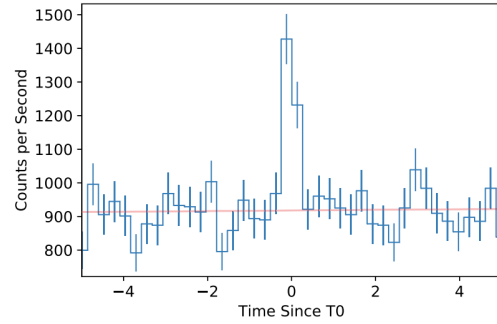
An example of the synergy between these two types of waves is the detection of a Neutron Star Binary, on August of 2017. The LIGO and VIRGO detectors first received the *GW* signal GW170817 and a few seconds later, Fermi Gamma-ray Space Telescope captured the Gamma-ray burst GRB 170817A [15, 16]. Both signals were traced back to the same source due to their similar localization in the sky. Following these, after ~ 11 hours, the *One-Meter, Two-Hemisphere*, collaboration made an optical observation[17]. The optical data, pinpointed the source to the NGC 4993 galaxy located 40 Mpc away from the Earth, a distance that was consistent with the *GW* estimation.

Figure 1.2 shows the detection of GW170817 and its electromagnetic counterparts. In the left panel, time-frequency plots from LIGO and Karga illustrate how the dominant frequencies (indicated in yellow) of the *GW* increase with time as the binary Neutron Stars inspirals inward. The upper right panel displays an ordinary gamma-ray burst detection at ~ 229 eV and the bottom right panel, shows the optical observation, by comparing an image taken four months before the *GW* detection, with one captured ~ 11 h after it.

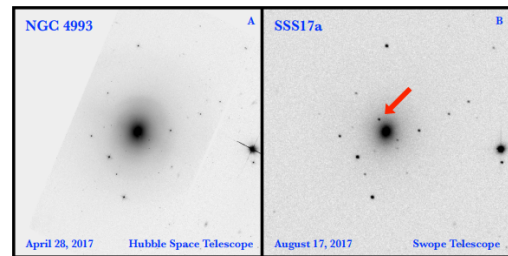
While combining electromagnetic and gravitational wave observations, part of the so-called multi-messenger astrophysics, has proven to be an enlightening approach, not all astrophysical systems emit electromagnetic counterparts. Such a system is the Binary Black Hole Coalescence, which lacks electromagnetic emissions and whose final stage of evolution is the topic of this thesis. Now, let us discuss the *GW* generated by these systems.



Time-frequency plots of the observed GW from the three ground-based detectors (LIGO Scientific Collaboration, Virgo Collaboration, “GW170817: Observation of Gravitational Waves from a Binary Neutron Star Inspiral,” *Phys. Rev. Lett.*, vol. 119, 161101 (2017), [arXiv:1710.05832](#) [gr-qc]. Published under [Creative Commons Attribution 4.0 License](#).) [15].



Gamma-ray burst detection at ~ 229 eV (A. Goldstein et al., “An Ordinary Short Gamma-Ray Burst with Extraordinary Implications: Fermi-GBM Detection of GRB 170817A,” *Astrophys. J. Lett.*, vol. 848, no. 2, p. L14, 2017, doi: [10.3847/2041-8213/aa8f41](#). [arXiv:1710.05446](#) [astro-ph.HE]) [16].



Optical detection, by comparing two images taken before and after the GW detection (D. A. Coulter et al., “Swope Supernova Survey 2017a (SSS17a), the Optical Counterpart to a Gravitational Wave Source,” *Science*, vol. 358, p. 1556, 2017, doi: [10.1126/science.aap9811](#). [arXiv:1710.05452](#) [astro-ph.HE]). Copyright © 2017, American Association for the Advancement of Science. Reproduced with permission.

Figure 1.2: Multi-messenger detection of a Binary Neutron Star System.

1.3.2 Stages and Regimes of Coalescence

Gravitational Waves (GWs) are sourced from various astrophysical processes which can be generally split into two large categories: high and low frequency [18]. Since the frequency of a GW is inversely proportional to the mass of the source, high frequency waves come from light systems and low frequency from more massive ones. High frequency waves can be traced back to supernovae, caused from non spherical collapses of stars, rotating Neutron Stars due to potential small mountains on their surface or small ellipticity that breaks their spherical symmetry, tidal disruption of a Neutron Star that spirals on the field of an other compact object, during the accretion of a white Dwarf to a Neutron Star [18]. Low frequency waves are radiated from more massive non-spherical systems and

are a target group for the LISA detector that will be online in 2035 [19] and focus on the frequency range between 0.1 mHz – 1 Hz [20].

The binaries of the three possible combinations of Neutron Stars and BHs, also belong to one of the two categories depending on the mass of the compact objects. They all consist of the three main stages that are going to be discussed, but with enormous differences on the corrections that have to be included in the waveform in order to describe the process properly. Specifically, systems including Neutron Stars are always more complicated to model, since additional phenomena and properties should be taken into account, such as the internal structure of the neutron star and the aforementioned tidal effects. Also, the complexity increases if the objects are rotating and increases even more if the spins are not aligned and instead, are precessing.

We are going to focus on binary BH coalescence since all the others are beyond the scope of the thesis. It consists of the three stages shown in Figure 1.3 and each stage or different regime of masses and separations is treated with different techniques and methods, as shown in Figure 1.4. The three phases of coalescence are the following

- a) *Inspiral*: This is the earliest stage of the evolution, where the two compact objects have small velocities and large separation, which is gradually shrinking due to loss of energy to GW radiation. As we can see in the blue box of Figure 1.4, the Post-Newtonian analytic approximation is used as a tool to model the waveform on large separations. Within this method, the EFE are expanded around the Newtonian limit in powers of the small parameter $\epsilon \sim v/c$. Each power n , incorporates a new phenomenon in the waveform model, for example, $n = 2$ includes orbit precession, $n = 3$ includes spin-orbit coupling, $n = 4$ spin-spin coupling and GW emission appears for $n \geq 5$. [22–24].
- b) *Merger*: This is the intermediate stage of the evolution. Starts when the separation distance is smaller than the Innermost Stable Circular Orbit and ends when the final remnant is formed. Nonlinearities dominate this phase, and the tools that are used to tackle it are many, as seen in Figure 1.4. Numerical Relativity, a purely numerical treatment of EFE which works better for small and intermediate mass ratios and gravitational self-force perturbation theory, which is employed in large mass ratio regime and takes into account the impact of a small object in its own motion while moving in the field of a massive object [25].
- c) *Ringdown*: This is the last stage of the evolution where one remnant BH is left. Excited from the previous stage, the final object settles exponentially to equilibrium emitting GW in the process. The produced signal is sufficiently described from the complex frequencies called Quasi-Normal Modes (QNMs). We discuss about them more analytically in Chapter 3.

From the techniques shown in Figure 1.4, the Effective One-Body formalism can produce full waveforms and covers a wide area of the parameter space. Initially introduced from Buonanno and Damour in 1998 [26], this method maps the relativistic two body problem

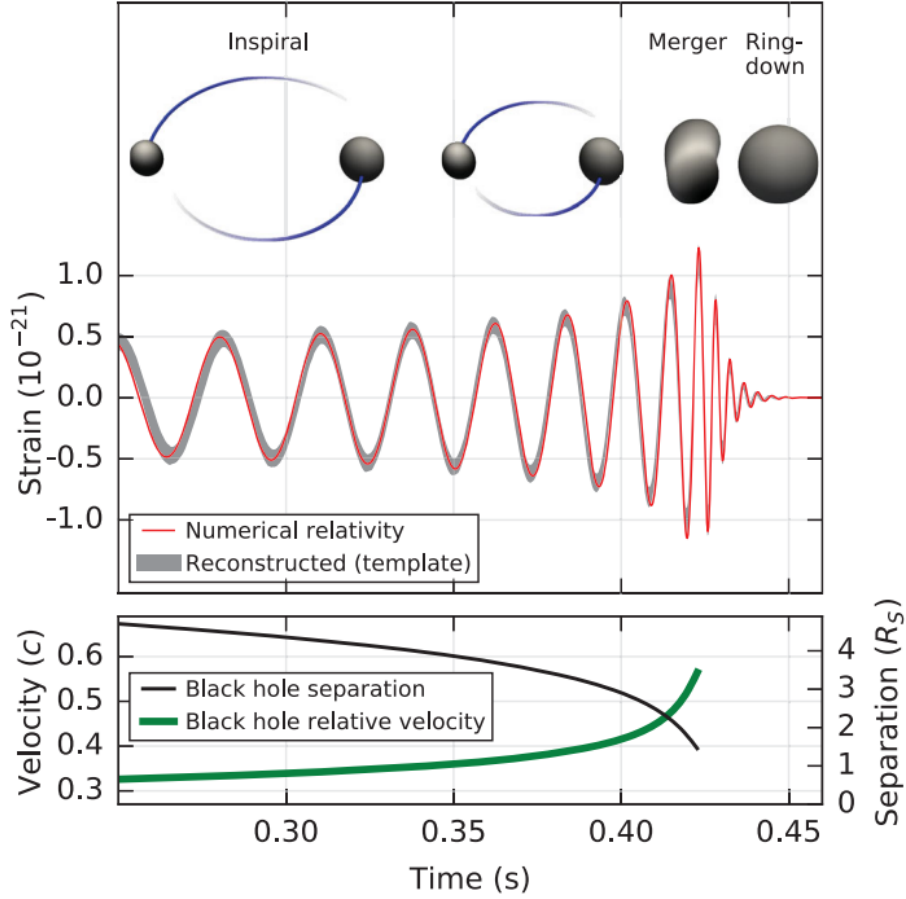


Figure 1.3: **Top:** Stages of the general relativistic two-body problem. **Middle:** Estimated gravitational-wave strain amplitude from GW150914. The peak is reached at the point of merger. **Bottom:** The effective black hole separation in units of Schwarzschild radii R_S and the effective relative velocity of the system (LIGO Scientific Collaboration, Virgo Collaboration, *Observation of Gravitational Waves from a Binary Black Hole Merger*, *Phys. Rev. Lett.* **116**, 061102 (2016), [arXiv:1602.03837](https://arxiv.org/abs/1602.03837) [gr-qc]. Published under [Creative Commons Attribution 4.0 License](https://creativecommons.org/licenses/by/4.0/).) [21].

onto that of a test particle moving in an effective metric, thus providing the waveform in a non-perturbative manner.

1.3.3 Ringdown

The ringdown of a BH can be sufficiently described by an infinite sum of discrete complex frequencies

$$h(t) \simeq \sum_{\ell, m, n} A_{\ell mn} e^{-i(M\omega_{n\ell m}t + \phi_{n\ell m})},$$

where M is the BH mass, $n \geq 0$ is the overtone number, $\ell \geq 0$ is the angular number and $|m| \leq \ell$ is the azimuthal number, fully describing each frequency. This set of frequencies $\omega_{\ell mn}$ is called the *QNM spectrum*. The spectrum carries information about its emitter, and

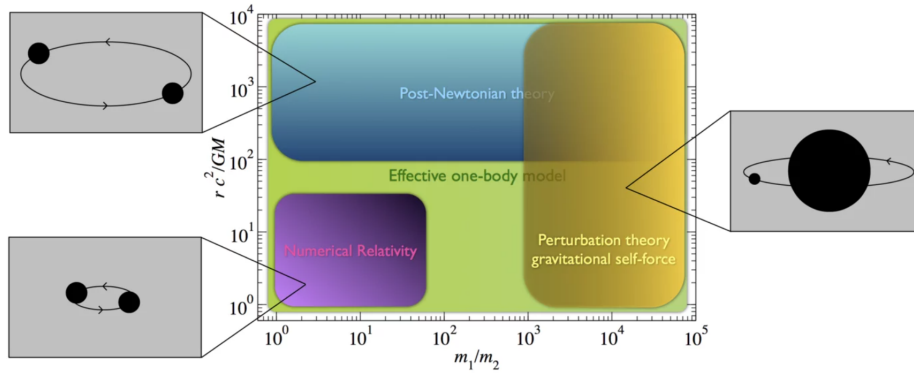


Figure 1.4: Regimes of validity for various methods to tackle the general relativistic two-body problem. (© A. Buonanno, B.S. Sathyaprakash in: "General Relativity and Gravitation: A Centennial Perspective"; Cambridge, University Press (2015). Reproduced with permission of The Licensor through PLSclear) [27]

in our case, if the no-hair theorem holds, it completely describes the properties of the BH, which are its mass, M , and angular momentum, J [28].

The importance of the ringdown phase lies in its ability to offer valuable opportunities for testing GR [28, 29]. However, measuring only the fundamental mode ($n = 0$), is not sufficient to fully determine the angular momentum, J , and the mass, M of the object. This is because different types of objects may have fine-tuned parameters that coincidentally yield the same fundamental mode. On the other hand, if we measure two or more modes from the same object, we can perform a consistency check for GR [28]. By comparing these multiple modes to theoretical predictions, we can verify if they correspond to the same pair of J and M values, as predicted by GR. If there is inconsistency, its source could be either that GR is not the correct description of gravity or that the object is not isolated and there is concentrated mass around it that alters the spectrum.

BLACK HOLE PERTURBATION THEORY

In this chapter, we outline the procedure for deriving the equations that govern small perturbations around a Schwarzschild Black Hole (SBH). We will break the process down into five steps - the first four are related to the mathematical setup, and the last one to the detailed and lengthy calculation. Before diving into the full metric perturbations, however, we begin by tackling a simpler, toy problem: the evolution of a scalar test field on top of a SBH background. This problem serves as a useful starting point, as it leads to an equation that is structurally similar to that for the metric perturbations. By deriving the equation for the scalar field case we will gain intuition for the more complex scenario that follows.

Specifically, in Sec. 2.1 we derive in detail the wave equation that governs the scalar perturbations and in Sec. 2.2 we outline the derivation of the linearized gravitational perturbations around a spherically symmetric spacetime.

2.1 SCALAR PERTURBATIONS

In this section, we aim to study the behavior of a test field on a Schwarzschild background. By *test field*, we mean a field that does not influence the underlying spacetime geometry; instead, it evolves according to how the curved spacetime dictates. To simplify the problem, we will consider the case of a massless, spin-zero field, thus a scalar. The equation of motion can be derived by extremizing the action

$$S = \int dx^4 \sqrt{-g} \mathcal{L}[\Psi, \partial\phi] = \int dx^4 \sqrt{-g} g^{\mu\nu} \partial_\mu \Psi \partial_\nu \Psi,$$

where Ψ is the scalar field and g is the determinant of the metric $g_{\mu\nu}$. By varying this action with respect to Ψ , we obtain the equation of motion, which is the Klein-Gordon equation in curved spacetime [4]

$$\begin{aligned} \square\Psi = 0 &\Rightarrow \nabla_\mu \nabla^\mu \Psi = 0 \Rightarrow \\ \frac{1}{\sqrt{-g}} \partial_\mu (\sqrt{-g} g^{\mu\nu} \partial_\nu \Psi) &= 0. \end{aligned} \tag{2.1}$$

General Spherically Symmetric Background

Instead of deriving the equations directly for the Schwarzschild background, we can start from a more general spherically symmetric metric which has as a specific case the Schwarzschild. The metric, its inverse and its determinant have the structure

$$g_{\mu\nu} = \text{diag}(-A(t, r), B(t, r), r^2, r^2 \sin^2 \theta), \quad (2.2)$$

$$g^{\mu\nu} = \text{diag}(-1/A(t, r), 1/B(t, r), 1/r^2, 1/(r^2 \sin^2 \theta)), \quad (2.3)$$

$$g = -r^4 \sin^2 \theta, \quad (2.4)$$

where if we want to retrieve the Schwarzschild one we can substitute $A(t, r) = A(r) = 1 - r_H/r$ and $B(t, r) = 1/A(r)$. Now we further expand (2.1) using the general metric

$$\frac{1}{r^2 \sin \theta} \partial_\mu \left(r^2 \sin \theta g^{\mu t} \partial_t \Psi + r^2 \sin \theta g^{\mu r} \partial_r \Psi + r^2 \sin \theta g^{\mu \theta} \partial_\theta \Psi + r^2 \sin \theta g^{\mu \psi} \partial_\psi \Psi \right) = 0$$

If we expand the summation on μ we obtain

$$-\partial_t \left(\frac{1}{A} \partial_t \Psi \right) + \frac{1}{r^2} \partial_r \left(r^2 \frac{1}{B} \partial_r \Psi \right) + \frac{1}{r^2 \sin \theta} \partial_\theta (\sin \theta \partial_\theta \Psi) + \frac{1}{r^2 \sin \theta} \partial_\psi \Psi = 0.$$

Assuming spherical symmetry, we split the temporal-radial part of the solution from the angular, $\Psi = \psi(t, r)Y(\theta, \Psi)$

$$\underbrace{-\frac{r^2}{A} \frac{\partial_{tt} \psi}{\psi} + r^2 \frac{\partial_t A}{A^2} \frac{\partial_t \psi}{\psi} + \frac{\partial_r (r^2 \partial_r \psi / B)}{\psi}}_{\ell(\ell+1)} + \underbrace{\frac{1}{Y \sin \theta} \partial_\theta (\sin \theta \partial_\theta Y) + \frac{1}{Y \sin^2 \theta} \partial_\psi \psi Y}_{-\ell(\ell+1)} = 0, \quad (2.5)$$

the equation was further split into two terms. The first (radial) depends only on t, r and the second (angular) on θ, ψ . Therefore each one of them should be constant.

The solution of the angular part, which if further separated leads to a Legendre equation for the θ variable and to a simple harmonic oscillator equation for the ψ part, are the well-know spherical harmonics $Y_{\ell m}$. For the radial part, we can make some first steps without assuming any particular structure neither for A nor B . Initially, we treat them as general as possible, allowing us to derive a broad form of the radial equation. Once the general expression is obtained, we can specify them to match the Schwarzschild metric.

In particular, the radial equation becomes

$$-\partial_{tt} \psi + \frac{\partial_t A}{A} \partial_t \psi + \frac{A}{B} \partial_{rr} \psi + \left(\frac{2A}{rB} - \frac{A \partial_r B}{B^2} \right) \partial_r \psi - \frac{l(l+1)}{r^2} A \psi = 0. \quad (2.6)$$

Now we want to transform the spatial coordinate. When we will specify A, B to the Schwarzschild metric this transformation will help us to eliminate the fictitious singularity that arises from spherical coordinates. In the most general case, it is

$$\frac{\partial r^*}{\partial r} = \Gamma(t, r). \quad (2.7)$$

Using this we can transform the derivatives

$$\partial_r \psi = \frac{\partial r^*}{\partial r} \partial_* \psi = \Gamma(t, r) \partial_* \psi,$$

and

$$\begin{aligned} \partial_{rr} \psi &= \partial_r (\partial_r \psi) \Rightarrow \\ &= \partial_r \Gamma(t, r) \partial_* \psi + \Gamma(t, r)^2 \partial_{**} \psi. \end{aligned}$$

By substituting this transformation into the radial equation (2.6) and by grouping term with same derivative we obtain

$$-\partial_{tt} \psi + \frac{A}{B} \Gamma^2 \partial_{**} \psi + \left(\frac{A}{B} \partial_r \Gamma + \frac{2A}{rB} \Gamma - \frac{\partial_r B}{B^2} A \Gamma \right) \partial_* \psi - \frac{\ell(\ell+1)}{r^2} A \psi = 0. \quad (2.8)$$

We observe that the radial equation is nearly a wave equation with a potential and an extra friction-like term with the first-order derivative which we aim to eliminate. In particular, we can perform a generic decomposition of the ψ function, for example

$$\psi(t, r) := \zeta(r) u(t, r),$$

and then substitute to (2.8). At this point we will have an equation with respect to r^* containing both $u(t, r)$ and the arbitrary function $\zeta(r)$. Thus, we can impose a condition on $\zeta(r)$, which will cancel the first order derivative term.

Following these steps, we have

$$\begin{aligned} \partial_* \psi &= \zeta \partial_* u + u \partial_* \zeta \\ \partial_{**} \psi &= \zeta \partial_{**} u + u \partial_{**} \zeta + 2 \partial_* u \partial_* \zeta. \end{aligned}$$

By substituting in (2.8) we obtain

$$\begin{aligned} -\partial_{tt} \psi + \frac{A}{B} \Gamma^2 (\zeta \partial_{**} u + u \partial_{**} \zeta + 2 \partial_* u \partial_* \zeta) + \left(\frac{A}{B} \partial_r \Gamma + \frac{2A}{rB} \Gamma - \frac{\partial_r B}{B^2} A \Gamma \right) (\zeta \partial_* u + u \partial_* \zeta) - \\ - \frac{\ell(\ell+1)}{r^2} A \psi = 0 \Rightarrow \\ -\partial_{tt} u + \frac{A \Gamma^2}{B} \partial_{**} u + \partial_* u \left(2 \frac{A \Gamma^2}{B} \frac{\partial_* \zeta}{\zeta} + \frac{A}{B} \partial_r \Gamma + 2 \frac{A \Gamma}{rB} - \frac{\partial_r B}{B^2} A \Gamma \right) + u \left(\frac{\partial_* \zeta}{\zeta} \frac{A \partial_r \Gamma}{B} + \right. \\ \left. + \frac{\partial_* \zeta}{\zeta} \frac{2A}{rB} \Gamma - \frac{\partial_* \zeta}{\zeta} \frac{\partial_r B}{B^2} A \Gamma + \frac{A \Gamma^2}{B} \frac{\partial_{**} \zeta}{\zeta} - \frac{\ell(\ell+1)}{r^2} A \right) = 0. \quad (2.9) \end{aligned}$$

If we demand the coefficient of $\partial_* u$ to be zero, we have a differential equation with respect to $\zeta(r)$, assuming that A , B and Γ are known. If we solve it, we obtain the correct transformation which cancels the unwanted first order term and we obtain a wave equation with a potential, for the function $u(t, r)$.

Specification to Schwarzschild Metric

Specifying all the above to the Schwarzschild metric, we have

$$A(r) = f(r) = 1 - \frac{r}{r_H}, \quad (2.10a)$$

$$B(r) = \frac{1}{A(r)} = \frac{1}{f(r)}, \quad (2.10b)$$

$$\frac{\partial r^*}{\partial r} = \Gamma(r) = \frac{1}{A(r)} = \frac{1}{f(r)}. \quad (2.10c)$$

Using the last relation (2.10c) we eliminate the coordinate singularity that arises in spherical coordinates at $r = r_H$. The new spatial coordinate r^* is the *tortoise coordinate* which was introduced in (1.13). The remaining part to fully specify the equation is to obtain $\zeta(r)$. This is achieved by imposing the condition that vanishes the coefficient of the first-order derivative term of the equation (2.9)

$$\begin{aligned} 2\frac{A\Gamma^2}{B}\frac{\partial_*\zeta}{\zeta} + \frac{A}{B}\partial_r\Gamma + 2\frac{A\Gamma}{rB} - \frac{\partial_r B}{B^2}A\Gamma &= 0 \Rightarrow \\ 2\frac{\partial_*\zeta}{\zeta} - \cancel{A^2\frac{\partial_r A}{A^2}} + 2\frac{A}{r} + \cancel{A^2\frac{\partial_r A}{A^2}} &= 0 \xrightarrow{\partial_* \rightarrow \partial_r} \\ \frac{\partial r}{\partial r^*}\frac{\partial_r\zeta}{\zeta} + \frac{A}{r} &= 0 \xrightarrow{\partial_* r = A} \\ \frac{\partial_r\zeta}{\zeta} + \frac{1}{r} &= 0 \Rightarrow \\ r\partial_r\zeta + \zeta &= 0 \Rightarrow \\ (r\zeta)' &= 0 \Rightarrow \\ \zeta(r) &= \frac{1}{r}. \end{aligned}$$

We are able to compute the coefficient of the u term in (2.9):

$$\begin{aligned} \frac{\partial_* f}{f}\frac{A\partial_r\Gamma}{B} + \frac{\partial_* f}{f}\frac{2A}{rB}\Gamma - \frac{\partial_* f}{f}\frac{\partial_r B}{B^2}A\Gamma + \frac{A\Gamma^2}{B}\frac{\partial_{**}f}{f} - \frac{\ell(\ell+1)}{r^2}A \xrightarrow{\partial_* f = A\partial_r f} \\ = -\frac{A}{r}\left(-\cancel{A^2\frac{\partial_r A}{A^2}} + \frac{2A}{r} + \cancel{\frac{\partial_r A}{A^2}A^2}\right) + rA\partial_r\left(A\partial_r\left(\frac{1}{r}\right)\right) - A\frac{\ell(\ell+1)}{r^2} \\ = A\left(-\frac{2A}{r^2} + r\partial_r\left(-\frac{A}{r^2}\right) - A\frac{\ell(\ell+1)}{r^2}\right) \\ = A\left(-\cancel{\frac{2A}{r^2}} - \frac{\partial_r A}{r} + \cancel{2\frac{A}{r^2}} - A\frac{\ell(\ell+1)}{r^2}\right) \\ = -A\left(\frac{r_H}{r^3} + \frac{\ell(\ell+1)}{r^2}\right), \quad (2.11) \end{aligned}$$

and finally, equation (2.9) becomes

$$-\frac{\partial^2 u}{\partial t^2} + \frac{\partial^2 u}{\partial r^{*2}} - \left(1 - \frac{r_H}{r}\right)\left(\frac{\ell(\ell+1)}{r^2} + \frac{r_H}{r^3}\right)u = 0 \quad (2.12)$$

This equation governs the radial part of the solution for scalar test fields in SBH, also known as *master equation*. We will now follow the procedure for the metric perturbations around SBH and as we will see, the master equation the we find is quite similar.

2.2 GRAVITATIONAL PERTURBATIONS

References used for this section: [9, 30].

The question that initiated the study of metric perturbations of Schwarzschild Black Hole (SBH) was whether the spherically symmetric solution of the Einstein's Field Equations (EFE), now known as SBH, is stable [31]. It is important to emphasize that if the SBH was found to be unstable under small perturbations, the arguments supporting the existence of the objects that this solution implies, would have been weakened.

However, in 1957, T. Regge and J.A. Wheeler proved that the SBH is stable under small perturbations. In their seminal work [31], they derived the equation governing the perturbations that have odd parity transformation. Later, in 1970, F.J. Zerilli, derived the equation for perturbations with odd parity transformation [32, 33]. The time gap between these two derivations may serve as a small indicator of the complexity of some steps of these calculations.

In this section, we will outline the procedure for deriving these equations, while providing some calculations when they are feasible by hand in a reasonable length and offering further insights. The main steps for this procedure are the following five:

Step 1: Find a solution, $\bar{g}_{\mu\nu}$ to Einstein's equations, serving as the background space-time

Step 2: Express a new metric in small, perturbations, around the background metric

$$g_{\mu\nu} = \bar{g}_{\mu\nu} + h_{\mu\nu} + \mathcal{O}(h^2),$$

where $|h_{\mu\nu}| \ll |\bar{g}_{\mu\nu}|$

Step 3: Find a good basis to describe the perturbation $h_{\mu\nu}$

Step 4: Choose an appropriate gauge to simplify the equations

Step 5: Plug into Linearized Einstein's Field Equations

Steps 1 & 2

The first two steps have already been already done. For the first one, we assume spherical symmetric system and we obtain the SBH solution that we derived in Section 1.2.1

$$\begin{aligned} \bar{g}_{\mu\nu} &= \text{diag}(-A(r), B(r), r^2, r^2 \sin^2 \theta), \\ A(r) &= \frac{1}{B(r)} = 1 - \frac{r_s}{r}. \end{aligned} \tag{2.13}$$

The second one is just a matter of notation

$$g_{\mu\nu} = \bar{g}_{\mu\nu} + h_{\mu\nu} + \mathcal{O}(h^2), \quad |h_{\mu\nu}| \ll |\bar{g}_{\mu\nu}|,$$

where $h_{\mu\nu}$ is the perturbation metric. From now on, the goal is to find the equations that govern the behavior of the small perturbation on top of our background solution. The next two steps are crucial for simplifying the final equations.

Step 3: Expand into Basis

The idea of choosing an appropriate basis to simplify problems, is already familiar from various areas of physics such as Quantum Mechanics and Electrodynamics. By aligning the choice of basis with the symmetry of the problem, we can often decouple different aspects of the solution, making the problem more tractable.

For example, in the solution of the hydrogen atom, we tried to take advantage of the spherical symmetry of the problem and expressed the wave function as a sum of a radial function multiplied with spherical harmonics. The spherical harmonics are the basis of the angular part of the wave function, whereas by solving for the radial part, we find the associated Legendre polynomials as its basis [34].

Similarly, in electrostatics, we consider a simple example of a conducting charged shell. The electric potential outside the shell, satisfies the Laplace equation. Due to spherical symmetry, again, we expand the solution to a sum of spherical harmonics, multiplied by a factor of the form *(constant) × (powers of r)*. By imposing the boundary conditions, we could obtain the *constant* of the radial part of the solution [35].

The takeaway from these examples is that in problems with spherical symmetry, spherical harmonics naturally appear in the solutions. By imposing boundary conditions, we can determine all the unknown pieces of the expansion. Of course, these are not novel or profound points, but let us try to specify them to our case.

The difference in our expansion from these examples is that they refer to scalar quantities, whereas our case involves tensors. Our task is more complicated. We should not only find a basis for each element of the perturbation tensor $h_{\mu\nu}$ (which is a function), but also a convenient basis for the tensor components themselves. So, we can think that the basis that we seek consists of two parts - basis for the tensor and bases for each tensor element. In that process, we are going to need vector and spin-2 tensor spherical harmonics.

A general way to construct spherical harmonics with spin s , is by coupling the standard scalar spherical harmonics $Y_{\ell\ell_z}(\theta, \phi)$ with the spin function χ_{ss_z} , using the Clebsch-Gordan coefficients [30]. The resulting spin-weighted spherical harmonics can be expressed

$$Y_{jj_z}^{\ell s}(\theta, \phi) = \sum_{\ell_z=-\ell}^{\ell} \sum_{s_z=-s}^s \langle s\ell s_z \ell_z | jj_z \rangle Y_{\ell\ell_z}(\theta, \phi) \chi_{ss_z}, \quad (2.14)$$

when $s = 1$ we construct *vector spherical harmonics* and when $s = 2$ we construct *tensor spherical harmonics*. The Clebsch-Gordan coefficients, couple the angular momentum and

spin states, $|\ell\ell_z\rangle$ and $|ss_z\rangle$, respectively, to create a new state with total angular momentum $|jj_z\rangle$.

The perturbation tensor $h_{\mu\nu}$, being symmetric, has 10 independent components. To take advantage of its spherical symmetry, we can restrict ourselves to the submanifold of the SBH which has t, r constant, leaving only the angular dependence. On this submanifold, different components of $h_{\mu\nu}$ transform differently under rotations. The final expression contains 3 scalar elements (h_{00}, h_{01}, h_{11}), 2 2-dimensional vectors ($h_{0\alpha}, h_{1\alpha}$, for $\alpha = 2, 3$) and one rank two 2-dimensional tensor ($h_{\alpha\beta}$ for $\alpha, \beta = 2, 3$). This structure is a consequence of our choice for the spin function χ_{ss_z} and the final linear combinations of spin-2 spherical harmonics $Y_{jj_z}^{\ell 2}$. There are different possible bases that we can use. One common and convenient choice in General Relativity is the Zerilli tensor harmonics, particularly used in perturbation theory for spherically symmetric spacetimes like Schwarzschild [30].

The scalar ones, are the following three

$$\mathbf{t}_{lm}^{tt} = \begin{pmatrix} 1 & 0 & 0 & 0 \\ 0 & 0 & 0 & 0 \\ 0 & 0 & 0 & 0 \\ 0 & 0 & 0 & 0 \end{pmatrix} Y_{lm}, \quad \mathbf{t}_{lm}^{Rt} = \begin{pmatrix} 0 & 1 & 0 & 0 \\ 1 & 0 & 0 & 0 \\ 0 & 0 & 0 & 0 \\ 0 & 0 & 0 & 0 \end{pmatrix} Y_{lm}, \quad \mathbf{t}_{lm}^{L0} = \begin{pmatrix} 0 & 0 & 0 & 0 \\ 0 & 1 & 0 & 0 \\ 0 & 0 & 0 & 0 \\ 0 & 0 & 0 & 0 \end{pmatrix} Y_{lm}. \quad (2.15)$$

The vector are the following four

$$\mathbf{t}_{lm}^{Et} = \begin{pmatrix} 0 & 0 & \partial_\theta & \partial_\phi \\ 0 & 0 & 0 & 0 \\ * & 0 & 0 & 0 \\ * & 0 & 0 & 0 \end{pmatrix} Y_{lm}, \quad \mathbf{t}_{lm}^{E1} = \begin{pmatrix} 0 & 0 & 0 & 0 \\ 0 & 0 & \partial_\theta & \partial_\phi \\ 0 & * & 0 & 0 \\ 0 & * & 0 & 0 \end{pmatrix} Y_{lm}, \quad (2.16a)$$

$$\mathbf{t}_{lm}^{Bt} = \begin{pmatrix} 0 & 0 & (1/\sin\theta)\partial_\phi & -\sin\theta\partial_\theta \\ 0 & 0 & 0 & 0 \\ * & 0 & 0 & 0 \\ * & 0 & 0 & 0 \end{pmatrix} Y_{lm}, \quad \mathbf{t}_{lm}^{B1} = \begin{pmatrix} 0 & 0 & 0 & 0 \\ 0 & 0 & (1/\sin\theta)\partial_\phi & -\sin\theta\partial_\theta \\ 0 & * & 0 & 0 \\ 0 & * & 0 & 0 \end{pmatrix} Y_{lm} \quad (2.16b)$$

and the tensor are the remaining three

$$\mathbf{t}_{lm}^{T0} = \begin{pmatrix} 0 & 0 & 0 & 0 \\ 0 & 0 & 0 & 0 \\ 0 & 0 & 1 & 0 \\ 0 & 0 & 0 & \sin^2\theta \end{pmatrix} Y_{lm}, \quad \mathbf{t}_{lm}^{E2} = \begin{pmatrix} 0 & 0 & 0 & 0 \\ 0 & 0 & 0 & 0 \\ 0 & 0 & W & X \\ 0 & 0 & X & -\sin^2\theta W \end{pmatrix} Y_{lm}, \quad \mathbf{t}_{lm}^{B2} = \begin{pmatrix} 0 & 0 & 0 & 0 \\ 0 & 0 & 0 & 0 \\ 0 & 0 & -(1/\sin\theta)X & \sin\theta W \\ 0 & 0 & * & \sin\theta X \end{pmatrix} Y_{lm} \quad (2.17)$$

where $X = 2\partial_\theta\partial_\phi - 2\cot\theta\partial_\phi$, $W = \partial_\theta\partial_\theta - \cot\theta\partial_\theta - 1/\sin^2\theta\partial_\phi\partial_\phi$ and the asterisks refer to symmetric parts. We can split these tensor harmonics into two categories regarding their parity transformation $\hat{\mathcal{P}}$

$$\theta \rightarrow \theta - \pi, \quad \phi \rightarrow \phi + \pi. \quad (2.18)$$

The scalar spherical harmonics transform with even parity transformation, $\hat{\mathcal{P}}Y_{\ell m} = (-1)^\ell Y_{\ell m}$. When we extend this to tensor harmonics, each component of the tensor picks an additional (-1) factor for each derivative ∂_i . This leads to both odd and even parity

components. The components with $b = \{Bt, B1, B2\}$ are odd and also called *axial* and the components with $c = \{tt, L0, T0, Rt, Et, E1, E2\}$ are even and also called *polar*. We can now write the perturbation metric separating the temporal-axial from angular part and also split it into axial and polar counterparts

$$\begin{aligned} h_{\mu\nu} &= \sum_a \sum_{\ell m} h_{\ell m}^a(t, r) (\mathbf{t}_{\ell m}^a)_{\mu\nu}(\theta, \phi) \Rightarrow \\ &= \underbrace{\sum_b \sum_{\ell m} h_{\ell m}^b(t, r) (\mathbf{t}_{\ell m}^b)_{\mu\nu}(\theta, \phi)}_{(h_{\text{odd}})_{\mu\nu}} + \underbrace{\sum_c \sum_{\ell m} h_{\ell m}^c(t, r) (\mathbf{t}_{\ell m}^c)_{\mu\nu}(\theta, \phi)}_{(h_{\text{even}})_{\mu\nu}}. \end{aligned} \quad (2.19)$$

In this expression there are three unknown temporal-radial functions for the axial part of the metric and seven for the polar. These functions are to be determined by the [EFE](#). This clear separation into axial and polar contributions not only aids in understanding the structure of the perturbation metric but also indicates that polar and axial solutions are independent and do not couple and mix with each other.

Step 4: Gauge Fixing

As Regge and Wheeler write in their 1957 paper: “Different waves can represent the same physical phenomena viewed in different systems of coordinates” [31]. By this, they mean that [EFE](#), do not have a unique solution. Instead, the solution depends on an arbitrary coordinate transformation. This is analogous to gauge invariance in electrodynamics, where Maxwell’s equations remain invariant under the gauge transformation $V \rightarrow V + \partial_t \Phi$ and $A^\mu \rightarrow A^\mu - \partial^\mu \Phi$, describing the same electrodynamics [35]. By imposing a gauge condition on Φ , we can completely determine the solution in a unique way. The choice of gauge is optimized on the context of the specific details of each problem, with the aim of simplifying the equations as much as possible.

Similarly, the [EFE](#) are gauge invariant under local infinitesimal coordinate transformations of the form:

$$x^\mu \rightarrow x'^\mu = x^\mu + \zeta^\mu(x), \quad (2.20)$$

where ζ^μ is a 4-vector. Under such transformations, the [EFE](#) describe the same gravity. This reduces the number of independent metric components by four.

Quantities that stay numerically invariant under (2.20), are called *gauge-invariants*. In contrast, the metric itself, including its perturbative part, is not a gauge invariant, because it transforms as:

$$h'_{\mu\nu}(x) = h_{\mu\nu}(x) - (\bar{D}_\mu \zeta_\nu - \bar{D}_\nu \zeta_\mu). \quad (2.21)$$

If we expand the second part of this equation in terms of the Zerilli tensor harmonics, by writing ζ^μ in vector harmonics and computing its covariant derivative, then we can impose

four conditions on $\tilde{\zeta}_\mu$, and thus on $h'_{\mu\nu}$, components. The expansion of the transformation 4-vector $\tilde{\zeta}$ consists of two parts: $\tilde{\zeta}^0$ which is a scalar and $\tilde{\zeta}^i$, which is a 3-vector

$$\begin{aligned}\tilde{\zeta}^\mu &= \sum_\ell \sum_{m=-\ell}^m \left(\tilde{\zeta}_{\ell m}^0, \tilde{\zeta}_{\ell m}^i \right) \Rightarrow \\ &= \sum_\ell \sum_{m=-\ell}^m \left(\zeta_{\ell m}^0(t, r) Y_{\ell m}, \left[\zeta_{\ell m}^t(t, r) Y_{\ell m}(\hat{r})_i + \zeta_{\ell m}^E(t, r) \partial_i Y_{\ell m} + \zeta_{\ell m}^B(t, r) (\hat{r} \times \nabla)_i Y_{\ell m} \right] \hat{e}_i, \right)\end{aligned}\quad (2.22)$$

where Einstein's convention is not used on i 's ¹. If we examine the above relation for its parity properties, we can observe that each term with a derivative or \hat{e}_i picks a (-1) factor. Terms with ζ^0, ζ^t and ζ^E correspond to the polar part (even parity) of $\tilde{\zeta}^\mu$ whereas the term with ζ^B corresponds to the axial part (odd parity). So we can split this vector in two $\tilde{\zeta}^\mu = \tilde{\zeta}_{axial}^\mu + \tilde{\zeta}_{polar}^\mu$.

For the axial part of the $\tilde{\zeta}$ 4-vector, we have

$$\tilde{\zeta}_{axial}^\mu = \sum_{\ell=1}^m \sum_{m=-\ell}^m \zeta_{\ell m}^B \left(0, 0, -\frac{1}{\sin \theta} \partial_\phi, \sin \theta \partial_\theta \right) Y_{\ell m}. \quad (2.23)$$

Using the Christoffel symbols ²for the background metric to compute the derivatives of (2.21), it becomes

$$(h'_{axial})_{\mu\nu} = (h_{axial})_{\mu\nu} - \sum_{\ell m} \partial_t \zeta_{\ell m}^B \left(\mathbf{t}_{\ell m}^{Bt} \right)_{\mu\nu} - \sum_{\ell m} \left(\partial_r \zeta_{\ell m}^B - \frac{2}{r} \zeta_{\ell m}^B \right) \left(\mathbf{t}_{\ell m}^{B1} \right)_{\mu\nu} + \sum_{\ell m} \zeta_{\ell m}^B \left(\mathbf{t}_{\ell m}^{B2} \right)_{\mu\nu}. \quad (2.24)$$

Now is the time to fix the gauge in the axial term, which will provide a single gauge condition. The Regge-Wheeler (RW) gauge is chosen with the objective of eliminating terms that involve higher order angular derivatives. In the above equation, if we take into account the definition of tensor spherical harmonics in equations (2.16, 2.17), the coefficient that needs to be eliminated is the one of the term $\mathbf{t}_{\ell m}^{B2}$. This corresponds to the RW gauge condition

$$\zeta_{\ell m}^B = 0. \quad (2.25)$$

The same procedure should be performed for the polar part.

¹ It should be noted that in equation (2.22) the index ℓ on the first summation does not start from the same value for all the terms. For example, it starts from $\ell = 1$ for ζ^E and ζ^B terms, since they are constructed from terms with total angular momentum 1 whereas in the rest start from $\ell = 0$.

² They can be found on pg. 200 of [5].

When we write the axial and polar part of the final perturbation metric, we observe that the conditions for the [RW](#) gauge are the following

$$h_{\theta\phi} = 0, \quad (2.26a)$$

$$h_{\phi\phi} = h_{\theta\phi} \sin^2 \theta, \quad (2.26b)$$

$$\partial h_{t\phi} = -\sin \theta \partial_\theta (h_{t\theta} \sin \theta), \quad (2.26c)$$

$$\partial h_{r\phi} = -\sin \theta \partial_\theta (h_{r\theta} \sin \theta). \quad (2.26d)$$

These relations also provide an easy way to check at any time if we work with [RW](#) gauge. After all the steps, the final form of the axial and polar parts of the metric have the following form

$$(h_{axial})_{\mu\nu} = \sum_{b=Bt,B1} \sum_{\ell m} h_{\ell m}^b (\mathbf{t}_{\ell m}^b)_{\mu\nu} = \sum_{\ell m} \begin{pmatrix} 0 & 0 & h_{\ell m}^{Bt} (1/(\sin \theta) \partial_\phi) & h_{\ell m}^{Bt} \sin \theta \partial_\theta \\ 0 & 0 & h_{\ell m}^{B1} (1/\sin \theta) \partial_\phi & h_{\ell m}^{B1} \sin \theta \partial_\theta \\ * & * & 0 & 0 \\ * & * & 0 & 0 \end{pmatrix} Y_{\ell m} \quad (2.27a)$$

$$(h_{polar})_{\mu\nu} = \sum_{c=tt,L0,Rt,T0} \sum_{\ell m} h_{\ell m}^c (\mathbf{t}_{\ell m}^c)_{\mu\nu} = \sum_{\ell m} \begin{pmatrix} h_{\ell m}^{tt} & h_{\ell m}^{Rt} & 0 & 0 \\ * & h_{\ell m}^{L0} & 0 & 0 \\ 0 & 0 & h_{\ell m}^{T0} & 0 \\ 0 & 0 & 0 & \sin^2 \theta h_{\ell m}^{T0} \end{pmatrix} Y_{\ell m} \quad (2.27b)$$

Step 5: Linearized [EFE](#)

The final step is the most tedious, involving many calculations that we are going to skip here. As someone at the [AEI](#) once remarked, "It might be a good exercise for the soul" when I mentioned I was attempting to do this calculation by hand. We begin by computing the [EFE](#) up to first order with respect to the perturbation metric $h_{\mu\nu}$ and then substitute its expansion in Zerilli tensor harmonics from equation (2.21) and its polar counterpart.

We start from the [EFE](#) in vacuum

$$G_{\mu\nu} = \bar{G}_{\mu\nu} + \Delta G_{\mu\nu} = 0 \Rightarrow \\ \Delta R_{\mu\nu} = 0,$$

where Δ denotes the change (up to linear order) of the corresponding quantity with respect to the background [SBH](#). Now, we can directly use *Palatini's identity*, which reads

$$\Delta R_{\mu\nu} = \Delta \Gamma_{\mu\nu;\alpha}^\alpha - \Delta \Gamma_{\mu\alpha;\nu}^\alpha, \quad (2.28)$$

with

$$\Delta\Gamma_{\mu\nu}^{\alpha} = \frac{1}{2}\bar{g}^{\alpha\gamma}(h_{\gamma\mu,\nu} + h_{\gamma\nu,\mu} - h_{\nu\mu,\gamma}) - \frac{1}{2}h^{\alpha\gamma}(\bar{g}_{\gamma\mu,\nu} + \bar{g}_{\gamma\nu,\mu} - \bar{g}_{\nu\mu,\gamma}). \quad (2.29)$$

The result of this procedure is a set of ten equations, three axial (denoted with -) and seven polar (denoted with +). From these, due to gauge fixing, only six are independent (two axial and four polar). After some manipulations (additions and redefinitions) we are left with the following two wave equations

$$\left(-\frac{\partial^2\Phi_{\ell}^{\pm}(t,r^*)}{\partial t^2} + \frac{\partial^2\Phi_{\ell}^{\pm}(t,r^*)}{\partial r^{*2}}\right) - f(r)V_{\ell}^{\pm}(r)\Phi_{\ell}^{\pm}(t,r) = 0, \quad (2.30)$$

where $f(r) = 1 - r_H/r$ and r^* is the tortoise coordinate (2.7). This equation is called *Regge-Wheeler equation* for axial potential

$$V_{\ell}^{-}(r) = \left(1 - \frac{r_H}{r}\right) \left(\frac{\ell(\ell+1)}{r^2} - \frac{3r_H}{r^3}\right), \quad (2.31)$$

and *Zerilli equation* for polar potential

$$V_{\ell}^{+}(r) = \frac{9\lambda r_H^2 r + 3\lambda^2 r_H r^2 + \lambda^2(\lambda+2)r^3 + 9r_H^3}{r^2(\lambda r + 3r_H)^2}, \quad (2.32)$$

where $\lambda = \ell(\ell+1) - 2$. We should stress that only perturbations with $\ell \geq 2$ lead to gravitational waves. This is because GW are produced by oscillating quadrupole moments and higher, whereas oscillations with $\ell = 0, 1$ refer to spherical and axial symmetric oscillations respectively. Perturbations with $\ell = 0$ refer to a small change of the BH mass and with $\ell = 1$ to a small increase in BH angular momentum.

Despite the substantial increase in complexity, it is noteworthy that the RW potential is quite similar to the one describing scalar perturbations as given in equation (2.12). Actually, it is also similar with the potential emerging from electromagnetic perturbations, and all of these potentials can be written in a compact way:

$$V(r) = \left(1 - \frac{r_H}{r}\right) \left(\frac{\ell(\ell+1)}{r^2} + (1-s^2)\frac{r_H}{r^3}\right), \quad (2.33a)$$

$$s = \begin{cases} 0, & \text{scalar perturbation} \\ 1, & \text{EM perturbation} \\ 2, & \text{axial perturbation} \end{cases} \quad (2.33b)$$

The quantity Φ_{ℓ} of equation (2.30) does not appear directly in the metric, but is connected to it. For example, regarding the axial part

$$\Phi^{-}(t,r) = -\frac{A(r)}{r}h_{\ell m}^{B1}(t,r) \quad (2.34)$$

and regarding the the polar part

$$\Phi^+(t, r) = \frac{1}{\lambda r + 1.5r_H} h_{\ell m}^{T0}(t, r) + \frac{rA(r)}{i\omega(\lambda r + 1.5r_H)} h_{\ell m}^{Rt}(t, r) \quad (2.35)$$

After all, the description of the radial perturbation on top of a Schwarzschild BH reduces to two 1-D wave equations with potentials. These two potentials have very similar qualitative and quantitative characteristics, which is clear even from their plots in Figure 2.1. We are going to discuss some of their properties, similarities, and consequences in the next chapter, but just to give a short preview, they have the same asymptotic behavior, similar maximum value, and position, and produce the same spectrum.

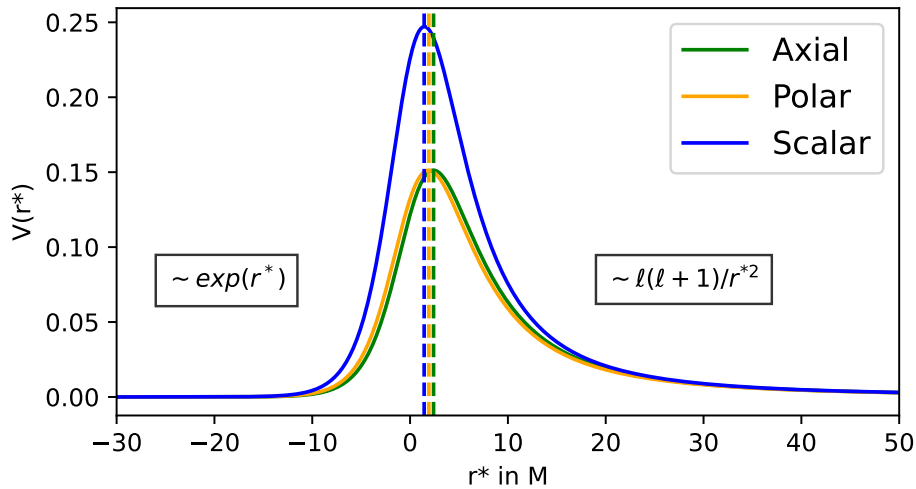


Figure 2.1: Potentials for perturbations with different spin and parity, i.e. scalar, axial and polar with $\ell = 2$. The position of each peak is indicated with the vertical dashed lines. For all of them is around $r^* \sim 3M$.

Using equations (2.30) we can determine the evolution of any initial perturbation by numerically integrating it in the time domain, which was initially done by Vishveshwara in 1970 [36]. This method also offers a straightforward, though not rigorous, way to practically verify that initial data with compact support do not lead to instabilities as shown in Figure 2.2. As a small parenthesis, it is worth noting that the time domain signal consists of three parts, an initial transient one which depends on the initial conditions, a middle one which dominated by exponentially damped oscillations, and the late-time part characterized by a power-law tail. We will discuss these properties further in the next chapter.

A bit better argument regarding the stability, but still quite naive, was given again by Vishveshwara in 1970 [37]. He assumes just imaginary frequency $\omega = i\alpha$, which results in a time dependence of the form $\sim \exp(\alpha t)$, leading to exponential divergence with time. If this assumption leads to inconsistencies, there cannot exist solutions with imaginary frequencies and thus, finite initial data can only produce bounded solutions.

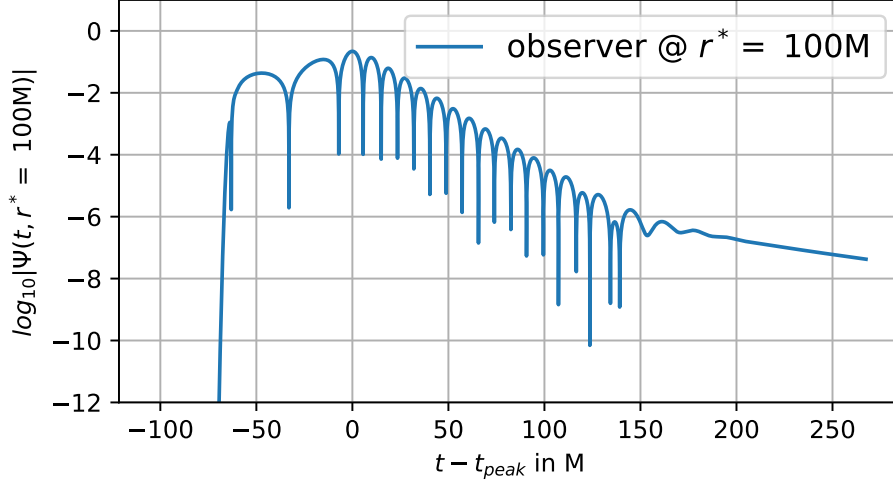


Figure 2.2: Time evolution of equation (2.30) with Gaussian initial data as seen from an observer at fixed position $r^* = 100M$

The asymptotic behavior of the solution, he states, is $\Phi \sim \exp(\pm\alpha r^*)$ at spatial infinity, $r^* \rightarrow +\infty$, and at the horizon, $r^* \rightarrow -\infty$. To preserve asymptotic flatness, we have to choose the negative sign for spatial infinity,

$$\Phi_{+\infty} \sim \exp(-\alpha r^*),$$

and to avoid divergence at the horizon in tortoise coordinates, we must choose the positive sign, which asymptotically leads to $\Phi_{+\infty} \rightarrow 0$. Since all the potentials (2.33), (2.32) are positive, by substituting the temporal part in the wave equation, we obtain

$$\frac{d^2\Phi_{\pm}(r)}{dr^2} = (\alpha^2 + V^{\pm}(r))\Phi_{\pm}.$$

We infer that the second derivative $d^2\Phi_{\pm}/d^2r^*$ will be positive for all of these cases. Therefore, the finite solution at spatial infinity cannot be matched smoothly to the finite solution at the horizon. To match with the asymptotic expression for $r^* \rightarrow$, the solution should behave as

$$\Phi_{-\infty} \sim \exp(-\alpha r^*),$$

which diverges. This divergence can be related to the metric via the equation (2.34)

$$h_{\ell m}^{B1}(r \rightarrow +\infty) = -\frac{r}{A(r)}\Phi_{-\infty}^- \sim -\frac{r}{A(r)}\exp(-\alpha r^*) \Big|_{-\infty} \rightarrow +\infty.$$

Such a divergence contradicts the assumption of $h_{\mu\nu}$ being small. thus ruling out the possibility of an exponentially growing solution for the axial sector of the perturbation equations.

The fact that initial data with compact support do not lead to an exponentially growing solution, but instead, to bounded ones was shown rigorously in [38]. Now that we are confident about the sane and non-explosive behavior of our SBH under a small perturbations,

we can study its time evolution, but before doing so, let us discuss some properties of the equation also in the frequency domain.

Chapter Summary

For spherically symmetric Black Holes we discussed:

- the derivation of scalar and gravitational (axial and polar) perturbations,
- scalar and gravitational perturbation are described by a wave equation with qualitatively similar potentials, with peaks $\sim 3M$ and same asymptotic behavior,
- all these three perturbations are stable and do not diverge as a function of time, indicating that the background spherically symmetric spacetime is stable.
- The time domain signal consists of the transient phase, the oscillating phase and the power-law tail.

QUASI NORMAL MODES

Time and frequency domain study are the two ways of examining the properties of equation (2.30). Each approach has its advantages and disadvantages and can be used to reveal different properties of the Black Hole (BH) ringdown.

A time-domain study of the linear equation reveals the dynamic evolution of an initial wave packet and the response of the BH to it. In this way, it raises questions regarding the the number of overtones that can be fitted, or how well we can extract the parameters that describe the signal, or when the linear signal is described well by superpositions of Quasi-Normal Modes [39–41].

In contrast, a frequency-domain study is useful for defining the Quasi-Normal Modes (QNMs)s and investigating the intrinsic properties of the object [42].

The significance of QNMs lies in the fact that they encode the identity of the underlying object. If the Kerr hypothesis holds, knowing the QNM spectrum allows us to extract information about the object’s mass and spin, and consequently fully determine its parameters [12].

Specifically, in Sec. 3.1 we provide intuition about QNMs by comparing them to Normal Modes (NMs) and in Sec. 3.2 we provide definitions about the QNMs. In Sec. 3.3 we provide details about the time domain study, which is the one employed in this thesis and in Sec. 3.4 we outline some common methods that are used to compute QNMs.

3.1 NORMAL MODES

We shall start by providing a bit of intuition about QNMs, even before formally defining them. To simplify the explanation, let’s start by removing the "Quasi" and discuss about NMs. We encounter them in all sorts of physical systems, from simple mechanical systems, to vibrating strings, to crystal lattices, thus they serve as a good ground point.

We stick to a vibrating string, since it is closer to our problem. The equation that describes this system both in time and in frequency domain (after a *Fourier Transformation*) is

$$\frac{T}{\rho} \frac{\partial^2 \Phi(t, x)}{\partial x^2} - \frac{\partial^2 \Phi(t, x)}{\partial t^2} = 0 \xrightarrow{\text{F.T.}} \quad (3.1a)$$

$$\frac{d^2 \hat{\Phi}(x)}{dx^2} = \omega^2 \frac{\rho}{T} \hat{\Phi}(x). \quad (3.1b)$$

where T is the tension and ρ the density of the string.

By imposing Boundary Conditions (BCs) to equation (3.1b), for example Dirichlet, Newman, mixed, we define an infinite number of distinct eigenvalues of the operator d^2/dx^2 , which correspond to the NM, denoted as ω_n .

Additionally, by specifying Initial Conditions (ICs) for equation (3.1a), that is, values at $t = 0$ for the solution $\Phi(t = 0, x)$ and its derivative $\partial_t \Phi(t = 0, x)$, we can express the general solution of the equation as a sum of NMs

$$\Phi(t, x) = \sum_{n=0}^{\infty} c_n e^{i\omega_n t} \Phi_n(x). \quad (3.2)$$

We should highlight the fact that the NM spectrum emerges from the intrinsic properties of the underlying system which fully describe it. In the case of the 1-D string, these properties are the BCs, the tension, the density, and, in extension, any potential that could be applied to it [43].

However, there are fundamental issues associated with the kind of problems where the spectrum is known but the parameters describing the source are to be found, also known as inverse problems. For example, the spectrum of a 2-D oscillating membrane does not correspond to a unique shape, rather, a given spectrum can be traced back to an infinite number of different membrane shapes. This is implied by the phrase "Can one hear the shape of a drum?" [44].

In contrast, the amplitudes c_n do not reflect fundamental properties of the system; instead they are a consequence of the ICs and indicate how much a specific mode from the spectrum is excited. Therefore, if one wants to study the system's identity and properties, one should study equation (3.1b) and if one wants to understand how these properties evolve over time, one should study equation (3.1a).

The NM expansion provides a complete set of functions, implying that at any time t , the solution can be reproduced by summing over NM for all x . In addition, the eigenvalues ω_n are real, which means that there is no energy escaping from the boundaries or dissipation, which corresponds to an idealized system. In a more realistic situation some form of dissipation would occur, for example, friction between the string and the mechanism holding the boundaries. This would introduce damping to the modes, causing ω_n to become complex numbers. The damping could be explained by microscopically examining the interaction between the string and the boundaries. These complex modes are called Quasi-Normal Modes (QNMs).

3.2 QUASI-NORMAL MODES DEFINITION - FREQUENCY DOMAIN

Intuitively, from the previous section, we know that the QNMs are the complex frequencies of a system, having both oscillatory (real) and dissipative (imaginary) parts, that potentially fully characterize it. Similarly to NM, they are said to be the fingerprints of the underlying system and specifically in our case of the BH.

There are different ways to properly define the QNMs. The most common one is through the frequency domain of equation (2.30). Generally speaking, one can transform time do-

main to frequency domain with many different transformations. The two most commonly used in QNM literature are the *Fourier Transformation* and the *Laplace Transformation* [42, 45]. An other definition involves scattering amplitudes.

Definition I: Fourier Transformation

The *Fourier Transformation*¹ of (2.30) leads to a Schrödinger-like equation

$$\frac{d^2 \hat{\Phi}_\ell^\pm(r^*)}{dr^{*2}} + (\omega^2 - V_\ell^\pm(r)) \hat{\Phi}_\ell^\pm(r^*) = 0. \quad (3.3)$$

The limits of the potentials at the horizon and in the region of spatial infinity are zero, $V_\ell^\pm(r^* \rightarrow \pm\infty) \rightarrow 0$. This leads to a harmonic oscillator equation

$$\frac{d^2 \Phi_\ell^\pm(r^*)}{dr^{*2}} + \omega^2 \Phi_\ell^\pm(r^*) \simeq 0. \quad (3.4)$$

As a result, the possible physical solutions are

$$\Phi_\ell^\pm \sim e^{+i\omega r^*}, \quad r^* \rightarrow +\infty, \quad (3.5a)$$

$$\Phi_\ell^\pm \sim e^{-i\omega r^*}, \quad r^* \rightarrow -\infty. \quad (3.5b)$$

These correspond to outgoing waves at spatial infinity and ingoing waves at the horizon². Had we taken the opposite signs, it would imply incoming waves from infinity or outgoing waves from the horizon, which means that the horizon has reflectivity. The first is non-physical, while the second is non-physical in classical terms.

If we impose (3.5) as BCs on equation (3.3) we obtain a boundary value problem whose eigenvalues are the complex frequencies $\omega = Re(\omega) - iIm(\omega)$, the Quasi-Normal Modes. We note that in order to avoid exponential growth, which we excluded in section 2.2, we expect $Im(\omega) > 0$.

The fact that they are complex is a consequence of the complex BCs [30]. This complex nature indicates that there is dissipation in the system, leading to energy loss. The dissipation cannot be traced back to a microscopic mechanism, as could for mechanical systems, so the relaxation of an oscillating BH to equilibrium is its intrinsic property.

An important property of the spectrum emerging from the two gravitational potentials is that the potentials are isospectral, meaning that they have exactly the same QNM spectrum. It was firstly found by Chandrasekhar in 1985 [46]. In mathematical terms this implies that if the even-parity equation (3.3) can be written as $\hat{L}^+ \Phi^+ = \omega^2 \Phi^+$, then the odd-parity one can be expressed as $\hat{L}^- F(\Phi^-) = \omega^2 F(\Phi^-)$, where F we denotes that the new eigenfunction is not directly Φ^- but a function of it. Therefore, the two potentials

¹ We define the Fourier Transform as $\hat{\Phi}_\ell^\pm(\omega, r^*) \equiv \hat{\Phi}_\ell^\pm(r^*) = \int_{-\infty}^{+\infty} \Phi_\ell^\pm(t, r^*) e^{-i\omega t} dt$. Alternatively, we may obtain (3.3) by simply substituting $\Phi_\ell^\pm(t, r^*) \rightarrow e^{-\omega t} \hat{\Phi}_\ell^\pm(r^*)$ into (2.30).

² This is even more clear if we multiply with the corresponding time factor $e^{-i\omega t}$. The spatial infinity term becomes $\sim e^{+i\omega(r^*-t)}$ which implies outgoing waves and the horizon term becomes $\sim e^{-i\omega(r^*+t)}$, which implies left moving, thus ingoing waves.

posses the same set of eigenvalues which they correspond to different eigenfunctions [30, 47].

However, from this definition a problem rises. We can express (3.5) more compactly as $\Phi_\ell^\pm \sim e^{i\omega|r^*|} = e^{+i\text{Re}(\omega)|r^*|} \cdot e^{+Im(\omega)|r^*|}$. Therefore, as we take $r^* \rightarrow \pm\infty$, the solution diverges. Does this divergence imply that each QNM carries infinite energy? The answer is negative. The reason is that QNMs, as can also be seen in Figure 3.1, are localized to a finite and small region of space. They could occupy all space, thus diverge, only if they had existed for all time. That is, because each QNM excitation from the initial pulse happens at a specific and finite time interval and also the excitation signal decays exponentially in time [42]. To take into consideration the initial pulse we should turn to Laplace Transformation.

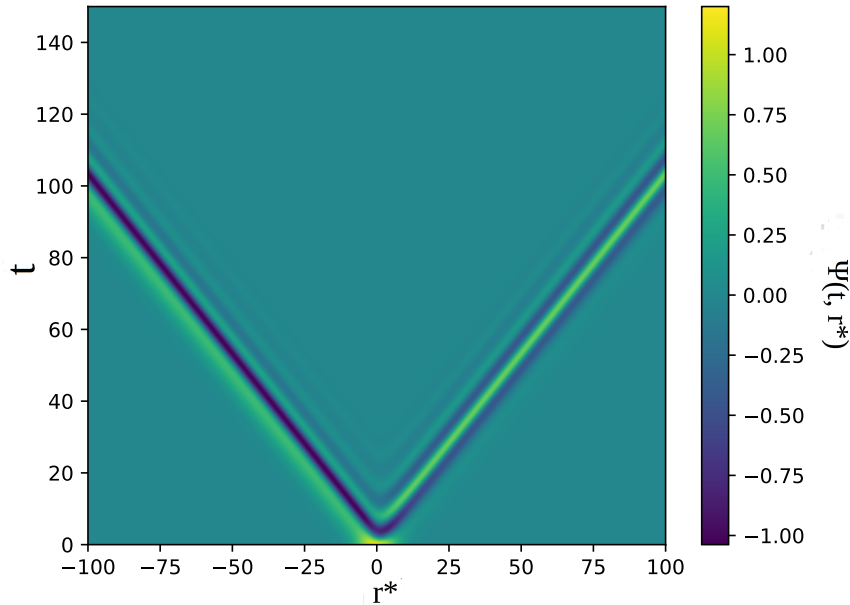


Figure 3.1: The evolution of an initial Gaussian profile propagated towards both directions. We observe that the divergence of the QNMs coming from the $e^{+Im(\omega)|r^*|}$ term as implied by equations (3.5), is suppressed when we add the time dependence $e^{+Im(\omega)(|r^*|-t)}$ and the total solution remains local in space and finite.

Definition II: Laplace Transformation

The Laplace Transformation³ also leads to an ordinary differential equation, although it takes into account the Initial Conditions of the wave equation, providing a more robust way to define the QNMs. The transformed equation reads:

³ The Laplace Transformation is defined as $\hat{\Phi}_l^\pm(s, r^*) \equiv \hat{\Phi}_l^\pm(r^*) = \int_{0^+}^{+\infty} \Phi_l^\pm(t, r^*) e^{-st} dt$.

$$\frac{d^2\hat{\Phi}(s, r^*)}{dr^{*2}} + (-s^2 - V(r^*)) \hat{\Phi}(s, r^*) = \underbrace{-s\Phi(t, r^*)|_{t=0} - \frac{\partial\Phi(t, r^*)}{\partial t}|_{t=0}}_{\mathcal{J}(s, r^*)}, \quad (3.6)$$

where $s = \sigma + i\omega$. This procedure reveals a lot more novel points and details than the previous one, delivering for that reason more insights and deeper understanding to the problem. We will only stick to the extremely main points.

The solution of the inhomogeneous equation (3.6) can be formally expressed in terms of the Green's function $G(s, r^*, r^{*'})$

$$\hat{\Phi}(s, r^*) = \int_{-\infty}^{+\infty} \mathcal{J}(s, r^*) G(s, r^*, r^{*'}) dr^{*'} . \quad (3.7)$$

The crucial step is to invert the transformed solution and find Φ from $\hat{\Phi}$ [42]. If \mathcal{J} has no singularities inside the chosen contour of integration, then the QNMs are defined as the poles of the Green's function. By applying the residue theorem, we observe that these poles contribute to the inverse transformation, thus define the solution

$$\begin{aligned} \Phi(t, r^*) &= \frac{1}{2\pi i} \oint ds e^{st} \int_{-\infty}^{+\infty} \mathcal{J}(s, r^*) G(s, r^*, r^{*'}) dr^{*'} \Rightarrow \\ &= \frac{1}{2\pi i} \sum_n \text{Res} \left(e^{st} \int_{-\infty}^{+\infty} \mathcal{J}(s, r^*) G(s, r^*, r^{*'}) dr^{*'}, s_q \right). \end{aligned} \quad (3.8)$$

Since \mathcal{J} is analytic within the curve of integration, the only term that contributes to the summation of equation (3.8) is the Green's function.

The contribution to the inverse integral comes from three main sources, as we discussed with Figure 2.2: (a.) the directly transmitted wave from the source to the observer, primarily related to the IC, (b.) the BH response to the IC, which is dominated by the QNMs, and (c.) the backscattering of the signal due to the asymptotic behaviour of the potential. This, causes a late-time power-law tail that we will discuss later [48].

Definition III: Scattering Amplitude [30]

This definition of QNMs is more closely related to the time domain, which is the focus of this thesis. At spatial infinity and at the horizon $|r^*| \rightarrow +\infty$, the potential vanishes. Therefore, the solution can be expressed as a sum of all possible frequencies, similar to approaches in Classical Field Theory and Quantum Mechanics.

If we begin with an initial wavepacket at spatial infinity, part of it will be reflected while another part will be transmitted due to the potential barrier. Consequently we have the following asymptotic solutions

$$\Phi(t, r^*) \simeq A_0(\omega) e^{-i\omega r^*} + A_r(\omega) e^{+i\omega r^*}, \quad r^* \rightarrow +\infty \quad (3.9a)$$

$$\Phi(t, r^*) \simeq A_t(\omega) e^{-i\omega r^*}, \quad r^* \rightarrow -\infty \quad (3.9b)$$

The scattering amplitude, defined as the ratio of the final reflected amplitude over the initial amplitude in a region of space where the potential is practically absent, is given by

$$S(\omega) = \frac{A_r(\omega)}{A_0(\omega)}. \quad (3.10)$$

This quantity can be defined due to the conservation of probability $|A_0|^2 + |A_r|^2 = |A_t|^2$.

Taking into account the BC from equations (3.5), there should be $A_0(\omega) = 0$ and simultaneously $A_r(\omega) \neq 0$. It is important to note that $A_0(\omega)$ cannot be equal to zero for all frequencies, thus the QNMs are the discrete frequencies that satisfy this condition. In other words, the QNMs correspond to the poles of the scattering amplitude.

3.3 TIME DOMAIN

The time evolution of linear perturbation equations provides valuable insights to the study of oscillating BHs. This method typically involves analyzing the scattering of an initial Gaussian wavepacket, evolved according to a wave equation, after its interaction with various potential barriers. These barriers correspond to different types of perturbations, as discussed in Chapter 2.

Vishveshwara first used this method in 1970 [36], where he presented an expected result, that if the initial Gaussian is too narrow it penetrates the RW potential whereas if it is too wide, it is fully reflected and the reflection coefficient approaches one.

The main limitation of this method is its inability to robustly extract the overtones. This is due to their significantly larger imaginary part than the fundamental mode ($\gtrsim 3$ times larger for the first overtone and even larger for the others). As a result they die a lot faster (at least $\gtrsim e^3$ times), and the majority of the time-domain signal, especially for late times after the peak, is dominated by the fundamental mode. However, different techniques yield varying number of extracted overtones and the discussion on how many modes one can extract from the ringdown signal is still ongoing [40, 41].

To start further exploring this method, which is the method that we implement in this thesis, we write again the wave equation together with its outgoing BC and its IC

$$-\frac{\partial^2 \Phi_\ell^\pm(t, r^*)}{\partial t^2} + \frac{\partial^2 \Phi_\ell^\pm(t, r^*)}{\partial r^{*2}} - V_\ell^\pm(r) \Phi_\ell^\pm(t, r^*) = 0 \quad (3.11a)$$

$$\text{(BC)} : \begin{cases} \Phi_\ell^\pm \longrightarrow e^{+i\omega(r^*-t)}, & r^* \rightarrow +\infty \\ \Phi_\ell^\pm \longrightarrow e^{-i\omega(r^*+t)}, & r^* \rightarrow -\infty \end{cases} \quad (3.11b)$$

$$\text{(IC)} : \begin{cases} \Phi_\ell^\pm(t=0, r^*) = h(r^*) \end{cases} \quad (3.11c)$$

Most usually, the IC are chosen as follows: Gaussian profile for the initial function, $h(r^*) = A \cdot \exp(-0.5(r^* - \mu)^2/\sigma^2)$ and for the initial derivative either $g(r^*) = 0$ which splits the Gaussian into two or $g(r^*) = \pm \partial_r^* h(r^*)$ which correspond to advection equations, that

cause the Gaussian to start moving either to the left or to the right, depending on whether the sign is negative or positive, respectively.

To study the problem and obtain useful information, we need to extract the time-domain signal. We consider a fixed position and record the waves that pass through this location. In other words, we place an observer at $x_{obs} = R$ and examine the data that the observer sees, as illustrated in the upper panel of Figure 3.1. The observer captures the impact of the potential on the initial data. It is, therefore, important to position the observer sufficiently far from the potential, ideally at spatial infinity, so that the effect of the potential on the waves has ceased.

The recorded signal can be seen at the bottom panel of Figure 3.1. As evident, it can be divided into three phases: the transient phase (gray shaded), the damped oscillatory phase (green shaded), and the late-time power-law tail (red shaded). It is important to note that contributions coming directly from the initial data (without interaction with the potential) can contaminate the signal. However, these contributions can be mitigated by applying an advection equation as Initial Condition to the time derivative, as discussed earlier.

Among the three phases, the first one is insignificant - it depends only on the initial data and does not impact the subsequent phases of the signal. This phase is where the oscillations build up and it terminates at the peak. The second phase is expected to be described, either partially or fully, by the QNMs. The last one follows a power-law whose exact form depends on the initial data and the asymptotic form of the potential. We will now elaborate on these points in more detail.

A question that arises from the above is whether the QNMs form a complete basis which can be used in superposition to fully describe the time-domain signal. Completeness has many definitions but based on one provided in reference [50], it means that the time-domain signal can be expressed as a sum over the QNMs: $\sum_n c_n f_n(r^*) e^{-\omega_n t}$. The indications we have so far, however, are against completeness. At the transient part, the oscillations are building up and reasonably, QNMs cannot describe parts of the signal in which they do not exist, so we should exclude this part and discuss about the completeness for the other two.

First of all, we note that QNMs are infinite in number which is a necessary condition to form a complete basis [42, 45, 51]. However, in reference [50] certain connections between the completeness of the QNM spectrum and the properties of the potential are proposed. One of them is that the potential is everywhere finite and at $|r^*| \rightarrow +\infty$ vanishes rapidly. By "vanishes rapidly" practically is implied that it possesses no power-law tails and mathematically is meant that it should be decaying at least exponentially fast

$$\int_0^{+\infty} r^* e^{\alpha r^*} |V(r^*)| dr^* < +\infty, \quad \forall \alpha \geq 0. \quad (3.12)$$

The second connection they provide, is that if the potential's spectrum is not complete, it can be made complete by introducing a small discontinuity on the potential.

The reason for the incomplete description of the linear BH ringdown from the QNMs lies in the presence of the power-law tail at late times. Price first described their form [52].

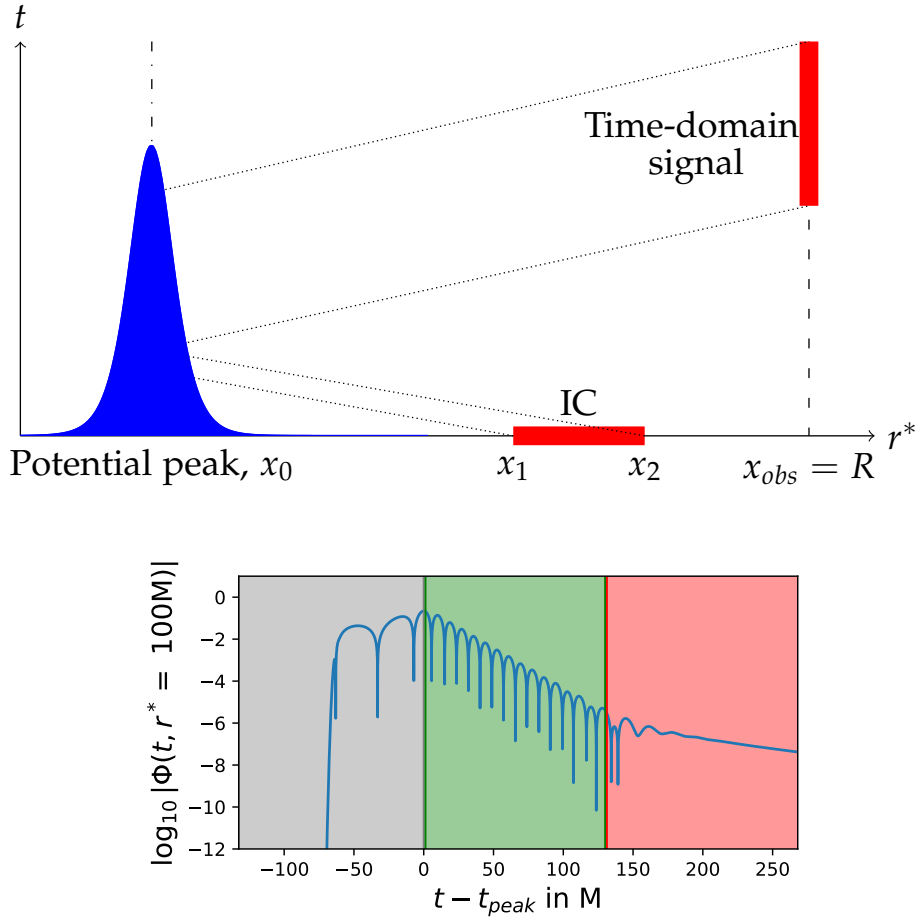


Figure 3.1: **Top:** Schematic explanation of the study in the time domain (inspired by the reference [49]). **Bottom:** Time-domain signal for Axial potential as seen by the observer. The different regions: transient (gray), QNM dominance (green), and late-time tail (red) are also shown.

Their source is the asymptotic behavior of the potential. If the potential does not decrease fast enough, some back-scattering of the waves is present and produces the tails according to the power-law

$$\Phi(t, r^* = R) \sim t^{-(2\ell+P+1)}, \quad (3.13)$$

where $P = \{1 \text{ if } \partial_t \Phi(0, r^*) = 0 \text{ and } 2 \text{ otherwise}\}$ and ℓ is the multipole number. This behavior is the same for scalar and gravitational fields. Furthermore, there are more general studies that relate the asymptotic behavior of the term accompanying the centrifugal one ($\sim 1/(r^*)^2$), which for RW potential is $\sim 1/(r^*)^3$, to the late-time behavior of the signal [53].

All gravitational potentials shown in equation (2.33) do not satisfy equation (3.12) meaning their post-peak signal cannot be completely described as a superposition of QNMs. Therefore, they do not constitute a complete set. Nevertheless, we can make a weaker

statement, that the signal, excluding the transient part, can be approximated quite well by the QNMs [45]

$$\left| \Phi(t, r^* = R) - \sum_{n=0}^N a_n e^{\omega_n(t-r^*)} \right| < C e^{((-a_{N+1} + \epsilon)t)},$$

where C is a constant. So, QNMs can approximate the extracted signal at sufficiently late times.

The ultimate goal of the time domain analysis that we perform in the next chapters, is to efficiently solve the inverse problem with minimal assumptions. The data seen by the observer contain some QNM frequencies. These frequencies come from a specific potential and thus from a specific object, which in our case is a SBH. If we know these frequencies, we know the potential and thus the object. So, if we calculate the frequencies, we determine the object, since different objects produce different frequencies.

The point in doing this analysis in the time domain is that the procedure is the closest toy-mimicker of the procedure used to extract frequencies from experimental data, or numerical relativity waveforms. In fact, there is ongoing discussion on the starting time of validity of the linear ringdown, namely whether it can describe well the early post-peak times and the number of modes that we can extract from a given waveform [39–41].

Specifically, in paper [41] the authors present Figure 3.2, which shows the mismatch as a function of the starting time of the fit. They fit linear ringdown models (damped sinusoids) to a waveform generated from numerical relativity simulations. The mismatch (y-axis), is a quantity defined later in the thesis, in equation (B.12), and practically shows the discrepancy of a given signal with the fitted model. A smaller mismatch indicates good agreement between the two. The x-axis shows the starting time after the peak of the signal that is included in the fit. For example, a value of zero on the x-axis means that to perform the fit they included a window of the signal starting from the peak and ending to a constant value.

Notice that, in all cases the mismatch reaches a plateau. By including more and more overtones into the fit (up to seven), the authors obtain better and better mismatches, the starting time of the plateau gradually moves at earlier times. For seven overtones ($N = 7$), the plateau starts exactly at the peak. Based on this, they claim that the post-peak regions of ringdown waveforms can be properly described only by the linear ringdown model, provided that an appropriate number of overtones is included into the fit. Furthermore, they claim that the starting time of validity for the linear ringdown is as early as the peak. Their claim was further supported by the fact that they could recover the mass and spin of the remnant Kerr BH even at the peak of the waveform.

In paper [40], a similar analysis is performed with the explicit comment that ‘the higher overtones lead to very small mismatches by merely overfitting the waveforms’. Practically, their point is that focusing only at the mismatch can be misleading. In linear

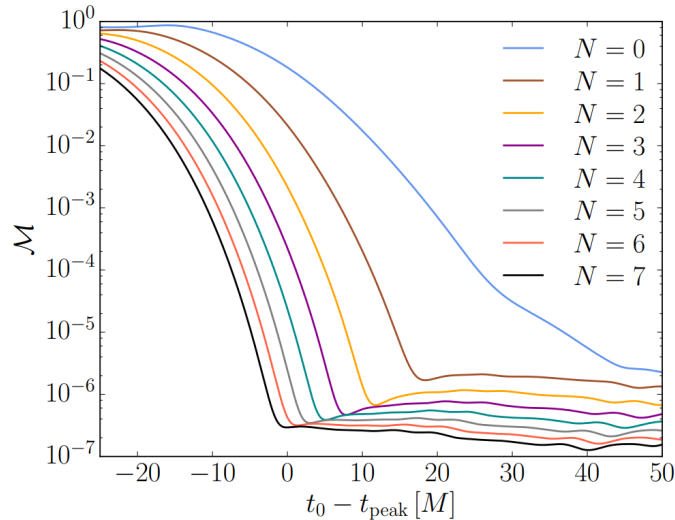


Figure 3.2: Mismatch as a function of the starting time of the fit. The fitted waveform generated by numerical relativity evolution and the fitting models refer to damped sinusoids with N overtones, note that their convention about N differs than the one used in this thesis which indicates the total number of the fitted modes (M. Giesler, M. Isi, M. A. Scheel, and S. A. Teukolsky, “Black Hole Ringdown: The Importance of Overtones,” *Phys. Rev. X*, vol. 9, 041060. doi: 10.1103/PhysRevX.9.041060. Published under [Creative Commons Attribution 4.0 License](#)) [41].

perturbation theory, the amplitude of each mode is constant. So by claiming that one found a mode in the signal, one should provide modes with constant amplitude. However, working with the same waveform as in reference [41], they find that the amplitudes for the overtones higher than the second, remain constant within 10% only for a short range of starting times of the fit, thus making it difficult to claim that these modes were found. They further state that higher overtones than the second, do not contribute to the parameter extraction and that beyond this, all the higher overtones just fit away poorly understood physics related to an evolving background spacetime, time variation of the QNM amplitude due to initial data and nonlinear effects.

3.4 HOW TO COMPUTE QUASINORMAL MODES

After years of ongoing research on BH perturbation theory and QNMs, numerous methods for computing the spectrum have been developed. The historical pattern is the usual. Some researches propose the main foundational idea and subsequently others make more accurate and efficient versions. Given that gravitational potentials lack analytic solutions, the methods are semi-analytic at best, completely numerical, and even involve substitutions of the gravitational potentials with simpler alternatives that are easier to handle.

Each method serves a different purpose and highlights different aspects of the problem. For example, if one wants to robustly compute high overtones it is not wise to choose the extraction from time domain [39]. On the contrary, if one wants to study the dynamical evolution of the perturbations which, for beyond-GR cases, might reveal unexpected types of modes, time evolution is ideal [54]. Here, we will outline the most basic and famous

ones. A summary table of the current status of each method can be found on page 20 of [29].

3.4.1 Frequency-Domain Integration

The direct integration of RW and Zerilli equations in the frequency domain (3.3) is commonly known as *Shooting Method*. In the context of QNM calculation, was introduced by Chandrasekhar and Detweiler [55]. The idea is to make an initial guess for a frequency value, then start from a large value of r_* , where the potential is small and the asymptotic solution is $\sim \exp(-i\omega t)$ and integrate backward to $\sim 3M$, close to the peak of the potentials. Similarly, start integrating forward from a negative value of r_* up to the same point.

If the initial guess of ω leads to a vanishing Wronskian of the two solutions at the common point, it means that the two functions are linearly dependent, therefore eigenfunctions of the boundary value problem and the initial frequency is an eigenvalue, so a QNM. If the Wronskian does not vanish, the initial guess is updated and the process is repeated from the beginning.

This method contains some numerical pitfalls. For example, it becomes unstable for large values of $|r^*|$. For large positive r^* , the solution, whose asymptotic behavior is $\sim \exp(-i\omega r^*)$, becomes contaminated with contributions from the other boundary where $\sim \exp(+i\omega r^*)$, which diverges exponentially. Consequently, in reference [55], the authors integrated the Ricatti equation, which was found to be more stable and is the product of the field redefinition $\Phi \rightarrow \exp\left(i \int^{r^*} \Phi dx\right)$. Their method was stable only for slowly damping modes with $|Im(\omega)| \leq |Re(\omega)|$.

3.4.2 Time-Domain Integration

The time-domain study was firstly performed by Vishveshwara [37]. It is the method that we use in Part II of this thesis and was also discussed in the previous section 3.3. The wave equation (3.11) is solved numerically, an observer records the solution in a fixed position and finally various models are fitted the time-domain recorded signal. From these fits, we try to obtain the QNMs.

3.4.3 Continued Fraction

This method was used for the first time by Leaver in 1985 [56], to compute the QNMs of Kerr BH and is the most accurate method available to date [57]. In brief, the solution is expressed as a series of powers of r . The coefficients of different powers are connected via recurrence relations whose exact form is determined by the underlying potential. These coefficients are correlated to the eigenvalues of the equation, thus by computing them one knows the QNM spectrum.

3.4.4 WKB Method

The Wentzel–Kramers–Brillouin (WKB) method is a widely spread technique for approximating solutions to linear differential equations. In the context of QNMs it was introduced in 1985 by Schutz and Will [58]. Its utility is not limited only to computing the QNMs but also provides useful insights to the inverse problem. Specifically, given a spectrum, the WKB allows us to extract information about the potential and particularly for its properties around its peak.

The starting point of the method is to consider an ansatz $\Phi \sim \exp\left(\sum_{n=0}^{\infty} \delta^{(n-1)} S_n(x)\right)$. Then the GR potential is divided into regions that are separated from the turning points of the potential $Q(r) = \omega^2 - V(r)$. In each region, the ansatz is a different function and the matching is being done at the turning points by Taylor expanding $Q(r)$. In addition, the method works better as the turning points approach each other and at first it was developed only for potentials with two turning points.

For example, the first-order approximation contains only one term at the exponent and the approximation of the frequencies is [58]

$$(M\omega_n)^2 \simeq V^{(0)}(r)\Big|_{r=r_0} - i \left(1 + \frac{1}{2}\right) \left(-2 \frac{d^2 V_\ell(r)}{dr^{*2}}\right)^{1/2}\Big|_{r=r_0}, \quad (3.14)$$

where r_0 is the peak of potential.

The results for the fundamental QNM of a SBH deviate $\sim 7\%$ for the real part and $\sim 1\%$ for the imaginary part of the fundamental mode. As we increase n , the approximation gets worse, since the turning points of $\omega_n - V(r)$ go further away [42]. Including more terms in the ansatz increases the order of the method, leading to more accurate results. For example, WKB up to the sixth order is provided in [59]. Their result for the fundamental mode for the SBH deviates $\sim 0.03\%$ and $\lesssim 0.01\%$ for real and imaginary part respectively.

3.4.5 Inverted Potential

If we know the bound states of a potential, can we map them to the QNMs of its inverted counterpart? This approach, was firstly followed by Ferrari and Mashhoon [60, 61].

Their argument goes as follows. If the potential barrier V depends on a set of parameters p , the QNMs ω and the solution Φ will also depend on p . So we have $V(r; p)$, $\omega(p)$, and $\Phi(r; p)$. Let us consider a generic transformation $r \rightarrow -ir$ and $p \rightarrow p' = \pi(p)$ that leaves the potential invariant $V(r; p) = V(-ir; p')$ but alters the spectrum $\Omega(p') = \omega(p)$ and the solution $\phi(-ir; p') = \Phi(r; p)$. Consequently, if we transform equation (3.3) accordingly, we have that ϕ obeys the same equation, but governed by the inverted potential

$$\frac{d^2 \phi}{dr^{*2}} + (\Omega^2 - V) \phi = 0, \quad (3.15)$$

so ϕ is the solution of the corresponding inverted potential, which is a potential well and Ω are its bound states. This means that if one knows - analytically - the bound states of a

potential, one is able to map them to the QNMs by applying the inverse transformation of the parameters.

In reference [61], they worked with the PT potential

$$V_{PT}(r^*) = -\frac{V_0}{\cosh^2 \alpha(r^* - r_0^*)}, \quad (3.16)$$

where $V_0 > 0$ is the maximum height, r_0^* is the location of the maximum and α determines the width. The PT potential well, admits analytic solutions for its bound states [62]

$$\Omega = \alpha \left(-\left(n + \frac{1}{2}\right) + \left(\frac{1}{4} - \lambda \frac{V_0}{\alpha^2}\right)^{1/2} \right), \quad \text{for } \lambda = -1, \quad (3.17)$$

where n denotes the overtone number. It can be mapped to the barrier through the transformation $p' = \{V_0, \alpha, r_0^*\} \rightarrow p = \{V_0, -i\alpha, r_0^*\}$

$$\omega = \left(V_0 - \frac{1}{4}\alpha^2\right)^{1/2} + i\alpha \left(n + \frac{1}{2}\right) \quad (3.18)$$

We should note that the real part of the frequency is the same for all overtones and that, intuitively, the spectrum is independent of the location of the potential's maximum r_0 but only on its the width and height.

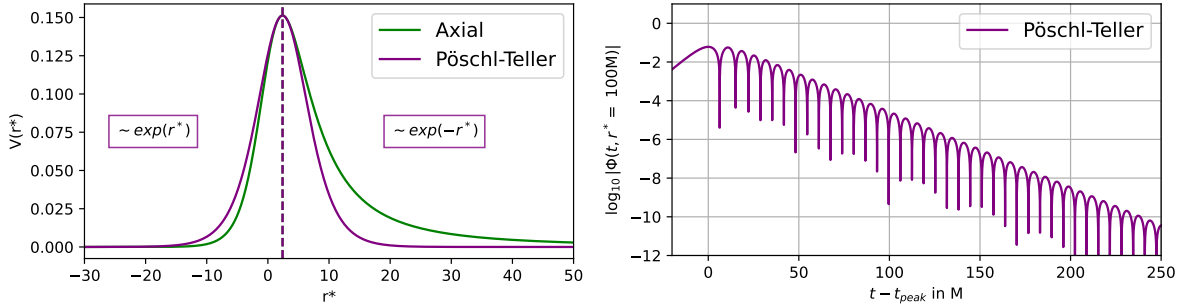


Figure 3.3: **Left panel:** The PT matched with the RW **Right panel:** Waveform that emerges from the PT potential. Note the absence of power-law tail.

The initial goal was to approximate the GR potentials. In Figure 3.3 In order to do so we should match three parameters. The first one is to fix the location of both maxima at r_0 . Afterwards, we should match the values of the maxima

$$V_0 = V_{GR}(r_0^*), \quad (3.19)$$

and also the second derivatives at the maximum r_0 in tortoise coordinates

$$\begin{aligned} \left. \frac{d^2 V_{PT}}{dr^{*2}} \right|_{r_0^*} &= \left. \frac{d^2 V_{GR}}{dr^{*2}} \right|_{r_0^*} \Rightarrow \\ -2\alpha^2 V_0 &= \frac{d^2 V_{GR}}{dr^{*2}} \end{aligned} \quad (3.20)$$

An intuitive explanation of this matching is that according to the WKB approach the modes are created around the peak of the potential and depend on its properties in that point, as seen in equation (3.14).

Chapter Summary

In this chapter we discussed

- Different definitions of QNMs, as eigenvalues of a boundary value problem, as poles of the Green's function and poles of the scattering amplitude.
- Differences between time-domain and frequency-domain.
- The study in time-domain, the different parts of the time-domain signal in greater detail, the incompleteness of QNMs, their stability.
- Various methods of computing the QNMs, such as the direct integration, the time-domain integration, the continued fraction, the WKB and the inverted potential.

PARAMETRIZED FRAMEWORK

General Relativity (GR) has successfully passed numerous major tests by predicting astrophysical phenomena such as the perihelion precession of Mercury, the gravitational deflection of light, the existence of BHs and GWs [21, 63]. However, as many of GR's predictions have now been verified, the focus has shifted towards performing high-precision tests to explore its limits. On one hand, on large scale, where discrepancies have already been noticed, and in the strong field regime, where discrepancies are under examination [63].

One approach to challenge GR is by testing it against modified theories of gravity. These theories are being made by questioning Lovelock's theorem [64], either by questioning the number of dimensions, the number of fields, the order of equations of motion or relaxing the equivalence principle [64, 65]. Each of these modifications leads to slight deviations in the predicted phenomena that can potentially be empirically measured. Consequently, such deviations, if present, are expected to yield small deviations to BH solutions and as a result the QNM spectrum.

In each top-down modification of GR, one should perform highly intricate and repetitive calculations in order to derive the QNM spectrum. However, a bottom-up, theory-agnostic modification has been introduced, initially for non-rotating cases [66, 67] and more recently extended to rotating cases [68]. This approach, known as the *Parametrized Quasi-Normal Mode Framework (PF)*, allows to model all possible modifications of the ringdown at once.

This Chapter presents the PF. Specifically Sec. 4.1 and Sec. 4.2 provide the appropriate motivation and definition, respectively. In Sec. 4.3, we present two examples that illustrate its application and mapping to various cases beyond Schwarzschild Black Hole.

4.1 MOTIVATION

The two body problem of coalescing BHs is of great interest to GW research. The GWs are emitted during the inspiral and the merger carry information about the system's properties such as the BH masses, spins, distance, eccentricity of the orbits [65]. The post-merger phase, the *ringdown*, consists of a remnant oscillating BH. This ringing BH emits gravitational radiation, rich in multipolar structure, until it relaxes exponentially to the final stationary solution. This phase can be adequately described, as we have discussed in Chapter 3, by the QNMs.

Assuming that GR is the correct theory of gravity, the QNMs should depend solely on the mass and spin of the remnant BH [12]. Consequently, a straightforward test of GR could be performed by checking the agreement between the measured and the predicted QNM frequencies. If the fundamental mode is measured, we can calculate the mass and the spin of the BH and if an overtone is also measured, we can test the consistency of its spectrum.

Possible discrepancies with the spectrum predicted by GR could indicate that it is not the complete or correct theory of gravity. This would not be entirely unexpected, as GR alone has not provided a full explanation for large-scale phenomena such as dark matter and dark energy. Current research in this direction is quite vivid, as can be seen in [64, 65]. If one follows a theory-specific top-down approach by modifying the action, the path to uncovering the imprints of these modifications on the spectrum becomes long.

First, comes the identification of a healthy theory. This is being done by questioning Lovelock's theorem which states that EFE are the only second-order local equations of motion for a metric tensor derivable from the Einstein-Hilbert action in 4D [69]. As is evident, there are myriad ways to alter, extend or break these five assumptions: increase the order of EFE, couple the metric with additional fields of all spins, relax the Equivalence Principle (EP), increase the dimensions. Each of these new constructions must be *complete* (explain the outcomes of all experiments), *self-consistent* (providing unique, falsifiable predictions), *relativistic* (reproduce Special Relativity in the absence of gravity) and reproduce the correct *Newtonian limit*.

Secondly, in the context of any new gravitational theory, it is essential to find BH solutions, as we did for GR in Section 1.2. It is important to note that the solution we found assumes spherically symmetric and stationary object within the simplest theory, representing the simplest possible and unrealistic case. However, even within GR the rotating solution, which is the most realistic, is significantly more complicated as will potentially be the analogous derivations in alternative theories.

The real challenge lies in the step of calculating the linear perturbation equations. The complexity of this process became evident in the thesis, where we dedicate an entire Chapter 2, just to outline the steps for the simplest case of perturbations on top of a SBH. Repeating this process, as well as the more complicated counterpart of rotating BHs, for every alternative theory of gravity remains a difficult and ongoing area of research. The status of current calculations can be found in [29].

4.2 DEFINITION

The approach introduced in [66, 67] follows an inverse, bottom-up, and theory-agnostic methodology, allowing for the modeling of all possible modifications simultaneously. Since we are interested in studying the linearized perturbation equations of SBH, we should directly modify them. This type of phenomenological modification is commonly referred to as Parametrized Quasi-Normal Mode Framework (PF). The working hypotheses for the validity of this framework are:

- (a.) small deviations from GR,

- (b.) separable linear ringdown equations of the underlying theory,
- (c.) conservation of asymptotic flatness,
- (d.) non-spinning black hole solution.

This phenomenological modification consists of terms of $1/r$ powers added to the radial ringdown potential. Its most general definition contains N coupled fields (scalar, vector, or tensor) $\Phi = \{\Phi_i\}, i = 1, \dots, N$, around a spherically symmetric and static BH and was introduced in the frequency domain

$$f \frac{d}{dr} \left(f \frac{d\Phi(r)}{dr} \right) + [\omega^2 - fV] \Phi(r) = 0 \quad (4.1)$$

where $f = 1 - r_H/r$, r_H is the radius of the event horizon, ω is the complex frequency and V is the potential matrix. In this thesis, we will only work with up to two fields, so from now on $\Phi = (\psi, \phi)$ and V will be up to 2×2 dimensional matrix. Under the assumptions (a.)-(d.), the parametrized, power-law modification of the potential matrix reads

$$V_{ij} = V_{ij}^{GR} + \delta V_{ij}, \quad (4.2)$$

$$\delta V_{ij} = \sum_{k=0}^{\infty} \delta V_{ij}^{(k)} = \frac{1}{r_H^2} \sum_{k=0}^{\infty} \alpha_{ij}^{(k)} \left(\frac{r_H}{r} \right)^k, \quad (4.3)$$

where $V_{ij}^{(GR)}$ is the GR potential and δV_{ij} is the modification to the GR potential. Firstly, we should note that diagonal terms ($i = j$) correspond to self-interaction terms, whereas non-diagonal terms ($i \neq j$) couple different fields. The diagonal GR scalar and tensor potentials are given in equations (2.33) and (2.32). It should be noted that in the uncoupled case isospectrality between RW and Zerilli potentials holds under very specific and fragile conditions for the corresponding amplitudes a_{ii}^{\pm} and thus is most commonly broken [66].

The modification is described by the power k as well as its corresponding amplitude $a_{ij}^{(k)}$ which in general is complex and can be dependent on the frequency ω . We can find a condition for the amplitude of each different power of modification by demanding the potential's value at its maximum to be much smaller than one. Each maximum is located at

$$\partial_r \delta V_{ij}^{(k)} = 0 \Rightarrow r_{max} = r_H (1 + 1/k),$$

therefore

$$\begin{aligned} \delta V_{ij}^{(k)} \Big|_{r_{max}} &= \frac{1}{k+1} \alpha_{ij}^{(k)} \left(\frac{k}{k+1} \right)^k \ll 1 \Rightarrow \\ \alpha_{ij}^{(k)} &\ll (k+1) \left(1 + \frac{1}{k} \right)^k, \end{aligned} \quad (4.4)$$

thus, the smallness of the modification can be captured and restricted by the above condition.

The solution of (4.1) corresponding to V_{ij}^{GR} potentials is sufficiently described by the frequencies ω^0 , which are the eigenvalues of the boundary value problem with outgoing boundary conditions at spatial infinity and ingoing at the horizon. *Small deviations from the GR potential will lead to small deviations from the GR frequency.* Thus, we can Taylor expand ω around ω^0 up to quadratic order

$$\omega \approx \omega_0 + \alpha_{ij}^{(k)} d_{(k)}^{ij}(\omega) + \alpha_{ij}^{(k)} \alpha_{qp}^{(s)} d_{(k)}^{ij}(\omega) d_{(s)}^{pq}(\omega) + \frac{1}{2} \alpha_{ij}^{(k)} \alpha_{pq}^{(s)} e_{ks}^{ijqp}(\omega) + \mathcal{O}(\alpha^3) \quad (4.5)$$

where Einstein's convention is being used. The most important aspect of this equation is that the coefficients d and e are universal, which means that they do not depend on the amplitudes of the modification, but only on the potential of the underlying theory and its spectrum ω . Their values differ from scalar to tensor fields and also for different overtones, but once we find them, we can use them to study deviations with varying α 's. Values up to quadratic, ignoring the possible dependence on frequency, have been calculated from direct integration of equation (4.1) (shooting method), as well as from the continued fraction method [67, 70].

We should also mention that, in a later work, the PF climbed one step higher [71]. The δV_{ij} modifications on the level of master equations were mapped to the metric. That is, given a metric that can be written as the Schwarzschild metric with some corrections expanded in inverse powers of r , one can quickly compute its spectrum.

Time Domain of the Parametrized Quasi-Normal Mode Framework

In this thesis, we extend the framework in the time domain. In doing so, we assume that the ω^2 term of equation (4.1) comes from a second time derivative and also that there are no other frequency dependent terms. Their presence would contaminate our time domain wave equation with terms containing time derivatives of different order than two. The case with maximum number coupled fields that we are going to study, will be two, for which the wave equation becomes

$$\left(-\frac{\partial^2}{\partial t^2} + f \frac{\partial}{\partial r} \left(f \frac{\partial}{\partial r} \right) \right) \Phi(t, r) - f \mathbf{V} \cdot \Phi(t, r) = 0, \quad (4.6)$$

where we set $V_{12} = V_{21} = 0$ when we study uncoupled fields.

We can work with the PF in the time domain in two different ways: mapping it to specific theories as done in Section 4.3, and test its limits by arbitrarily picking the amplitudes, one at a time or all of them simultaneously, as done in Chapter 7.

4.3 EXAMPLES

4.3.1 Example I: Uncoupled Case

Up to now, the one-liner description of the PF is that it approximates perturbations on top of beyond-GR stationary and spherically symmetric solutions using as base the GR perturbations. However, a more inclusive description would be that it approximates spacetimes beyond Schwarzschild. This includes both modifications of GR and also the extension of Schwarzschild spacetime to others that are GR solutions and for example contain charge or small spin or charge [66].

We will focus on the extension to Reissner-Nordstöm BH, which is spherically symmetric and stationary *charged* BH just to illustrate in detail how the PF is being mapped to extensions of the RW potential. The linearized axial perturbations for this metric obey the equation

$$f_{RN} \frac{d}{dr} \left(f_{RN} \frac{d\Phi(r)}{dr} \right) + [\omega^2 - f_{RN} V] \Phi(r) = 0, \quad \text{where} \quad (4.7)$$

$$f_{RN} = 1 - \frac{2M}{r} + \frac{Q^2}{r^2} = \left(1 - \frac{r_+}{r}\right) \left(1 - \frac{r_-}{r}\right),$$

$$V_{RN} = \frac{\ell(\ell+1)}{r^2} + \frac{4r_H r_-}{r^4} - \frac{3(r_H + r_-)}{2r^3} - \frac{\sqrt{4(\ell-1)(\ell+2)r_H r + 9(r_H + r_-)^2/4}}{r^3},$$

where the two horizon radii are $r_{\pm} = M \pm M\sqrt{1 - (Q/M)^2}$, from which the internal one r_- , has no physical significance since the outer one r_+ excludes any communication with its interior. We note that for small values of the charge $|Q| \ll M$, the multiplying factor of the potentials can be written as $f_{RN} = f(r)Z(r)$, where $f(r) = (1 - r_H/r)$ and $Z(r) = (1 - (Q^2/2M)/r)$. Here the horizon r_H is not equal to $2M$, but $r_H = r_+ = 2M - Q^2/2M + \mathcal{O}(Q^4)$. If we redefine the field as $\Psi = \sqrt{Z(r)}\Phi$, we obtain an equation of the form (4.1)

$$f \frac{d}{dr} \left(f \frac{d\Phi}{dr} \right) + \left[\left(1 - \frac{r_-}{r_H}\right)^{-2} \omega^2 - f(V_- + \delta V) \right] \Phi = 0, \quad (4.8)$$

with

$$\delta V = 2 \frac{r_-}{r_H} \omega_0^2 - \frac{1}{r_H^2} \left(\frac{\lambda + 6r_-}{3} \frac{r_-}{r_H} \right) \left(\frac{r_H}{r} \right)^3 + \frac{1}{r_H^2} \left(\frac{5r_-}{2r_H} \right) \left(\frac{r_H}{r} \right)^4, \quad (4.9)$$

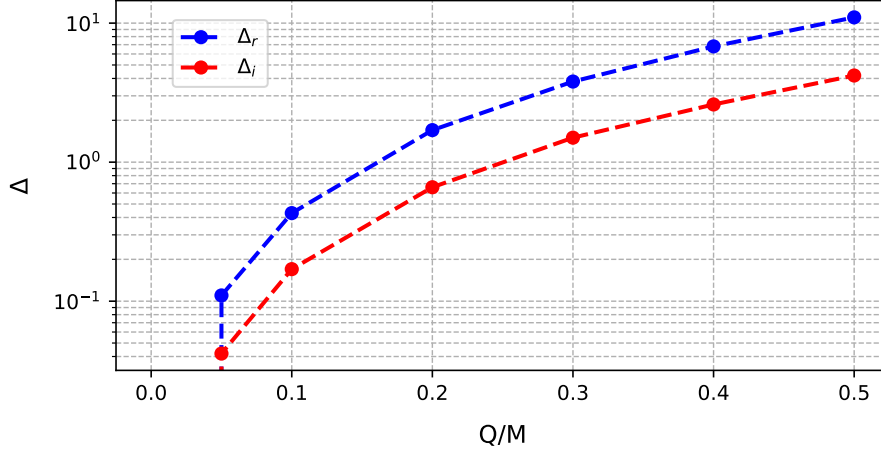


Figure 4.1: Errors of the PF fundamental mode predictions, compared to the exact Reissner-Nordström. Data taken from [66].

if we compare with equation (4.3), we find that there are only three terms that modify the potential from a SBH and their amplitudes are dependent on the parameters of the extension of axial RW potential

$$\alpha^{(0)} = 2\omega_0^2 \frac{r_-}{r_H}, \quad (4.10a)$$

$$\alpha^{(3)} = -\frac{\lambda + 6r_-}{3r_H}, \quad (4.10b)$$

$$\alpha^{(4)} = \frac{5r_-}{2r_H}. \quad (4.10c)$$

Now, the modification on the frequency based on equation (4.5) can be written

$$\omega_{RN-PF} = \left(1 - \frac{r_-}{r_H}\right) \left(\frac{2\omega_0}{r_H} + d_0 a^{(0)} + d_3 a^{(3)} + d_4 a^{(4)}\right). \quad (4.11)$$

We can define quantities, Δ_r and Δ_i , to quantify the accuracy of the QNM predictions obtained from the PF in equation (4.11) by comparing to the frequencies of the correct Reissner-Nordström potential. These quantities are defined as the following percentage

$$\Delta_r = \left| \frac{\text{Re}[\omega_{RN-PF} - \omega_{GR}]}{\text{Re}[\omega_{full} - \omega_{GR}] - 1} \right|, \quad (4.12)$$

where ω_{RN} is obtained by solving the exact master equation for Reissner-Nordström BH and similarly for the imaginary part. The result is shown in Fig (4.1) We observe that as the Q over M ratio becomes larger, the PF approximation deviates more and more from the exact values reaching up to 11% for the real and $\sim 4\%$ for the imaginary part. We can also observe that the imaginary part is better approximated than the real part.

4.3.2 Example II: Coupled Case - dynamical Chern-Simons gravity ^[67]

We will now show an example of mapping the PF to a beyond-GR theory. The dynamical Chern-Simons (dCS) gravity is a modification of GR that, additionally to the gravitational tensor field, contains a scalar field coupled to it with via the curvature. So, related to the assumptions of Lovelock's theorem, it questions the number of the fields. Dynamical means that the scalar field, θ , is changing over time [64]. This new CS! term is parity-violating and shows up in many branches of physics like particle physics, string theory and loop quantum gravity [72]. The action of dCS in vacuum is

$$\mathcal{S} = \mathcal{S}_{EH} + \mathcal{S}_\theta + \mathcal{S}_{CS}, \quad (4.13)$$

where the Einstein-Hilber term as usual is

$$\mathcal{S}_{EH} = \kappa \int d^4x \sqrt{-g} R,$$

where $\kappa = (16\pi)^{-1}$, g is the determinant of the metric tensor and R is the Ricci scalar. The part containing the kinetic and potential terms of the scalar field is

$$\mathcal{S}_\theta = -\frac{\beta}{2} \int d^4x \sqrt{-g} (g^{\mu\nu} (\nabla_\mu \theta) (\nabla_\nu \theta) + 2V(\theta)),$$

where β is a coupling constant, ∇_μ is associated with the metric $g^{\mu\nu}$ and the potential $V(\theta)$ is set to zero. The original version of dCS was not dynamical since it assumed a non-dynamical scalar field chosen "a priori" which served as a background. This can be done by setting $\beta = 0$. Finally, we have the Chern-Simons term, which couples the scalar field to the Pontryagin density $*RR$

$$\mathcal{S}_{CS} = \frac{\alpha}{4} \int d^4x \sqrt{-g} \theta *RR, \quad *RR = *R^\mu{}_\nu{}^{\kappa\delta} R^\nu{}_{\mu\kappa\delta}, \quad *R^\mu{}_\nu{}^{\kappa\delta} = \frac{1}{2} \epsilon^{\mu\nu\alpha\beta} R^{\alpha\beta\kappa\delta},$$

where α is the CS! coupling constant and $\epsilon^{\mu\nu\alpha\beta}$ the Levi-Civita symbol. This last term induces a parity violation coming from the Pontryagin density. By parity we mean purely spatial. Also, we should note that the θ field is actually a pseudo-scalar, since its parity transformation is $\hat{\mathcal{P}}[\theta] = -\theta$.

Conveniently, the Pontryagin density term vanishes in spacetimes with spherical symmetry. The EFE are reduced to [54]

$$R_{\mu\nu} = 8\pi \partial_\mu \theta \partial_\nu \theta, \quad (4.14)$$

$$\square \theta = 0. \quad (4.15)$$

So, the scalar field is constant and consequently the Schwarzschild metric is also a solution to dCS without any corrections.

However, linear perturbations on top of the SBH are not the same as GR, since the scalar field is also perturbed and provided that it is coupled to the gravitational field, it affects

it, and vice versa. To obtain the linear equation, a procedure similar the one described in Chapter 2 should be done assuming that the scalar and gravitational fields are of the same order[73]. It was found that the dCS axial and polar perturbations are decoupled and that the scalar field is coupled with the axial perturbations, therefore the spectrum of the polar perturbations is the same as GR. The perturbation equations that we get are two coupled wave equations [67]

$$-\frac{\partial^2 \Phi(t, r^*)}{\partial t^2} + \frac{\partial^2 \Phi(t, r^*)}{\partial r^{*2}} - V_{11}(r)\Phi(t, r^*) = V_{12}(r)\Psi(t, r^*), \quad (4.16a)$$

$$-\frac{\partial^2 \Psi(t, r^*)}{\partial t^2} + \frac{\partial^2 \Psi(t, r^*)}{\partial r^{*2}} - V_{22}(r)\Psi(t, r^*) = V_{21}(r)\Phi(t, r^*), \quad (4.16b)$$

where $\Phi \equiv \Phi_\ell^-$ is the axial gravitational field, Ψ is part of the scalar field after some transformations of the form $\theta = \Psi^{\ell m} Y^{\ell m} e^{-i\omega t} / r$ and the potentials are given by

$$V_{11} = V^-, \quad (4.17a)$$

$$V_{22} = V_{scalar} + \frac{1}{r_H^2} \frac{144\pi\ell(\ell+1)}{\beta r_H^4} \left(\frac{r_H}{r}\right)^8, \quad (4.17b)$$

$$V_{12} = V_{21} = \frac{1}{r_H^2} \frac{12}{\sqrt{\beta} r_H^2} \sqrt{\pi \frac{(\ell+2)!}{(\ell-2)!}} \left(\frac{r_H}{r}\right)^5, \quad (4.17c)$$

where V^- and V_{scalar} are given in equation (2.33).

We should define a parameter $\bar{\gamma} = \beta^{-1/2} r_H^{-2}$ which is larger when the coupling increases. Any modification will be a small deviation from GR. So it is reasonable to assume small values from $\bar{\gamma}$. For small $\bar{\gamma}$ (equivalently large β), the additional potential terms are small corrections on top of GR. Thus we can use the PF to approximate the frequencies. The amplitudes that map the PF to dCS are

$$a_{22}^{(8)} = \bar{\gamma}^2 144\pi\ell(\ell+1), \quad (4.18a)$$

$$a_{12}^{(5)} = a_{21}^{(5)} = 12\bar{\gamma} \sqrt{\pi \frac{(\ell+2)!}{(\ell-2)!}}. \quad (4.18b)$$

We have two classes of modes that are *both* contained in the oscillations of *both* perturbations. *Tensor-led* modes stem from small deviation of the gravitational QNMs and accordingly for the *scalar-led* modes [54]. Tensor-led modes are given from

$$\omega = \omega_0 + e_{(55)}^{1221} \left(12\bar{\gamma} \sqrt{\pi \frac{(\ell+2)!}{(\ell-2)!}} \right)^2, \quad (4.19)$$

and the scalar-led

$$\omega = \omega_0 + 2d_{(8)} 144\pi\ell(\ell+1)\bar{\gamma}^2 + e_{(88)} (144\pi\ell(\ell+1)\bar{\gamma}^2)^2 + e_{(55)}^{1221} \left(12\bar{\gamma} \sqrt{\pi \frac{(\ell+2)!}{(\ell-2)!}} \right)^2. \quad (4.20)$$

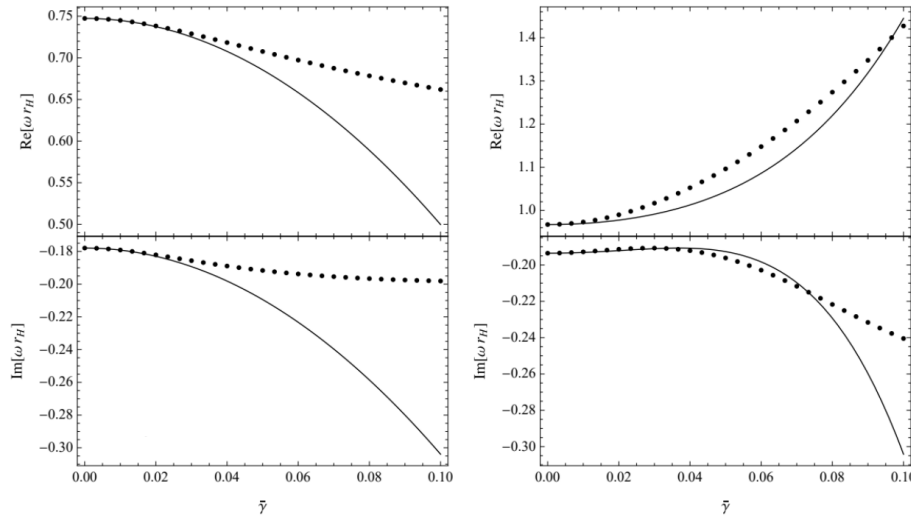


Figure 4.2: Real and imaginary parts of tensor-led (left) and scalar-led (right) fundamental QNMs in dCS gravity. The solid lines are PF approximations whereas the bullets are computed from direct integration (R. McManus, E. Berti, C. F. B. Macedo, M. Kimura, A. Maselli, and V. Cardoso, “Parametrized Black Hole Quasinormal Ringdown. II. Coupled Equations and Quadratic Corrections for Nonrotating Black Holes,” *Phys. Rev. D*, vol. 100, 044061 (2019), [arXiv:1906.05155](https://arxiv.org/abs/1906.05155) [gr-qc]. Published under [Creative Commons Attribution 4.0 License](https://creativecommons.org/licenses/by/4.0/).) [67].

In Figure 4.2 we see a comparison of the fundamental $\ell = 2$ mode as calculated from the PF and from direct integration of equations (4.16). We can comment that as the parameter γ becomes larger, the discrepancies between the approximations and the exact calculations grows.

Chapter Summary

In this chapter, we discussed the following key points:

- The motivation and definition of the Parametrized Quasi-Normal Mode Framework.
- The PF is a bottom-up and theory agnostic modification to the GR ringdown of a spherically symmetric BH.
- It captures all $1/r$ modifications simultaneously.
- It can be extended to ringdown cases within GR that include small spin and charge.

5

NUMERICAL TECHNIQUES

From this Chapter we initiate the more technical discussion regarding the employed techniques. Specifically, in Sec. 5.1 we present the numerical method we applied to solve the equations and in 5.2 we discuss about the algorithm used to fit the various models to the numerical solutions. The methods, namely the way that these techniques are applied, are presented in the beginning of Part II of the thesis.

5.1 SOLVE THE EQUATIONS

References used for this section: [74, 75].

We are going to discuss the evolution of one single field, as described by the perturbation equation around a Schwarzschild Black Hole (SBH). This equation, as we have already seen, is a wave equation with a potential, which dictates the time evolution of an initial wavepacket.

5.1.1 Uncoupled Case: Staggered Leapfrog Method

The most general way in which we can write the wave PDE for $t \in [0, t_f], r^* \in (-\infty, +\infty)$, is the following.

$$-\partial_{tt}\Phi(t, r^*) + c^2 \partial_{**}\Phi(t, r^*) - V(r)\Phi(t, r^*) = 0, \quad (5.1)$$

$$(IC) : \begin{cases} \Phi(t = 0, r^*) = h(r^*) \\ \partial_t \Phi(t = 0, r^*) = g(r^*), \end{cases} \quad (5.2)$$

$$(BC) : \begin{cases} \Phi(t, r^* \rightarrow -\infty) \sim e^{i\omega(t+x/c)} \\ \Phi(t, r^* \rightarrow +\infty) \sim e^{i\omega(t-x/c)}, \end{cases} \quad (5.3)$$

where $\Phi(t, r^*)$ is the field we are evolving, $V(r)$ the potential which governs the evolution and c the velocity which from now on we set equal to one.

Note that the spatial derivative is in tortoise coordinate r^* , whereas the potential is given in the standard radial coordinate r . This means that in every step of the numerical scheme, we must perform the mapping $r^* \rightarrow r$.

We know the map $r \rightarrow r^*$ analytically from equation (1.14), although its inverse, although also analytical, is given by not such a trivial function, the *Lambert W function*. In

addition, the outgoing boundary conditions are imposed for $|r^*| \rightarrow \infty$, which cannot be explicitly implemented in numerical schemes. So now, let us discuss how we discretize the main equation and address the aforementioned issues.

Discretization of the equation

The numerical scheme that we employ to solve the equation is called the *Staggered Leapfrog* method [75]. First, to discretize our domain, we create a rectangular mesh, which consists of N_t temporal and N_{r^*} spatial points. This discretization approximates the initial PDE with a set of algebraic equations with finite differences. The distance between each point is equal and is denoted by Δt and Δr^* .

$$\left. \begin{aligned} \Delta t &= (t_f - 0) / N_t \\ \Delta r^* &= (r_f^* - r_i^*) / N_{r^*} \end{aligned} \right\} \Rightarrow \begin{cases} t_j = 0 + j\Delta t & , \quad j = 0, \dots, N_t \\ r_i^* = r_i^* + i\Delta r^*, & i = 0, \dots, N_{r^*} \end{cases} \quad (5.4)$$

We observe that the spatial coordinate does not take values over the entire \mathbb{R} ; its domain is restricted. Now that we have defined a grid whose limit for small $\Delta t, \Delta r^*$ is identical to our initial continuous domain, we can define the discretization of equation (5.1).

We approximate the second order derivatives using centered finite differences¹ of second order both in time and space. After some calculations we obtain the equation

$$\begin{aligned} \Phi_i^{j+1} &= 2\Phi_i^j - \Phi_i^{j-1} + CFL^2 \left(\Phi_{i+1}^j + \Phi_{i-1}^j - 2\Phi_i^j \right) - \Delta t^2 \Phi_i^j \cdot V_i, \\ &\text{for } i = 1, \dots, N_{r^*} - 1 \text{ and } j = 2, \dots, N_t \end{aligned} \quad (5.5)$$

where we define $\Phi_i^j := \Phi(t_j, r_i^*)$, $V_i := V(r_i)$ and $CFL = c\Delta t / \Delta r^*$ is the Courant-Friedrichs-Lewy (CFL) parameter, through which we can define a stability criterion for the method. It is important to note that this equation does not cover the whole domain and that information for the values $j = 0, 1$ and $i = 0, N_{r^*}$ is given by the Initial and Boundary Conditions respectively.

The exact way in which previous temporal steps are used to propagate the solution to the next temporal step is visualized in Figure 5.1. The stability criterion for the free wave equation is also depicted in Figure 5.1. The diagonal dashed lines are the characteristic lines of the wave equation ($r^* \pm ct = const.$). The solution at a certain point (t, r^*) should only depend on the information coming from the interior of the domain defined by these lines. On the contrary, in the discretized problem, the solution at the point (t_j, r_i^*) depends on a different domain, which is given by the interior of the lines with slope $CFL = c\Delta t / \Delta r^*$ (gray solid lines in the figure). If the numerical domain of dependence is smaller than the analytical domain of dependence, which translates into $CFL > 1$, then the numerical solution is unstable. Intuitively, this happens because the numerical solution ignores necessary information from the previous points that lie between the two domains. If the numerical domain of dependence is larger than or identical to the analytical, $CFL \leq 1$, then the nu-

¹ Each second order derivative is discretized as $\partial_{xx}f(x) = (f(x_{i+1}) + f(x_{i-1}) - 2f(x_i)) / \Delta x^2$

merical solution is stable. We should also note that, as CFL approaches to 1, the solution approximates better the analytical one.

We emphasize that the above criterion refers to the free wave equation. When we introduce the potential this criterion changes since the potential should be resolved well. Therefore we choose resolutions which yield much smaller than one CFL.

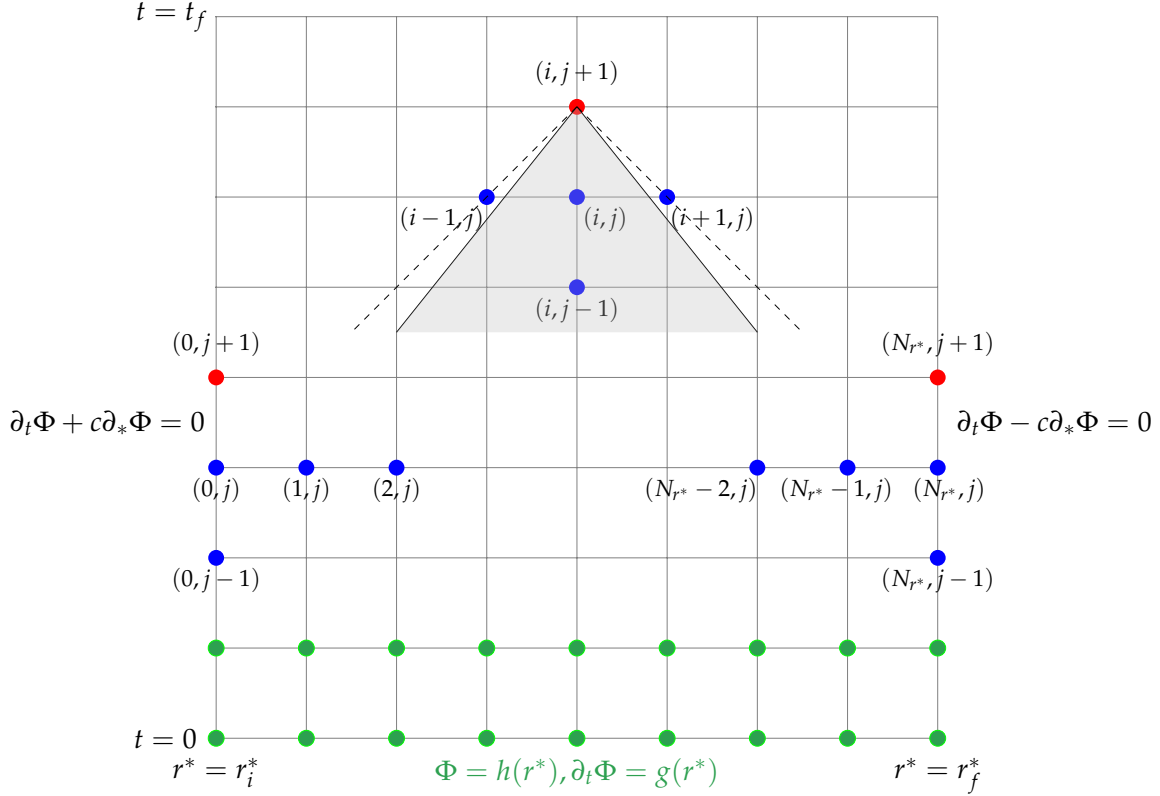


Figure 5.1: Equation (5.5) shown schematically. Staggered Leapfrog Stencil (Center), with outgoing BC (left and right), initial conditions determining the first two steps (lower green) and CFL criterion (triangle in shadow).

Initial Conditions

The Initial Conditions required for the wave equation are two: one for the field and one for its time derivative. They determine the first two steps of the scheme. The initial condition for the field also plays a role on how the QNMs are excited, even though it does not affect the actual values of the frequency. Throughout this thesis, we adopt a Gaussian as initial condition for the field

$$\Phi(t=0, r^*) = h(r^*) = A \cdot \exp\left(-\frac{(r^* - \mu)^2}{2\sigma^2}\right). \quad (5.6)$$

The initial condition for the derivative, determines the initial movement of the Gaussian. For example if we take an initially static field, $\partial_t \Phi(0, r^*) = g(r^*) = 0$, the Gaussian will split in two. However, in order to excite the QNMs we want to direct it towards the po-

tential, which is usually placed to the left of the IC. We can achieve this by imposing an advection equation for the derivative

$$\partial_t \Phi(t=0, r^*) = g(r^*) = -c \partial_x \Phi(t=0, r^*), \quad (5.7)$$

which by using (5.6) becomes

$$\partial_t \Phi(t=0, r^*) = g(r^*) = -c \frac{(r^* - \mu)}{\sigma^2} \cdot \Phi(t=0, r^*). \quad (5.8)$$

The discretized version of equations (5.6) and (5.8) is

$$\Phi_i^0 = h_i = A \cdot \exp\left(-\frac{(r_i^* - \mu)^2}{2\sigma^2}\right), \quad (5.9a)$$

$$\frac{\Phi_i^1 - \Phi_i^0}{\Delta t} = g_i = -c \frac{(r_i^* - \mu)}{\sigma^2} \Phi_i^0, \quad (5.9b)$$

where $h_i = h(r_i^*)$ and $g_i = g(r_i^*)$.

At this point, we should note a subtlety. We have already mentioned that from the IC, we can compute the first two steps of the numerical evolution, which serve as starting points. It is obvious that from (5.9a), we obtain the first step for $j = 0$. However, one could be naive and compute the second time step, for $j = 1$, by solving (5.9b) for Φ_i^1 . *This is not correct.* We must also consider the effect of the potential on the evolution to $j = 1$.

The correct approach is the following. We introduce a *phantom point* at $j = -1$. "Phantom" because it does not play a further role in the evolution and it is not a part of the grid. Now we can express the Finite Difference of the IC given by the equation (5.8) between $j = 0$ and $j = -1$. By substituting $j = 0$ into the main equation (5.5) we obtain

$$\frac{\Phi_i^0 - \Phi_i^{-1}}{\Delta t} = g_i = -c \frac{(r_i^* - \mu)}{\sigma^2} \Phi_i^0, \quad (5.10a)$$

$$\Phi_i^1 = 2\Phi_i^0 - \Phi_i^{-1} + CFL^2 (\Phi_{i+1}^0 + \Phi_{i-1}^0 - 2\Phi_i^0) - \Delta t^2 V_i \cdot \Phi_i^0. \quad (5.10b)$$

If we eliminate the phantom term Φ_i^{-1} , we obtain the correct value for the second time step $j = 1$

$$\Phi_i^1 = \Phi_i^0 + \Delta t \cdot g_i + CFL^2 (\Phi_{i+1}^0 + \Phi_{i-1}^0 - 2\Phi_i^0) - \Delta t^2 V_i \cdot \Phi_i^0. \quad (5.11)$$

As a final note, including the potential, only matters when we place the ICs close to the potential. If our initial Gaussian is far away from the potential influence, taking into account for the calculation of the first time step will not have such an impact.

Boundary Conditions

In principle, the Boundary Conditions should be outgoing, as shown in equation (5.3). However, since we generally do not know the frequencies that our solution contains, we cannot apply this relation directly. Instead, we can achieve purely numerical outgoing

BCs by imposing two advection equations at the boundaries of our grid. These equations will transport the quantity they receive out of the numerical domain. The equations read

$$\partial_t \Phi(t, r^*) + c \partial_* \Phi(t, r^*) = 0, \text{ at } r^* = r_0^*, \quad (5.12a)$$

$$\partial_t \Phi(t, r^*) - c \partial_* \Phi(t, r^*) = 0, \text{ at } r^* = r_f^*. \quad (5.12b)$$

Due to numerical errors, these boundary conditions cannot be exact. As a result, there will always exist a reflected fraction of the field, contaminating the signal. To mitigate the impact of these reflections on the numerical solution, we not only impose outgoing boundary conditions, but also place the boundaries of the numerical domain in such a distance that the reflections will not have the sufficient time to travel back to the observer and interfere with our desired results.

The discretization of the advection equation on the boundaries is being done with the upwind scheme. The intuitive advantage of this scheme, for example from central differences, is that the solution on the next time step depends only on points that are located in the direction from which the advective quantity comes. For example, if we want to find the solution on point $(i_s, j_s + 1)$, it will depend only on points with $i < i_s$ if the velocity is directed to the right and on points with $i > i_s$ if the velocity is directed to the left. This is shown schematically in Figure 5.1. In terms of discretization, we have

$$\Phi_0^{j+1} = \Phi_0^j + \frac{CFL}{2} (3\Phi_0^j - 4\Phi_1^j + \Phi_2^j), \quad (5.13a)$$

$$\Phi_{N_{r^*}}^{j+1} = \Phi_{N_{r^*}}^j - \frac{CFL}{2} (3\Phi_{N_{r^*}}^j - 4\Phi_{N_{r^*}-1}^j + \Phi_{N_{r^*}-2}^{j+1}), \quad (5.13b)$$

where we have used first order approximation for the time derivative and second order for the spatial derivative.

Coordinate Clarification

To complete the description of the numerical scheme for the uncoupled case, we have to clarify a final point in equation (5.1): the fact that the derivative is given in tortoise coordinate r^* , whereas the potential, in the usual r of the Schwarzschild coordinates. The transformation $r^* \rightarrow r$ is simple and is given by equation (1.14). The inverse transformation, that is, finding r^* for given r , is not so obvious. One could do it by numerically solving the equation at each time step, but this would be expensive and not accurate enough.

However, an analytic function which inverts equation (1.14) exists, is called *Lambert W function* and is defined by the relation

$$we^w = z \Rightarrow w = W_k(z), \quad (5.14)$$

where $w, z \in \mathbb{C}$ and $k \in \mathbb{N}$. Now, if $X, Y \in \mathbb{R}$, then the inversion becomes

$$Ye^Y = X \Rightarrow Y = \begin{cases} W_0(X), & X \geq 0, \\ W_0(X) \text{ or } W_{-1}(X), & -1/e \leq X < 0. \end{cases} \quad (5.15)$$

Thus, when *Lambert W function* is real-valued, it can be seen as the inverse function of xe^x and thus is also called *product logarithm function*. The equation that relevant to our case, can be written in the form of (5.15). From equation (1.13) we have

$$\exp\left(\frac{r^* - r}{r_H}\right) = \frac{r}{r_H} - 1$$

if we define $X := \exp(r^*/r_H - 1) > 0$ and $Y := r/r_H - 1$, we obtain

$$\exp\left(\frac{r^* - r_H}{r_H}\right) \cdot \exp\left(\frac{r_H - r}{r_H}\right) = \frac{r - r_H}{r_H} \cdot Y$$

and finally

$$X = Y \cdot e^Y.$$

As a result, from (5.15), we have

$$r = r_H + r_H \cdot W_0\left(\exp\left(\frac{r^*}{r_H} - 1\right)\right). \quad (5.16)$$

Now, for each r^* , we have analytically its corresponding r .

5.2 FIT THE FUNCTIONS

The solution of the wave equation is a scalar function which takes a different value at each point in space and time. If we fix the spatial position, namely setting an observer at a constant point in space, this observer records a signal in the time domain. This setup is shown schematically in Figures 3.1 and 5.2.

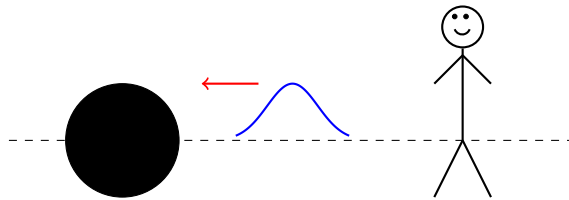


Figure 5.2: Simplified explanation of the study in the time domain. The signal is extracted by fixing the position of an observer and recording the data seen.

To fit the various models to the time-domain signal obtained from numerical solutions, we employ the `curve_fit` function from PYTHON's `scipy` library. This function, minimizes the Sum of Square Error Function (SSE) with respect to the model's parameters

$$S(\boldsymbol{\theta}) = \sum_{i=1}^n (f(x_i; \boldsymbol{\theta}) - y_i)^2, \quad (5.17)$$

where y_i are the numerical data, f is the model, $\boldsymbol{\theta} \in \mathbf{R}^K$ is the parameter vector where K is the dimension of the parameter space. The x_i are the points in the domain.

This PYTHON function, uses by default the Levenberg–Marquardt (LM) algorithm to optimize the SSE function [76]. The LM is an iterative method which requires an initial guess for the parameters, $\boldsymbol{\theta} = \boldsymbol{\theta}_0$, to start. Each step moves the previous values of the parameters $\boldsymbol{\theta}$ by a small amount $\boldsymbol{\chi}$, so that $\boldsymbol{\theta}$ becomes $\boldsymbol{\theta} + \boldsymbol{\chi}$. By Taylor expanding the function $f(x_i; \boldsymbol{\theta})$ around $\boldsymbol{\theta}$, we obtain

$$f(x_i; \boldsymbol{\theta} + \boldsymbol{\chi}) \simeq f(x_i; \boldsymbol{\theta}) + \mathbf{J}_{ij} \cdot \boldsymbol{\chi} + \mathcal{O}(\boldsymbol{\chi}^2), \quad (5.18)$$

where the Jacobian is $\mathbf{J}_{ij} = \partial f(x_i; \boldsymbol{\theta}) / \partial \theta_j$. Setting the derivative with respect to $\boldsymbol{\chi}$ equal to zero, yields

$$\left(\mathbf{J}^T \mathbf{J} + \mu \mathbf{I} \right) \boldsymbol{\chi} = \mathbf{J}^T (\mathbf{y} - f(\mathbf{x}, \boldsymbol{\theta})), \quad (5.19)$$

where $\mu \geq 0$ is the damping parameter introduced by Levenberg. This parameter controls the step size of each iteration, so that for steeper regions of the function the change is chosen smaller and inversely for flatter regions the step is chosen larger to accelerate convergence. In each step a linear system of equations should be solved in order to obtain the approximation of the parameters.

In the following Chapters (6) and (7), we work in parameter spaces of dimension 3 to 10. This makes the SSE function susceptible to many local minima which potentially might lead the LM getting stuck in one of them and missing the global minimum. To improve this a bit, we carefully choose the initial guess, as we discuss in the next Chapter 6.

Chapter Summary

In this chapter, we discussed the following points:

- The central in time and in space numerical scheme we use (staggered leapfrog).
- The implementation of the nonreflecting BCs through an advection equation
- The way we impose an advection equation as Initial Conditions for the derivative to prevent the direct propagation of the initial Gaussian to the observer.
- The application of an advection equation as Initial Conditions for the derivative to prevent the direct propagation of the initial Gaussian to the observer.
- The fitting algorithm employed.

Part II

Applications and Results

APPLICATIONS & RESULTS I

In this chapter, we present the first set of results, focusing on cases related to [GR](#). The high-level explanation of the procedure is the following: we generate ringdown waveforms by numerically solving the linear perturbation equations with [GR](#)-related potentials. Afterward, we employ different models to fit these waveforms and extract their parameters by systematically adjusting the portion of the waveform included in the fits (the fitting window) to evaluate how it impacts the parameter extraction.

More specifically, the potentials we use are the Pöschl-Teller ([PT](#)) potential, matched to the Regge-Wheeler ([RW](#)), as well as the [RW](#) potential itself. The models employed contain different number of modes, with some also including the power-law tail. The results here partially reproduce those in reference [\[39\]](#), with an extension to incorporate models that include tails.

The structure of this Chapter is that we first present the methods used to produce the waveforms and fit them with the various models in [Sec. 6.1](#). Then we apply them and examine the impact of the starting time of the fit on [PT](#) generated waveforms that are not contaminated with a late-time power-law tail in [Sec. 6.2](#) and in [Sec. 6.3](#) we study the [RW](#) generated waveform to also see the impact of the tail. Finally, in [Sec. 6.4](#) we treat both ends of the fitting window as free parameters.

6.1 METHODS

A common method for studying wave equations of the form [\(3.11\)](#) with a potential V , in the time-domain, involves first solving them numerically and then analyzing the results.

The step regarding the solution was discussed extensively in [Chapter 5](#). We use the Leapfrog scheme, which is a finite difference scheme, central in time and space, for a grid with resolutions $\Delta t = 0.01$ and $\Delta r^* = 0.02$. The chosen initial data is

$$\Phi(0, r^*) = A e^{-\frac{(r^* - \mu)^2}{2\sigma^2}}, \quad (6.1a)$$

$$\partial_t \Phi(0, r^*) = \partial_* \Phi(0, r^*) \quad (6.1b)$$

for $A \sim \max\{V\}$, $\mu = 30M$ and $\sigma = 1M$. The second condition [\(6.1b\)](#) forces the Gaussian to become ingoing, thus to move only towards the potential.

The Boundary Conditions are imposed as outgoing. However, since outgoing Boundary Conditions are implemented numerically, their implementation is imperfect, introducing numerical errors. To mitigate possible contamination of the signal due to reflections from

these imperfect boundary conditions (6.1b), we set the domain boundaries far enough from the region of interest.

The resulting numerical solution is time and space dependent. In order to extract the time-domain signal we place an observer at the fixed position of $R = 100M$ and we study the recorded signal. This location is chosen sufficiently far from the light ring, ensuring that the recorded waveform has ceased interacting with the BH potential and is nearly in its final form. Although the ideal position would be at spatial infinity, this is not feasible due to the increasing numerical cost.

In general, the recorded signal can be divided into three parts: the main bulk, sufficiently described by the QNMs, the initial transient regime where the modes have not yet fully developed and the late-time power-law tail. The two latter contributions influence the extraction of the parameters. A first and naive indication for this, is shown in Figure 6.1, where the blue line is the extracted signal and the others refer to different fitting models including one damped sinusoid (yellow line), the power-law tail (red line) or both (green line). Observe that when the power law tail is included the result of the fit almost coincides with the recorded signal especially at late times of the ringdown. Let's try to quantify this better by specifying exactly the fitting procedure and the fitting models.

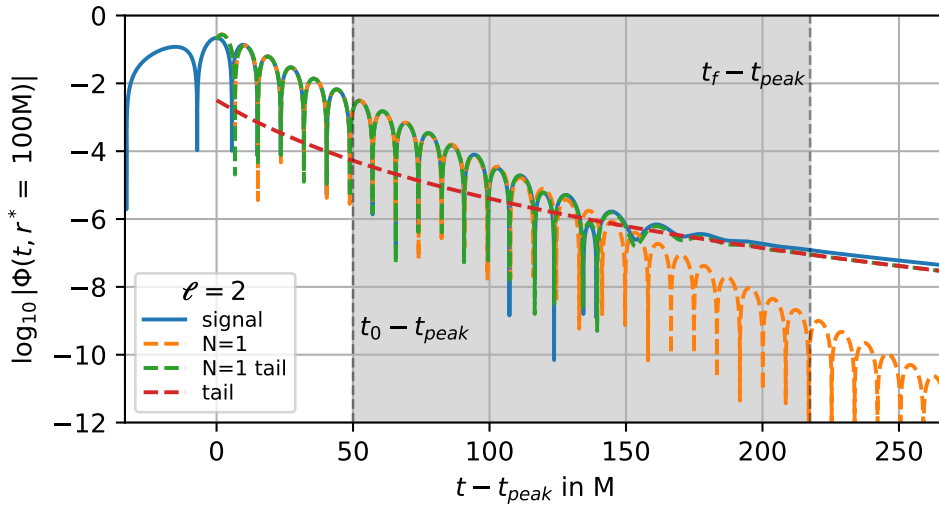


Figure 6.1: The waveform extracted by numerically solving equation (2.30) with RW potential with multipole number $\ell = 2$ is shown in the blue line. Also some fitting models are shown containing $N = 1$ mode (yellow line), $N = 1$ mode and tail (green line), tail alone (red line). The fitting window for the first two is indicated with the gray shaded area, starting at $t_0 - t_{\text{peak}}$ and ending at $t_f - t_{\text{peak}}$, where t_{peak} is the time at which the waveform takes its maximum. For the tail-only model, the fitting window is located at the final 50M. Here we see the extrapolation of the fitting results beyond their fitting windows.

A. The fitting models

The goal of this Chapter is to study how the portion of the waveform included in the fits impacts the parameter extraction. For that reason, we employ and compare different kinds

of analytical toy-models to extract the main features of the produced linear waveform. These models are either Theory Agnostic (TA) or Theory Specific (TS) and may also contain the Price power-law tail [52]. In the models we also vary the number of modes included from, $N = 1$ to $N = 2$. A summary of all the models is given in the Table 6.1.

The TA models make no assumptions for the QNM frequencies included in the waveform and each mode, n , requires four free parameters in order to be modeled. On the contrary, TS models assume certain values for the QNM frequencies that are included in the waveform. The details of each model are described below

- (i.) Φ_N^{TA} : This is a TA model, that makes no assumptions for the QNM frequencies and includes N modes:

$$\Phi_N^{TA}(t - t_{\text{peak}}) = \sum_{n=0}^{N-1} A_n e^{-Im(\omega_n^{TA})(t-t_{\text{peak}})} \cdot \sin\left(Re(\omega_n^{TA})(t - t_{\text{peak}}) + \phi_n\right),$$

$$t \in [t_0, t_f]. \quad (6.2)$$

The parameters that describe each mode are four, the complex frequency $\omega_n = Re(\omega_n) - iIm(\omega_n)$, the amplitude A_n and the phase ϕ_n , leading to $4N$ parameters in total.

- (ii.) Φ_N^{TS} : This is a TS model, which incorporates assumptions for the frequencies and includes N modes:

$$\Phi_N^{TS}(t - t_{\text{peak}}) = \sum_{n=0}^{N-1} A_n e^{-Im(\omega_n^{TS})(M)(t-t_{\text{peak}})} \cdot \sin\left(Re(\omega_n^{TS})(M)(t - t_{\text{peak}}) + \phi_n\right),$$

$$t \in [t_0, t_f]. \quad (6.3)$$

The assumption of the underlying frequency appears in the model through the injection of a frequency ω_n^{inj} and a mass M^{inj} . Specifically, we use the fact the product of the frequency times the mass is constant and in that way we can treat the mass as a free parameter

$$\omega_n^{TS} \cdot M^{TS} = \omega_n^{inj} \cdot M^{inj} \xrightarrow{M^{inj}=1}$$

$$\omega_n^{TS}(M) = \frac{\omega_n^{inj}}{M^{TS}}, \quad (6.4)$$

where the injected mass is set to one.

The parameters that describe each mode are two, the amplitude A_n and the phase ϕ_n . Additionally, the mass M^{TS} , serves as a global parameter that describes and controls the values of the frequencies for all n as shown in (6.4), leading to $2N + 1$ parameters in total.

- (iii.) Φ_N^{TA-t} : This is the same **TA** model as before, that makes no assumptions for the frequencies and includes N modes, but now we also take into account the late-time power-law tail:

$$\Phi_N^{TA-t}(t - t_{\text{peak}}) = \sum_{n=0}^{N-1} A_n e^{-Im(\omega_n^{TA})(t-t_{\text{peak}})} \cdot \sin\left(Re(\omega_n^{TA})(t - t_{\text{peak}}) + \phi_n\right) + A_{\text{tail}}(t - t_{\text{tail}})^{-(2\ell+3)}, \quad t \in [t_0, t_f]. \quad (6.5)$$

The parameters that describe each mode are four, the complex frequency $\omega_n = Re(\omega_n) - iIm(\omega_n)$, the amplitude A_n and the phase ϕ_n and additionally we have two extra parameters to model the tail, $A_{\text{tail}}, t_{\text{tail}}$, leading to $4N + 2$ parameters in total. For our case with $\ell = 2$ and non-static initial data, from equation (3.13), the exponent for the tail is -7 .

- (iv.) Φ_N^{TS-t} : This is the same **TS** model as before, which incorporates assumptions for the frequencies and includes N modes, but now we take into consideration the power-law tail:

$$\Phi_N^{TS-t}(t - t_{\text{peak}}) = \sum_{n=0}^{N-1} A_n e^{-Im(\omega_n^{TS})(M)(t-t_{\text{peak}})} \cdot \sin\left(Re(\omega_n^{TS})(M)(t - t_{\text{peak}}) + \phi_n\right) + A_{\text{tail}}(t - t_{\text{tail}})^{-(2\ell+3)}, \quad t \in [t_0, t_f]. \quad (6.6)$$

The explanation regarding the frequencies and the mass is the same as before. The parameters that describe each mode are two, the amplitude A_n and the phase ϕ_n and additionally the mass is global parameter for all of the frequencies. We also have two additional parameters to model the tail, $A_{\text{tail}}, t_{\text{tail}}$, leading to $4N + 1 + 2$ parameters in total. For our case with $\ell = 2$, the exponent for the tail is -7 .

Model	Description	Number of free parameters	Tail	Legends in plots
Φ_N^{TA}	N free frequencies	$4N$	no	N TA
Φ_N^{TS}	only fixed frequencies	$2N + 1$	no	N TS < TS >
Φ_N^{TA-t}	N free frequencies	$4N + 2$	yes	N TA tail
Φ_N^{TS-t}	only fixed frequencies	$2N + 1 + 2$	yes	N TS < TS > tail

Table 6.1: < TS > = {PT: Pöschl-Teller, GR: Regge-Wheeler}, N : Number of modes. The models taking into account the power-law tails refer only to the **GR** waveforms.

In general, **TS** implies that the assumptions for the frequencies could come from any possible theory. However, in this chapter we focus specifically on the **RW** and **PT** potentials. Accordingly, we make two distinct assumptions: the modes for each waveform correspond either to the Regge-Wheeler potential of equation (2.31) or to the Pöschl-Teller potential of equation (3.16). Regarding the **PT** potential it should be noted that we matched it to the **RW** with the method described in the subsection 3.4.5. The exact values for the former modes

are taken from [77] whereas the others can be computed analytically via (3.18), after the potential matching.

To highlight it again, for each waveform we use two TS models. For the one we assume the correct frequency and for the other we intentionally inject the wrong. In total, we employ six models when we study the PT waveforms which do not contain the power-law tail, since it is not produced by the PT potential, and twelve models when studying the RW waveforms.

A way to measure the performance of each model is to compare its parameters with known values, whenever possible. In our case, we can apply it for two parameters: for the mass M_{fit} , extracted from the TS models

$$\delta M = \frac{|M_{fit} - M_{inj}|}{M_{inj}}, \quad (6.7)$$

where $M_{inj} = 1$, and the frequency

$$\delta \omega = \frac{|\omega_i - \omega_{i,theory}|}{|\omega_{i,theory}|}, \quad (6.8)$$

where $\omega_{i,theory}$ is theoretical value of the complex frequencies corresponding to the underlying potentials which is always known.

B. The fitting procedure

To fit the models to the numerical data, we use PYTHON's `scipy` library and specifically the `curve_fit` function, which employs the Levenberg–Marquardt algorithm to minimize the Sum of Square Error Function, as defined in equation (5.17). For further details see Sec. 5.2. The `curve_fit` function takes some arguments that require special attention. For example, one should provide a priori the boundaries for the parameters. If the boundaries are too narrow, some of the parameters may get constrained by them and thus prevent the optimization algorithm from finding the global minimum. To avoid this, we ensure that the boundaries are wide enough.

All models require a predefined fitting window which starts from $t_0 - t_{\text{peak}}$ and ends at $t_f - t_{\text{peak}}$. This is why, in the definitions of the models we have $t \in [t_0, t_f]$. To determine the fitting window we should specify the starting and ending times. These limits are not strictly defined [78] and for example the choice of t_0 is related to the still ongoing discussion regarding the time of validity of the linear ringdown with respect to the full waveform extracted from numerical relativity simulations [39–41].

The choice of the ending time is more straightforward at first glance. One could say that if we did not want to study the effect of the power-law tail, we could choose an ending time that does not include it, as is done in [39]. To be more precise, it is not that the tail is absent in the early waveform, but rather that the QNMs dominate over it. Observe, for example, that in Figure 6.1, the contribution of the extrapolated tail is ~ 2 orders of

magnitude smaller than that of the QNMs. However, in the following Sec. 6.4, we treat the end time as a free parameter and we see that its impact on the extracted parameters is not so important. This means that for fixed starting time $t_0 - t_{\text{peak}}$, the extraction of the fundamental mode's complex frequency remains more stable as we vary the ending time $t_f - t_{\text{peak}}$, compared to when we vary the starting time instead.

On the contrary, the starting time of the fitting window t_0 , is a bit trickier. There are different approaches to choose it [78]. Here it is treated as a free parameter and to quantify these implications on the performance of the models we define the following quantity

$$\mathcal{M} = 1 - \frac{\langle \Phi_{\text{signal}}, \Phi_{\text{fit}} \rangle}{\sqrt{\langle \Phi_{\text{signal}}, \Phi_{\text{signal}} \rangle \langle \Phi_{\text{fit}}, \Phi_{\text{fit}} \rangle}}, \quad (6.9)$$

where

$$\langle \Phi_{\text{signal}}(t), \Phi_{\text{fit}}(t) \rangle = \int_{t_0}^{t_f} \Phi_{\text{signal}}(t) \cdot \Phi_{\text{fit}}(t) dt. \quad (6.10)$$

which is called *Mismatch*. As the fitted model Φ_{fit} approaches the produced waveform Φ_{signal} , the mismatch approaches zero, which implies that a good fit leads to very small mismatch. Therefore, by changing t_0 , we study how much the models match with the generated waveform by examining the mismatch.¹

Finally, for each t_0 , we need to provide an initial guess for the parameters in order to initiate the optimization algorithm. If this initial guess is close to the actual minimum of the Sum of Square Error Function, the algorithm converges faster to it. So if we make a good initial guess we can speed the process. If we make an extremely bad initial guess we might get stuck on a local minimum and obtain biased parameters.

Assuming that the extracted parameters improve as t_0 increases, since the transient part of the waveform is more and more excluded from the fit, we employ the following procedure, which is shown schematically in Figure 6.2. For the first t_0 we have no previous parameters to rely on. So we draw the initial guess randomly from a uniform distribution, covering the allowed range of parameters. For the subsequent t_0 , based on our assumption that the parameters improve, we replace the uniform distribution with a truncated Gaussian. This adjustment allows us to place more weight on certain regions of the parameter space. This Gaussian is cut at the borders of the allowed parameter range and its mean value is located exactly at the parameters that were extracted from the previous t_0 fit. The width is set to 25% of the range of each parameter. In that way, we speed up the process by starting from a guess that is relatively close to the minimum.

Finally, we repeat the fit for each t_0 at least 50 times, depending on the model, each one with random parameters drawn from the truncated Gaussian, in order to make sure that

¹ There is a possible pitfall in the above. Best-fit functions that differ only up to a constant factor, give the same mismatch, since this factor is canceled out. Therefore, we could have a nearly zero mismatch but wrong best-fit parameters.

the optimization algorithm is not stuck on a local minimum. From these fits, we select the parameters that correspond to minimum mismatch \mathcal{M} .

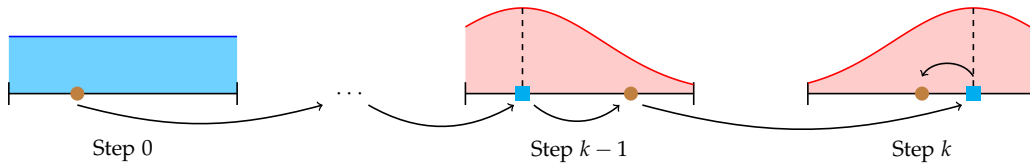


Figure 6.2: The fitting procedure shown schematically. The first step corresponds to the smallest starting time. The initial guess is drawn from a uniform distribution covering all the parameter space. The fitted parameters are depicted by the bullet. The k step corresponds to a larger starting time and uses information from the $k-1$ step. Specifically, the fitted parameters of $k-1$ step (bullet) serve as the mean of the truncated Gaussian distribution from which we draw the initial guess for the fit at step k (blue square at step k).

We remark that, as extensively discussed in [40], a small mismatch is not a panacea; it may also lead to overfitting. The authors show that by including up to $N = 8$ modes in various models, the mismatch is very small, even close to the peak. This seemingly positive result, hides the fact that the robustness of the extracted parameters deteriorates for higher overtones. Consequently, while the fit appears accurate, it may actually be an artifact of overfitting.

6.2 PÖSCHL-TELLER POTENTIAL

The initial application focuses on the study of waveforms generated by the scattering of a Gaussian to the Pöschl-Teller (PT) potential. We perform the fits using TA and TS models, six different in total, defined in equations (6.2) and (6.3) respectively. For the TS we consider frequencies originating either from the PT potential (correct ones) or the RW (incorrect ones). The fits are repeated for different starting times ranging from $t_0 - t_{\text{peak}} = -20M$ to $50M$ with step $1M$ and we plot all the extracted parameters as function of the starting time.

The performance of each model is shown in Figure 6.3, where we plot the mismatches for different starting times of the fit. In the pre-peak region - where the modes have not fully formed yet - all mismatches are large, indicating that the damped sinusoids cannot accurately describe this region of the waveform, as anticipated.

Two general trends can be observed: the mismatches decrease as starting time increases and the mismatches of models with $N = 2$ are smaller than their $N = 1$ counterparts. The first trend can be attributed to the fact that at late enough times, the transient content has vanished and the high overtone content has decayed resulting in the fundamental mode dominating over the signal. The second trend is due to the larger parameter space which provides greater flexibility.

Notably, both Theory Specific models perform similarly at early times. The TS GR models performs worse than the TS PT only at late times, after $30M$ for the $N = 1$ model and $20M$ for $N = 2$ model, where they plateau at almost a constant value of $\sim 10^{-6}$.

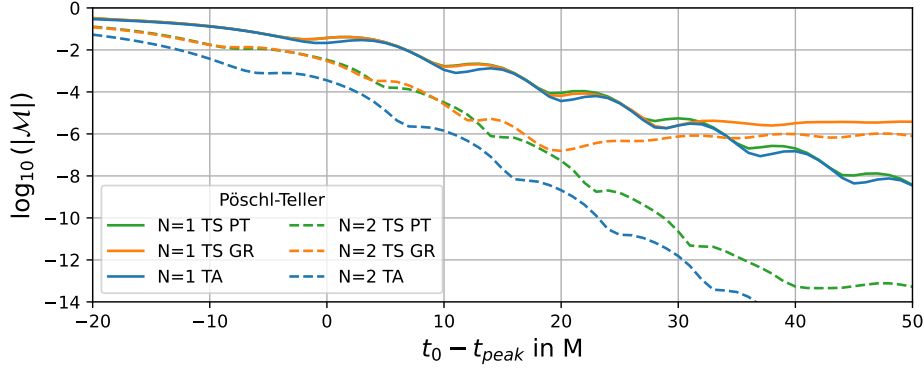


Figure 6.3: Mismatches between the fit and the **PT** generated waveform, as a function of starting time of the fit for the six models, each one containing up to N modes.

Finally, the $N = 2$ TA model seems to perform slightly better than its TS PT counterpart at very late times. A possible explanation for this could be attributed to its larger parameter space, which provides greater flexibility and enables it to better capture the numerical errors, which should be present for such small mismatches [39]. Given the small mismatches obtained, we can infer that our models can fit the waveform reasonably well. From now on, the focus shifts to the quality of the parameter extraction.

We start from the mass, M_{fit} . As shown in the top panel Figure 6.4, all TS PT models approach to the value of 1 and the TS GR models approach a value close to it but not exactly 1. Therefore, TS PT models that assume correct frequencies approximate better the injected mass, whereas the performance of the TS GR models plateaus on a wrong value at $\sim 10M$ and $\sim 30M$ for model containing $N = 1$ and $N = 2$ modes respectively. In the bottom panel we show the relative error of the extracted mass computed from equation (B.10) and we see that its value for TS GR models plateaus whereas for TS PT keeps improving. The somewhat unexpected of these plots is that the TS GR models, which contain the wrong frequency, recover the mass more accurately at early times as shown in the bottom panel.

The next parameter we discuss is the recovered frequency $\omega = Re(\omega) - iIm(\omega)$. Note that the **PT** spectrum has the same real part for all the frequencies. The results for real and imaginary parts are shown in the top and bottom panels respectively of Figure 6.5. The first observation is that for early times and especially before the peak, the predictions deviate a lot from the expected values which are shown with black lines. The convergence to the expected values starts after the peak and especially for late enough times all the models find the correct frequencies, except for the TS GR ones (see the inset which zoom in late-time region).

Again, models that are **TS** converge faster than **TA** but the latter approach closer to the correct frequencies (see Appendix A and Figure A.2). Additionally, the fundamental mode extracted from models containing two modes converge faster than models containing one mode.

In linear perturbation theory, each mode has constant amplitude and phase. There-

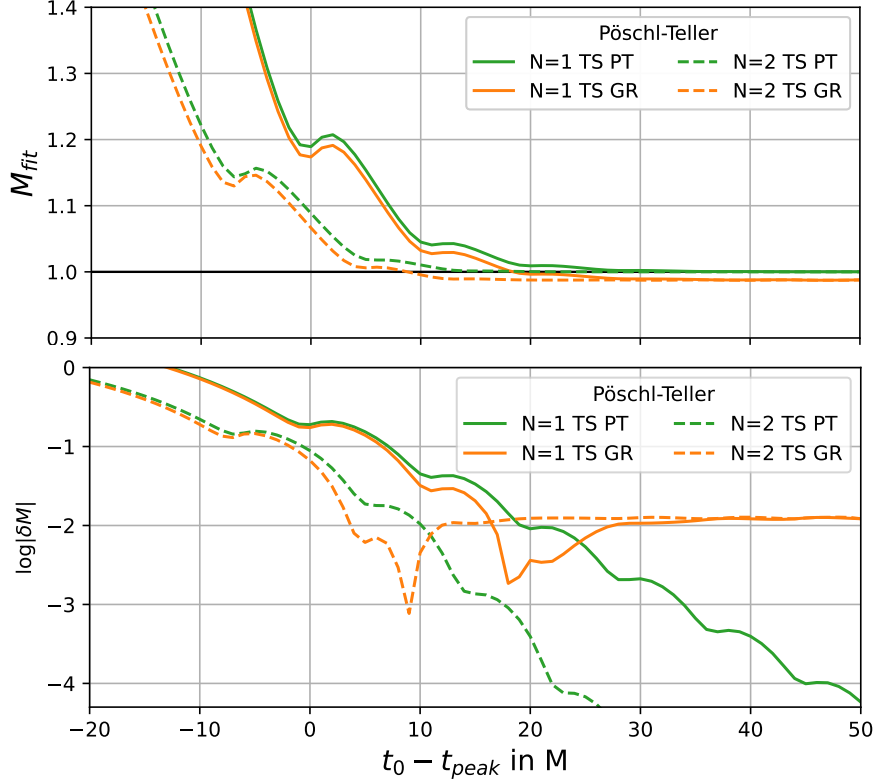


Figure 6.4: Results for the extracted mass as a function of starting time of the fit, using [PT](#) waveform and [TS](#) fit models with $N = 1, 2$ modes. *Solid lines* refer to models with $N = 1$ mode and *dashed lines* to models with $N = 2$ modes. **Top panel:** Value of extracted mass. **Bottom panel:** Relative error of the extracted mass computed with respect to the injected one which is equal $M_{inj} = 1$.

fore, to claim that a mode is found in a signal, its amplitude and phase should also be robustly extracted. These parameters are not as fundamental as the frequencies themselves since they depend on the Initial Condition used to produce the waveform. Though, the stable extraction of the frequency alone, does not guarantee the finding of the mode. In Figure 6.6 we plot the amplitudes for the fundamental mode A_0 and the first overtone A_1 (see Appendix A and Figure A.1 for the corresponding plots for the phase). The amplitude for the fundamental mode is extracted in a stable and constant manner at late times from all the models, certifying the convergence of the mode. However, for the first overtone, the amplitude becomes constant only for very late times only for TA and TS PT models and for the TS GR diverges, which means that this specific model failed to find the first overtone of the signal.

A final general comment can be made, on the fact that TS GR models predict wrong frequencies quite well and robustly. This means that if we did not know the correct underlying spectrum of the waveform and we assumed that it came from a GR potential we could possibly be satisfied with the results if we did not have many models to compare. Therefore, this could serve as a toy-example for biased model. For wrong assumptions, that is GR frequencies for a PT waveform, the extracted parameters were stable, though wrong.

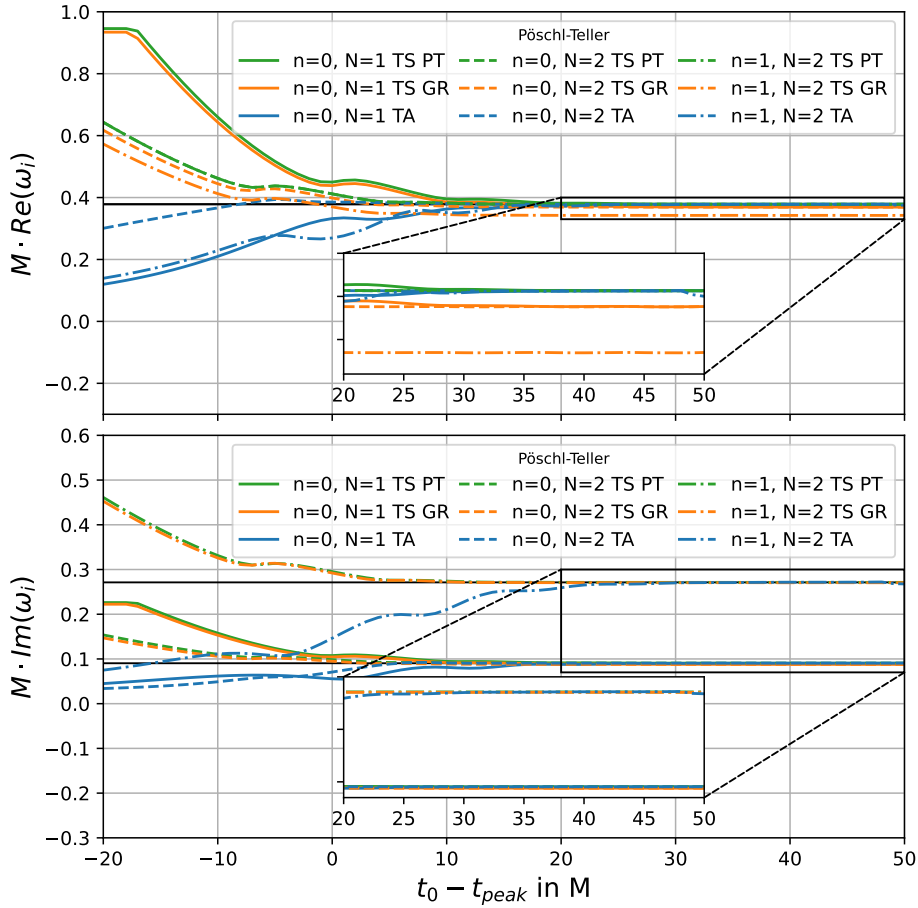


Figure 6.5: Results for the extracted frequencies from a **PT** waveform as a function of the starting time of the fit $t_0 - t_{\text{peak}}$. **Top panel:** Real part of ω . **Bottom panel:** Imaginary part of ω . *Solid lines* correspond to models containing $N = 1$ mode and the two types of *dashed lines* correspond to models containing $N = 2$ modes. The black lines correspond to the expected values. Specifically of the imaginary part, the lower black line refers to the fundamental mode and the upper to the overtone. The inset windows show the stable extraction of all modes from all models at late enough times.

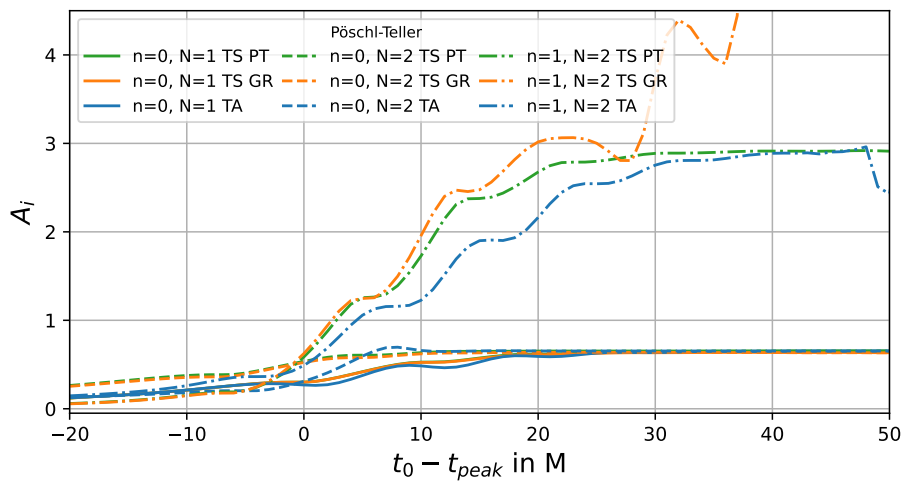


Figure 6.6: Amplitudes of the modes as a function of the starting time of the fit for the **PT** waveform. *Solid lines* correspond to models containing $N = 1$ mode and the two types of *dashed lines* correspond to models containing $N = 2$ modes.

6.3 REGGE-WHEELER POTENTIAL

The second application is a repetition of the previous calculations but for the *RW* potential. The main difference between the two cases, is that the *RW* has different asymptotic behavior which leads to a late-time tail. As we will discuss, this deteriorates the extraction of the parameters. Possible solutions for this could be to include the tail in the models or to exclude the tail from the fitting window. As we will see in more detail in Sec. 6.4, the first works whereas the second does not.

We use all the *TA* and *TS* specific models defined in equations (6.2), (B.8), (6.3) and (B.9), with included modes $N = 1$ or $N = 2$ and we also take into consideration the tail. In total we employ twelve different models. As before, for the *TS* ones, we consider both the correct *GR* frequencies and the wrong *PT* ones and we repeat the fits from $t_0 - t_{\text{peak}} = -20M$ to $60M$ with step $1M$.

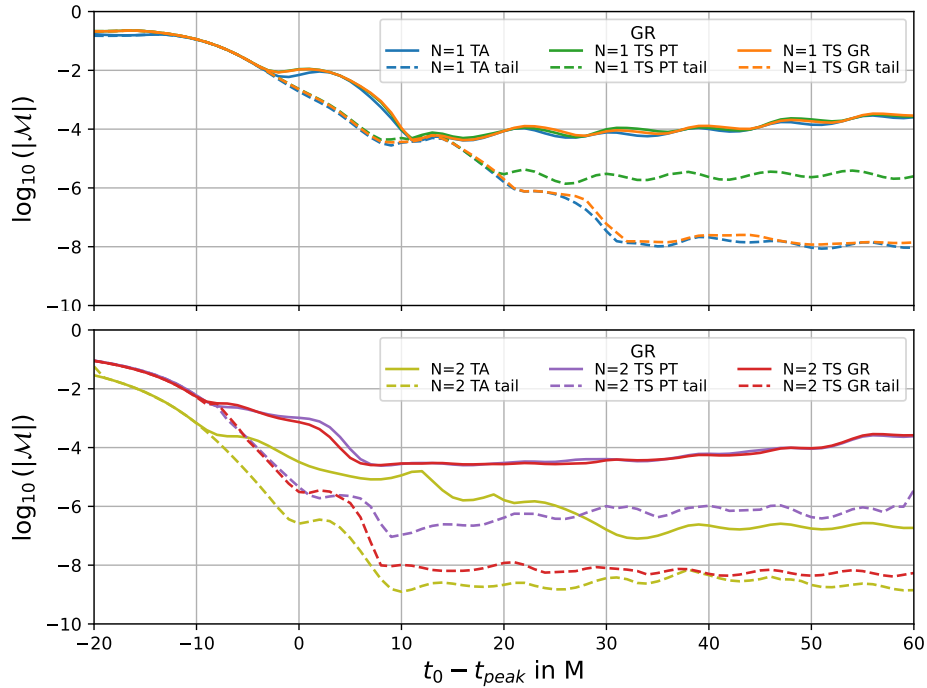


Figure 6.7: Mismatches between the *GR* waveform and the suits, as a function of the starting time of the fit. **Top panel:** Shows models with one mode. **Bottom panel:** Shows models with two modes. For both panels, the *solid lines* refer to models that do not include the late-time tail and *dashed lines* to models that include it.

First come the mismatch plots in Figure 6.7, which yield similar behavior as before, indicating the agreement between the fitted function and the numerical waveform. All models with $N = 1$ mode (solid lines at the top panel), perform quite similarly. Observe the minimum around $t_0 - t_{\text{peak}} \simeq 10M$ and the ascending behavior afterward. We did not observe such a behavior for the *PT* waveform, so it can be attributed to the late-time tail. Indeed, when we model the tail (dashed lines at the top panel), the mismatches decrease from two to four orders of magnitude (depending on the model) and at the same time no ascending tendency is observed.

Similar is the behavior of the $N = 2$ mode fits. The difference here is that they reach the minimum mismatch earlier than their $N = 1$ counterparts, since they capture better the first overtone that is present earlier at the waveform and has decayed in later times. The indication from the mismatch plots is again, that the models fit quite well the signal and from now on we discuss about the relation of small mismatch with the quality and stability of the extracted parameters.

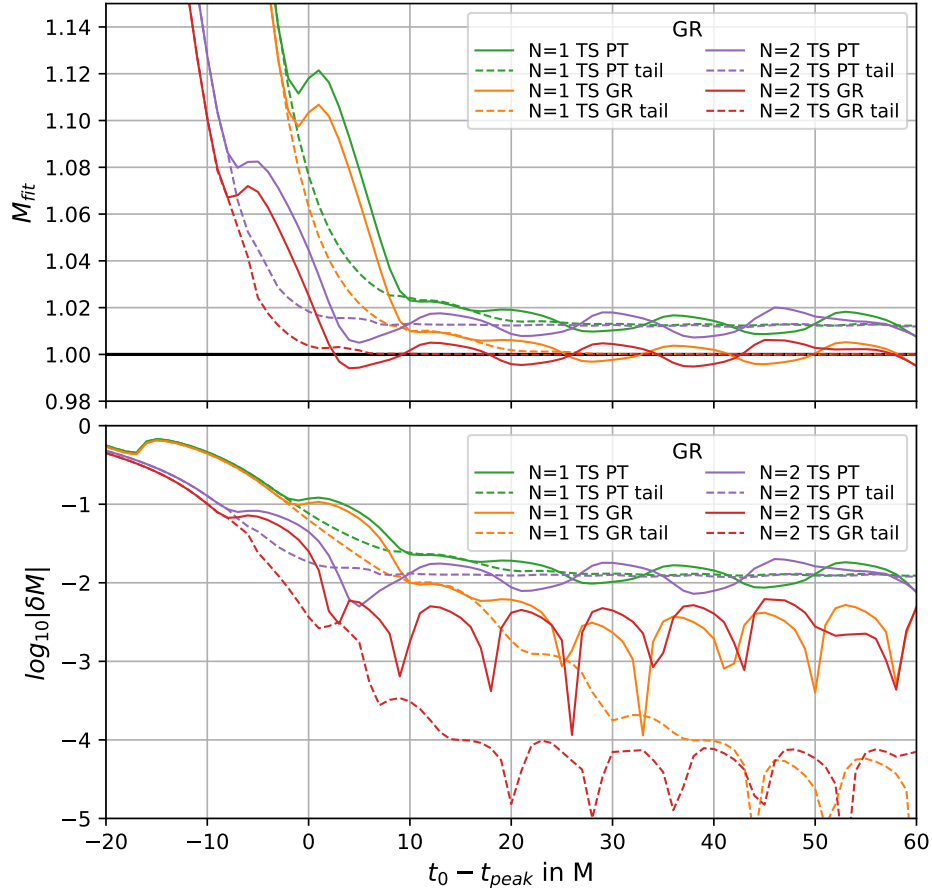


Figure 6.8: Results for the extracted mass as a function of starting time of the fit, using GR waveform and TS fit models with $N = 1, 2$ modes and tails. **Top panel:** Value of the extracted mass. The black line indicates the injected mass $M_{inj} = 1$. **Bottom panel:** Relative error of the extracted mass with respect to the injected mass which is equal to $M_{inj} = 1$. At both panels, the *solid lines* refer to models that do not include the late-time tail and *dashed lines* to models that include it.

We now turn to the extracted mass, shown in Figure 6.8, bringing us to the new point where the improvement provided from the modeling of the tail becomes more clear. In the top panel we plot the extracted mass M_{fit} as a function of the starting time of the fit and on the bottom panel, its relative error. Note that models without the tail (solid lines both in top and bottom panels) oscillate around a certain value. The TS PT ones with the wrong frequency, find a wrong value with relative error $\sim 10^{-2}$, whereas the TS GR that contain

the correct frequency, oscillate around the correct value of 1, with approximately one order of magnitude smaller relative error.

This oscillating plateau, even for the model containing the correct frequencies, is in contrast with the corresponding Figure 6.4 for the PT waveform. The difference is due to the presence of the power-law tail that limits the continuous improvement of the mass value at around $t_0 - t_{\text{peak}} \gtrsim 10M$ to $20M$ for different models.

However, when we explicitly model the late-time tail (dashed lines), we observe even by eye at the top panel that the extracted mass stabilizes around the wrong value for TS PT models and around the correct value from TS GR ones. From the bottom panel we see that in fact, regarding the TS GR the oscillation of the relative error is smaller by two orders of magnitude.

Also, the general trends are that models with two modes and models with tails reach their 'final-state', either oscillating or constant, faster than models with one mode and models without tails. The extraction of the mass overall, is quite reasonable, since it does not diverge, it is stable and additionally, the different results between different models can be reasonably explained.

At this stage, we must elaborate on a point that, once observed, could be classified into the 'not even wrong' category. Specifically, two of the models employed are TS PT with a tail. That is, in a theory-specific model, whose spectrum is assumed to emerge from a tail-less potential, a late-time tail is included. Conceptually, this is completely incorrect. However, there is an explanation for that and it offers something of value.

If we momentarily neglect the tail-less character of the PT spectrum and consider these injected frequencies simply as two frequencies that are different from the ones included in the signal, what we observe is an interesting point. The combination of the tail with the wrong frequency improves the fit by decreasing the mismatch as seen in Figure 6.7 and stabilizing the extraction of the mass as seen in Figure 6.8. So the correct modeling of some parts of the signal leads to more stable results, even though wrong frequencies are assumed.

We now discuss the extraction of the frequencies shown in Figure 6.9, where in the left and right column we see the complex frequencies of the fundamental mode and first overtone respectively. There is also its counterpart, Figure 6.10, which shows the relative errors of the complex frequencies defined in equation (B.11). This discussion illustrates again the improvement that comes along with the modeling of the tails and also exposes the problematic features of some models.

Regarding the fundamental mode (left column), all TS PT models, predict a wrong value with $\sim 2\%$ relative error and all the others approach the correct values with at least one order of magnitude smaller relative error. Note that frequencies from the models without the tail (solid lines) oscillate around a certain value. The exception is the 2 TA model,

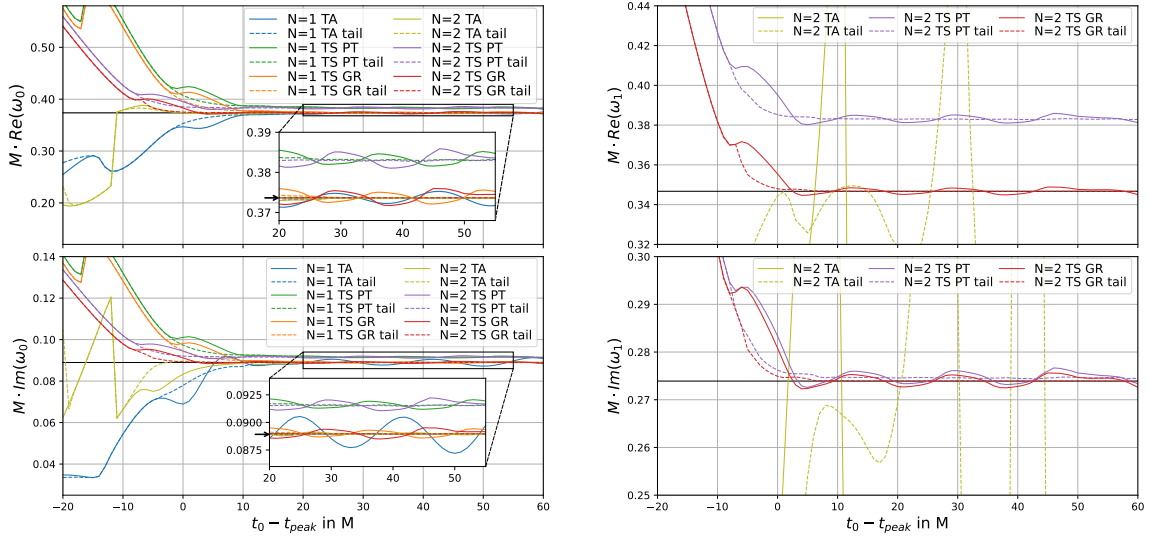


Figure 6.9: Results for the extracted frequencies as a function of starting time of the fit, using GR waveform. The black lines at the main axes and the black arrows at the insets indicate the expected values. The black arrows on the insets show the expected values. **Left column:** Real and imaginary parts of the fundamental mode. **Right column:** Real and imaginary parts of the first overtone. At all panels, the *solid lines* refer to models that do not include the late-time tail, and the *dashed lines* to models that include it.

which stabilizes the extraction of the frequency of the fundamental mode (see the yellow line on the inset of Figure 6.9 and Figure 6.10).

The first overtone frequencies (right panel) are extracted in a stable manner for the TS models (again wrong value for TS PT and correct for TS GR). This is due to the fact that they are the ratio of the assumed frequency over the extracted mass, which is robustly extracted with different accuracy depending on the model. However, the TA model is extremely unstable and does not recover the overtone at all (yellow line).

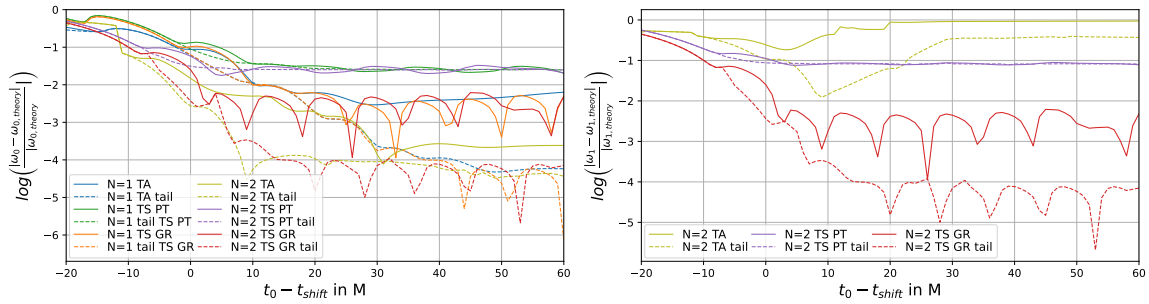


Figure 6.10: Relative errors of the extracted frequencies defined in equation (B.11), as a function of the starting time of the fit. **Left panel:** Fundamental mode results **Right panel:** First overtone results

If no further plots were shown, one could infer that all the TS models can robustly extract the first overtone from the signal. Figure 6.11, shows the extracted amplitudes as a function of the starting time. On the left panel we show the results for the fundamental mode, A_0 , which has similar behavior with the other parameters. The models that neglect the tail oscillate at late times around a certain value, models that include the tail stabilize

the extraction and models including the overtone also stabilize the extraction, but less. Additionally, the TS PT models, yield slightly different value from all the others.

On the right panel of the figure, we see that none of the amplitudes for the first overtone is robustly found. All of them deviate to large values at late times. Thus we cannot safely infer that we detected the first overtone in this specific produced signal with the procedure followed. If we compare with the corresponding results from the *PT* waveform where only the 2 TA model failed to detect the overtone (Figure 6.6), we can trace the reason of this difference back to the power-law tail. Similar results for the phases can be found in the Appendix A at Figure A.3.

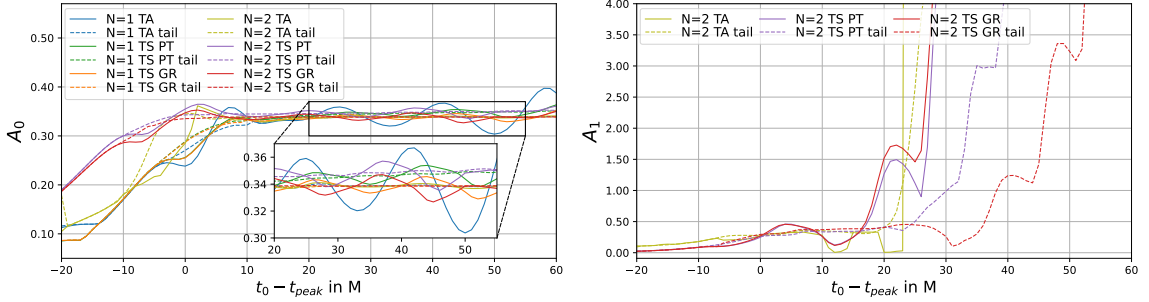


Figure 6.11: Amplitudes as a function of the starting time of the fit. **Left panel:** Fundamental mode results. **Right panel:** First overtone results.

Finally, we discuss whether the extraction of the tail was robust or not and we present relative results in Figure 6.12. Both its amplitude and its pole, were found to have similar behavior. For early times, up to $t_0 - t_{\text{peak}} \sim 10M$, the parameters are quite unstable meaning that its contribution to the signal is not so large compared to other contributions such as the transient phase and the higher overtone content at the early post-peak times. That is reasonable since the tail is a late-time effect of the linear ringdown.

However, after $t_0 - t_{\text{peak}} \sim 20M$ for the $N = 1$ mode models and $t_0 - t_{\text{peak}} \sim 10M$ for the $N = 2$ mode models, we observe either an oscillating behavior around a certain value or a convergence to a constant value, respectively. An intuitive explanation for this difference could be that the $N = 2$ mode models capture better the oscillating part of the signal therefore leaving a signal which contains a more clear form of the tail.

In the first paragraph of this section we talked about an other solution to improve the oscillating behavior of the extracted parameters. This was to decrease the end time of the fit window in order to exclude the tail from the fit. From the Figure 6.12, we can infer that this might not work, since the tail was robustly extracted from $t_0 - t_{\text{peak}} \sim 10M$ to $20M$ depending on the model.

However, this might be a pitfall since the tail extraction might depend on the initial data which is something that we do not examine in this thesis. Additionally, it could be that if we keep including more and more modes in the models, we extract the tail parameters robustly even around, or before the peak. This would mean that the late-time tail exists in these early-time regimes of the ringdown. Therefore, there is no point in shrinking the

end time to such early times, before $10M$ or $20M$. This would include just a small portion of the signal leading to small mismatch and large relative error.

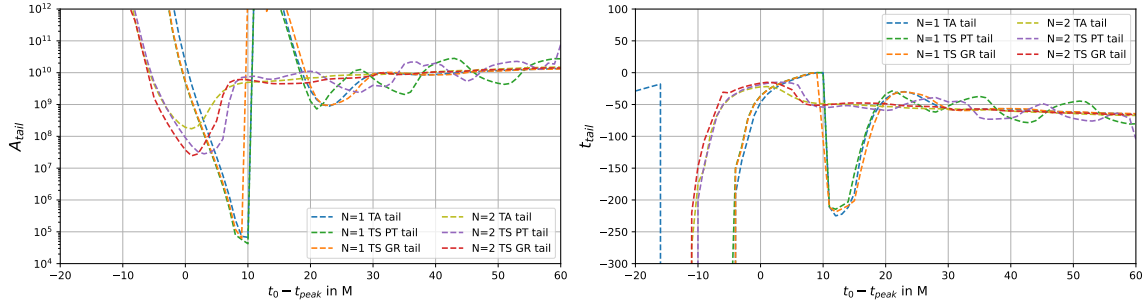


Figure 6.12: Tail parameters as a function of the starting time of the fit. Note that we modeled the tail as $A_{tail}(t - t_{tail})^{-7}$. **Left panel:** Tail amplitude in log scale, **Right panel:** Tail pole, its location is found $\sim 50M$ prior to the waveform peak.

6.4 IMPACT OF THE FITTING WINDOW END TIME

To conclude this chapter, we examine the sensitivity of the extracted frequencies to the boundaries of the fitting window. Specifically, we fit a waveform generated by the [RW](#) potential and perform the fit by using only one model containing the fundamental mode without a tail. We treat both limits of the window as free parameters by varying them in the ranges shown in Figure 6.13. The green area represents the range of the starting time t_0 and the red area the range of the ending time of the fit, t_f . We ensure that they do not overlap, meaning that the ending time never comes earlier than the starting.

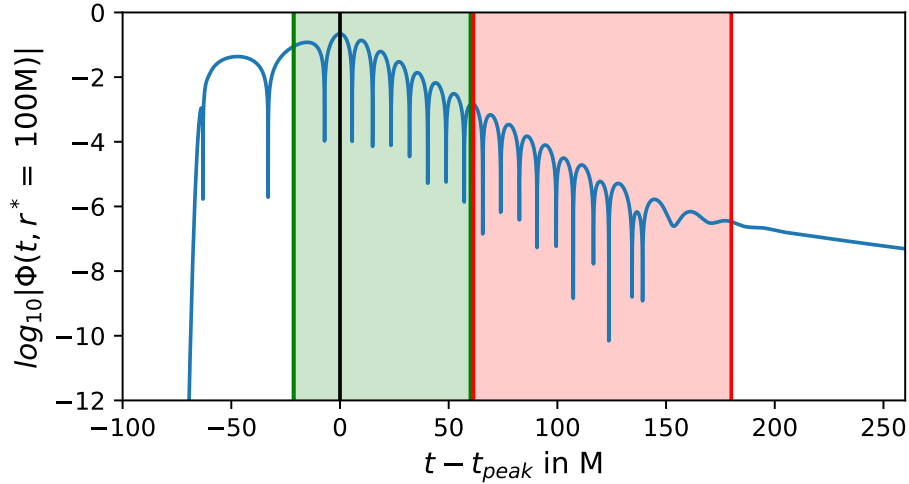


Figure 6.13: Shows the ranges of the two ends of the fitting window treated as free parameters. The range of the starting time is shown in *green* shading, $t_0 - t_{peak} \in [-20, 50]$ and the range of the ending time in *red*, $t_f - t_{peak} \in [60, 170]$. The *black* vertical line indicates the peak of the waveform.

First, as usual, we show a mismatch plot in Figure 6.14. On the vertical axis, we plot the end time of the window and on the horizontal axis the starting time. Both of them are with respect to the waveform's peak. The color scale represents the mismatch value, where

yellow indicates a large mismatch and purple indicates a small one. By picking a constant ending time, observe the oscillation of the mismatch similar to the behavior seen in the previous Chapter in Figure 6.7. In contrast, if we pick a constant starting time and follow a vertical straight line, there is no oscillation visible on the figure. Therefore, the range of the ending time of the window that we pick, seems to have little impact on the mismatch.

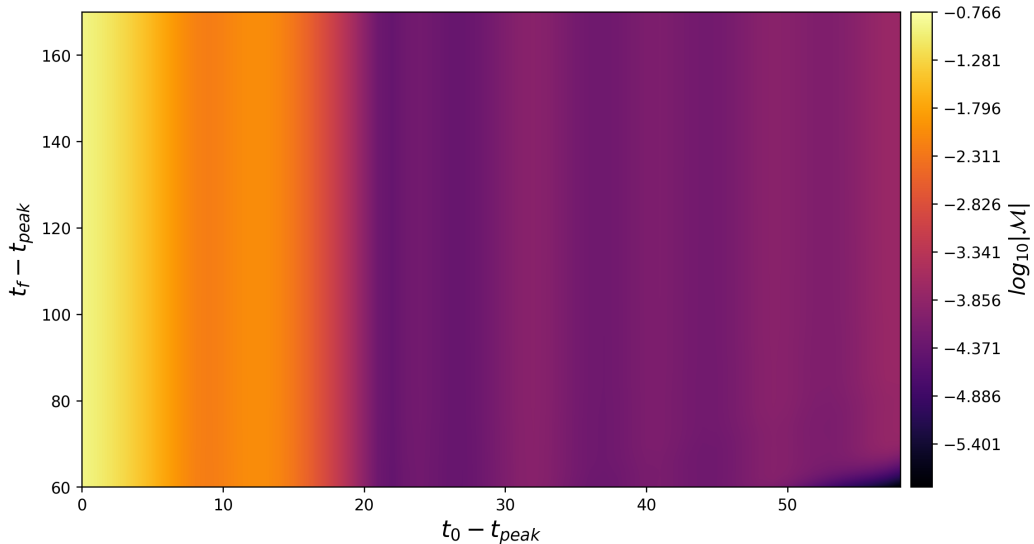


Figure 6.14: Results of the mismatch by letting both ends of the fitting window free. The horizontal axis shows the starting time $t_0 - t_{\text{peak}}$ and the vertical line the ending time of the fit $t_f - t_{\text{peak}}$, both relative to the waveform's peak. The color scale reflects the mismatch values on a logarithmic scale, with yellow being large and purple being small.

Next, in Figures 6.15 and 6.16, we present contour plots with a similar structure to 6.14, but instead of the mismatch we show in color the relative error of the real and imaginary parts of the fundamental mode. To further illustrate the apparent independence of the fit's end time, next to each contour plot, we show some slices of it.

In the top panel, we show slices with constant end times $t_f - t_{\text{peak}}$ and in the bottom panel slices with constant starting time $t_0 - t_{\text{peak}}$. Observe in the top panel that the curves related to different end times (distinguished by different colors) almost overlap with each other and that they vary as a function of t_0 . Similarly, in the bottom panel, the curves corresponding to different starting times (depicted with different colors) reach a constant value after a certain $t_f - t_{\text{peak}}$ but a different one for each $t_0 - t_{\text{peak}}$. This behavior suggests that, for the waveform generated from this specific initial data, the choice of the end time of the fitting window has small impact on the accuracy of mode extraction. The variation in $t_f - t_{\text{peak}}$ neither significantly improves nor deteriorates the extraction of the fundamental mode.

Finally, we provide some general comments on the figures above. The negative values of t_0 were excluded in order to improve the readability of the colormap and since no modes are present in that region yet, this exclusion is not of great importance.

Also in the bottom right corner of Figure 6.14 there is a purple region indicating very small mismatch. This results from the fitting window being very narrow ($\sim 10 - 20M$). For that reason the fitting model can closely match the signal but fails to accurately capture the

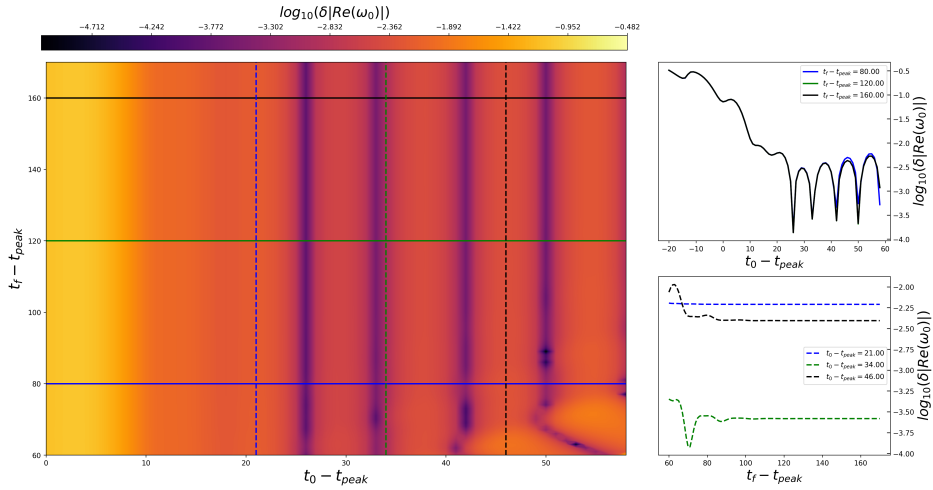


Figure 6.15: Results for the relative error of the real part $\delta Re(\omega_0)$, **Left panel:** The colormap on the corresponds to the relative error, with purple being small and yellow being large. **Right top panel:** Slices of the colormap with ending time $t_f - t_{peak}$ constant. **Right bottom panel:** Slices of the colormap with starting time $t_0 - t_{peak}$ constant.

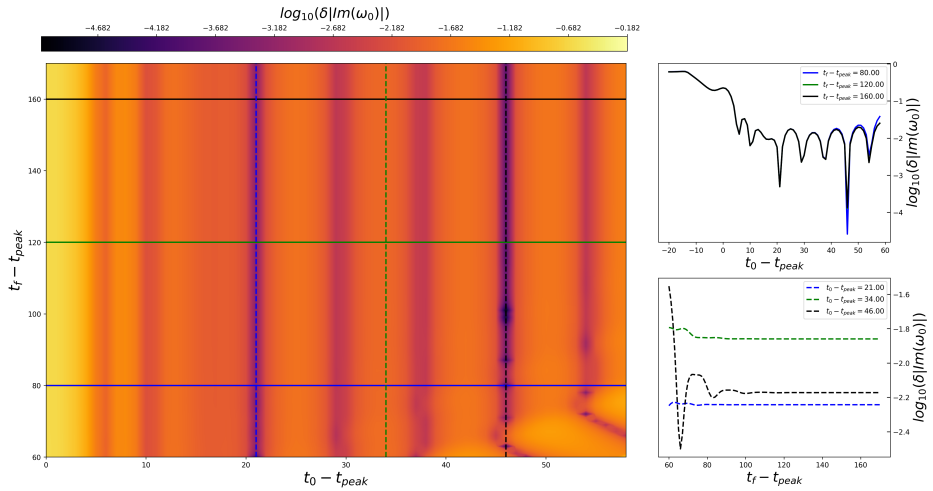


Figure 6.16: This figure has the same layout as Figure 6.15. Relative errors of the imaginary part $\delta Im(\omega_0)$.

modes. This can be observed in the same region of Figures ?? and 6.16 where the contour is distorted and the relative errors relatively large.

FUTURE WORK

Something that is not examined in the above is the correlation of each mode's excitation with the parameters of the initial Gaussian. It is intuitive to expect dependence on the amplitude and the width. For example, if we pick an amplitude much larger than the pick of the potential, possibly the Gaussian would be barely affected by the presence of the potential. Also, as Vishveshwara showed [37], a very narrow Gaussian fully penetrates the potential and a very thick is totally reflected. Therefore it is expected that they will also excite differently the QNMs. However, it would be interesting to examine if the QNMs are

excited differently when we put the Gaussian in the region where the potential is not very small, namely around its peak and also change the initial condition for the derivative.

Also it would be interesting to examine if we can control the excitation of the modes or the tail if we prepare more complicated initial data.

Chapter Summary

In this chapter, we discussed the following key points:

- Various models to fit the generated waveforms, which can be either Theory Agnostic or Theory Specific and may include the late-time tail.
- The fitting procedure of varying the starting time of the fit and selecting the best-fit results by optimizing the mismatch.
- Application to the Pöschl-Teller potential, from which we can infer
 - Stable extraction up to $N = 2$ modes from all the models, except for the 2 TA.
 - The choice of an incorrect frequency in the Theory Specific models yields stable but inaccurate extraction of the mass.
 - Including one overtone improves the obtained mismatches and the convergence of the parameters of the fundamental mode to their final value.
- Application to the Regge-Wheeler potential, from which we can infer:
 - The late-time tail induces oscillations in the extracted parameters at late times, if it is not included in the model,
 - Modeling the tail stabilizes the extraction of parameters
 - Inclusion of one overtone stabilizes the extraction of the parameters of the fundamental mode.
 - The first overtone was not extracted in a stable manner from any of the models.
 - The parameters of the tail showed an oscillatory behavior for late times only for the wrong TS PT models and were stable otherwise.
- It was observed that allowing the end time of the fitting window to be a free parameter neither improves nor deteriorates the accuracy of the extracted frequencies.

APPLICATIONS & RESULTS II

In this chapter we present the second set of results, focusing on the phenomenological extension to GR ringdown, also known as Parametrized Quasi-Normal Mode Framework (PF). Similarly as before, we generate linear ringdown waveforms but on top of the GR potential, we add modifications of $1/r$ powers and we extract the parameters by fitting damped sinusoids with tails. First, in Sec. 7.1, we consider modifications just on the axial perturbations, adding one modification at a time and afterward in Sec. 7.2, we add many modifications simultaneously, testing in that way the limits of PF at the time-domain.

7.1 SINGLE MODIFICATION AT A TIME

In the first application we add a single inverse power of r modification to the axial GR potential. The scalar and polar modifications behave qualitatively the same. Single modification in equation (4.6) means that the potential becomes

$$V(r) = V^{GR}(r) + \frac{1}{r_H^2} \alpha^{(k)} \left(\frac{r_H}{r} \right)^k. \quad (7.1)$$

Therefore the modification is totally controlled by two parameters, its amplitude $\alpha^{(k)}$ and the exponent k , for which we consider $k = 2, \dots, 7$. The objective is to sketch the connections between these two parameters and the properties of the waveforms which, if treated inversely, lead to the properties of the underlying potential.

The method we follow is the same as the one presented in Section 6.1. In brief, we generate a waveform coming from the same initial data but from the modified potential, we extract the time-domain signal by fixing the location of an observer and we fit the Theory Agnostic model of equation (B.8), containing one damped sinusoid and a tail. We perform the fit for different starting times, for each one we repeat at least 100 times and we keep the optimum fit that provides the smallest mismatch. The reason we include the tail in the fits, can be traced back to Section 6.3. There, in all figures the blue solid lines refer to the $N = 1$ TA and the blue dashed lines to the $N = 1$ TA tail model. The $N = 1$ TA tail model provides more accurate and more stable results.

Additionally, in Appendix B, we present some Figures of the same analysis but for a model including only the fundamental mode without the tail.

As a first indication for the success of the fits, we show in Figure 7.1 the mismatches as a function of the starting time. Different powers of $k \in [2, 7]$ are shown in each panel

and different values for the amplitudes, $\alpha^{(k)} \in [-1.5, 1.5]$ are shown in the colorbar. The behavior of the mismatches is similar, except for the $k = 2$ with negative amplitudes where we observe some outliers.

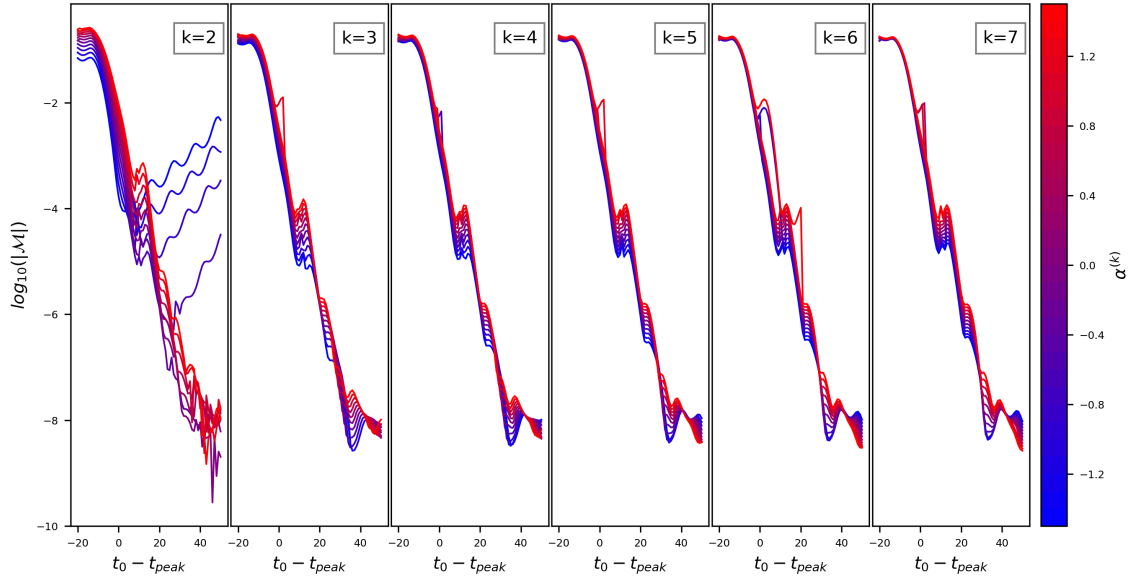


Figure 7.1: Mismatches between fit results and the generated waveforms of the same initial data, as a function of the starting time. Each panel shows different power of k and the colorbar indicates the value of the amplitude varying from $\alpha^{(k)} = -1.5$ (blue) to $+1.5$ (red).

From now on we turn to the quality of the extracted parameters. In Figure 7.2 we present the best-fit results for the fundamental QNM as a function of the modification's amplitude, $\omega_0(\alpha^{(k)})$. Specifically, different panels refer to a different power k and different markers refer to two different starting times $t_0 - t_{peak} = 10M$ and $30M$. The red line corresponds the perturbative theoretical prediction at quadratic order as calculated in [70]. With the gray shaded region, we show the difference between the linear and the quadratic predictions and in that way indicating the systematic error coming from the incorporation of the quadratic correction on top of the linear.

Note that the extracted QNMs agree with the prediction for the late time points (blue circles). The only disagreement can be seen for negative values of $\alpha^{(2)}$. The most probable reason is related to the vertical black dashed lines. These lines come from equation (4.4) and indicate a *rough estimate* of the largest value of each $\alpha^{(k)}$, under which the PF is supposed to be accurate. The lines for $k \geq 4$ are beyond the limits of the axes. This upper bound shows the region that the framework should work. It does not mean that it will not work beyond it. We observe that in general, the framework works even beyond these lines with the only exception this small range of $\alpha^{(2)}$.

Note that for the given range of amplitudes, the change of the real part becomes smaller as k increases. This is intuitive, since larger k brings smaller modification to the potential, thus smaller deviation on the real part. On the contrary, the behavior of the imaginary part is not the same and in fact is the opposite, large k alter it more from the GR value than small k do.

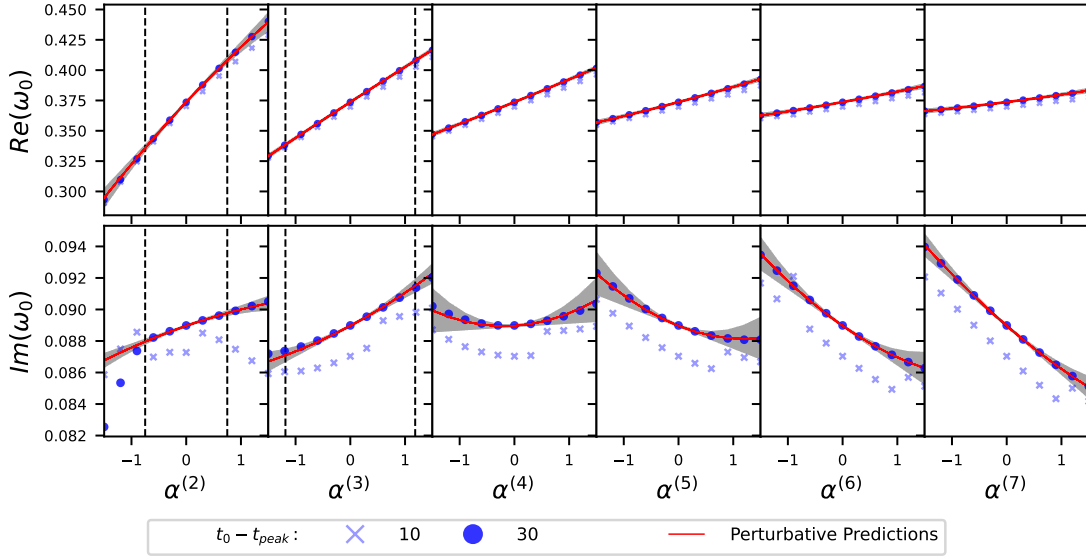


Figure 7.2: Results for the extracted frequencies as a function of the amplitude $\alpha^{(k)}$, for two starting times indicated by two different blue markers. **Top panel:** real part. **Bottom panel:** imaginary part. Each *vertical panel* refers to a different power $k \in [2, 7]$. *Red lines:* quadratic perturbative predictions *Gray errorband:* systematic error coming from the quadratic correction on top of the linear. *Vertical dashed lines* refer to the upper bounds of the amplitudes, under which the framework should be accurate. These lines are not shown for the last four k 's since they are outside of the range of amplitudes.

In Figure 7.3 we have a plot with the same structure as 7.2, where we show the relative errors (given in equation (B.11)) between the extracted and the predicted frequencies as a function of the modification amplitude, $\delta|\omega_0|(\alpha^{(k)})$. Different colors represent different starting times of the fit.

Observe the two behaviors of the relative error. The first is that it is reduced as the starting time increases, which was already observed at the GR case of previous chapter (specifically see Figure 6.10). The second tendency is that the smallest relative errors are obtained in the proximity of $\alpha^{(k)} \simeq 0$, where the modification is small. This implies that the PF works better in that region, since its predictions are closer to the ones extracted from the time evolution. That is expected, since small amplitudes yield smaller deviation from GR so the condition (4.4) is more effectively fulfilled.

The next two Figures ?? also have the same layout and show the amplitude and phase of the fundamental mode as function of the amplitude of modification $\alpha^{(k)}$ (left) and the amplitude and pole of the tail (right).

Observe that the amplitude and phase of the mode are modified differently. For negative $\alpha^{(k)}$ the amplitude decreases and the phase increases with respect to its GR value (at $\alpha^{(k)} = 0$) and inversely for positive amplitudes. Also, their difference from the GR value ($\alpha^{(k)} = 0$) is mitigated as k increases. That is expected because, a certain value of $\alpha^{(k)}$ introduces smaller modification for a large k than for a smaller one.

On the right figure we see that for a given modification amplitude, the tail parameters are the same for all the powers of k except for $k = 2$. The reason for this disagreement is that the exponent for all the tail fits was kept constant and equal to -7 . However, the

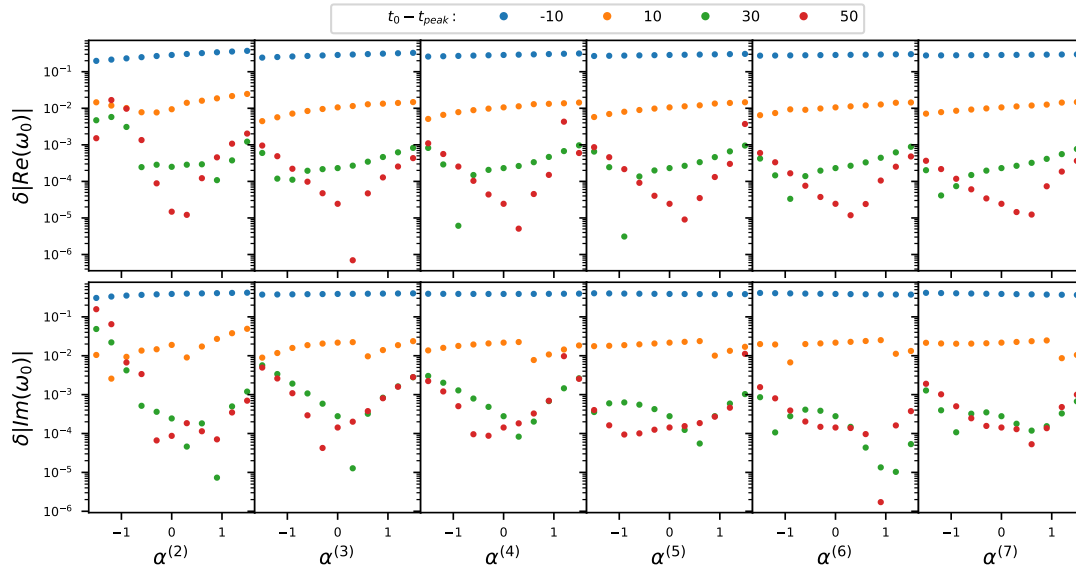


Figure 7.3: Relative errors between the extracted frequencies and the quadratic predictions of the PF. This figure has the same structure as Figure 7.3. Each different color shows a different starting time.

$k = 2$ modification alters this exponent as a function of its amplitude, thus we employed the wrong model for this power of modification and we did that for the sake of comparison between all the different modifications. Observe that for all the other values of k the same tails are found robustly.

The next Figure 7.5 has the purpose of illustrating the parameters' deviation of the GR value. Again, each column refers to different $k \in [2, 7]$ and the horizontal axes are the amplitudes. On the vertical axes we plot in different colors the fitted parameters over their GR counterparts. We observe that for the smallest k (largest modification), the parameters change the most. Then, for ascending k , the modification is shrinking in the same manner for the three parameters, $Re(\omega_0)$, A_0 , ϕ_0 . The imaginary part, shows a different behavior and its modification is larger for larger k .

The solid lines shown in the previous figures, emerge from fitting on the points of same color. The fit uses cubic polynomials $f(\alpha^{(k)}) = \beta \cdot (\alpha^{(k)})^3 + \gamma \cdot (\alpha^{(k)})^2 + \delta \cdot (\alpha^{(k)}) + \epsilon$. Figure 7.6 shows these coefficients as a function of k for all the parameters of the fundamental mode. As we see, the cubic coefficients β are almost zero for all the parameters and k . Also, for all the parameters, except for the real part, the quadratic coefficient γ is non-zero and for all of them the linear coefficient δ is non-zero. Meaning that for the amplitudes of the modification that we chose, the correction to all the parameters is quadratic whereas for the real part is linear. That is the reason why in Figure 7.3 the relative error of the real part is smaller than the corresponding of the imaginary.

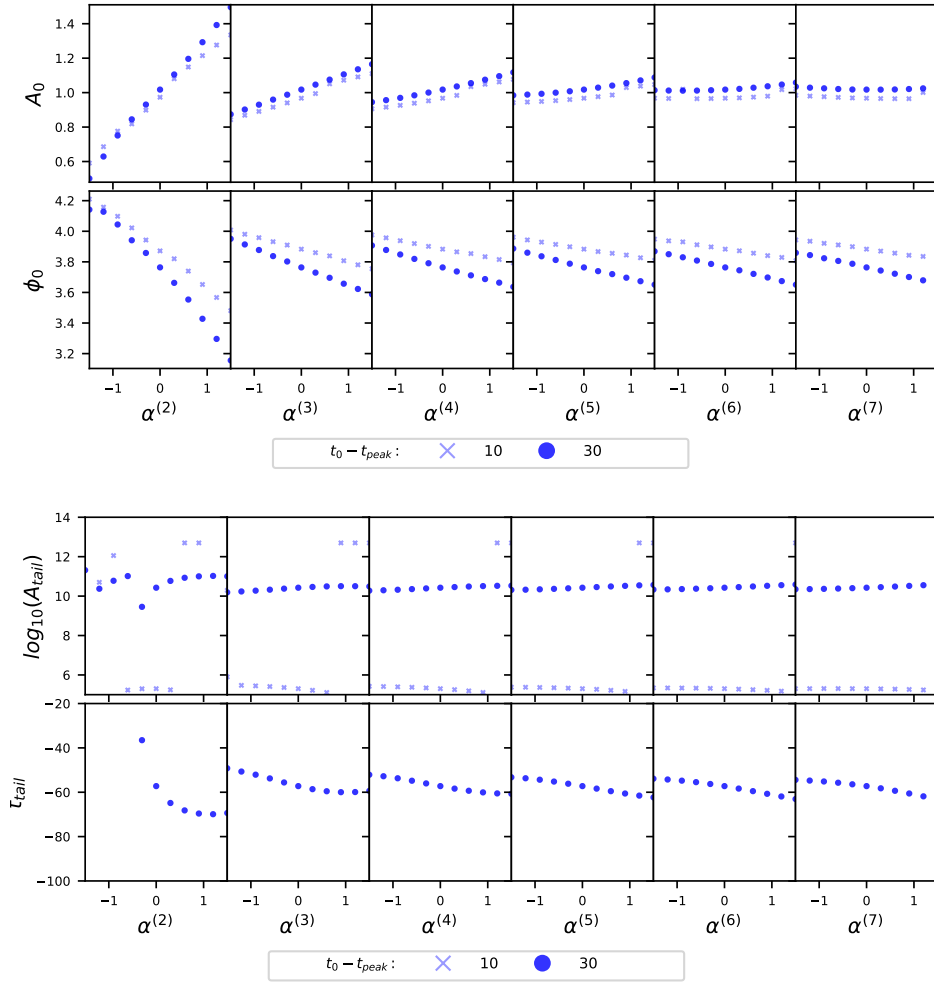


Figure 7.4: This figure has the same structure as Figure **Upper figure**: Amplitude and phase of the extracted fundamental mode for different modification amplitudes and powers. **Lower figure**: Amplitude and pole of the tail for different modification amplitudes and powers.

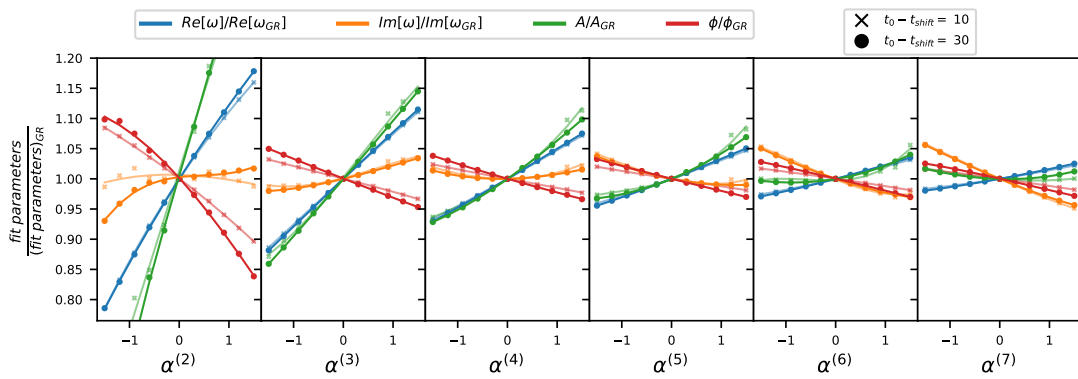


Figure 7.5: Each panel refers to a different power k . Horizontal axes refer to different modification amplitude and vertical axes show the ratio of the fitted parameters over their fitted GR counterparts. Each color depicts a different parameter and each symbol an other starting time of the fit. The solid lines are the result of the cubic polynomial fitting on the points.

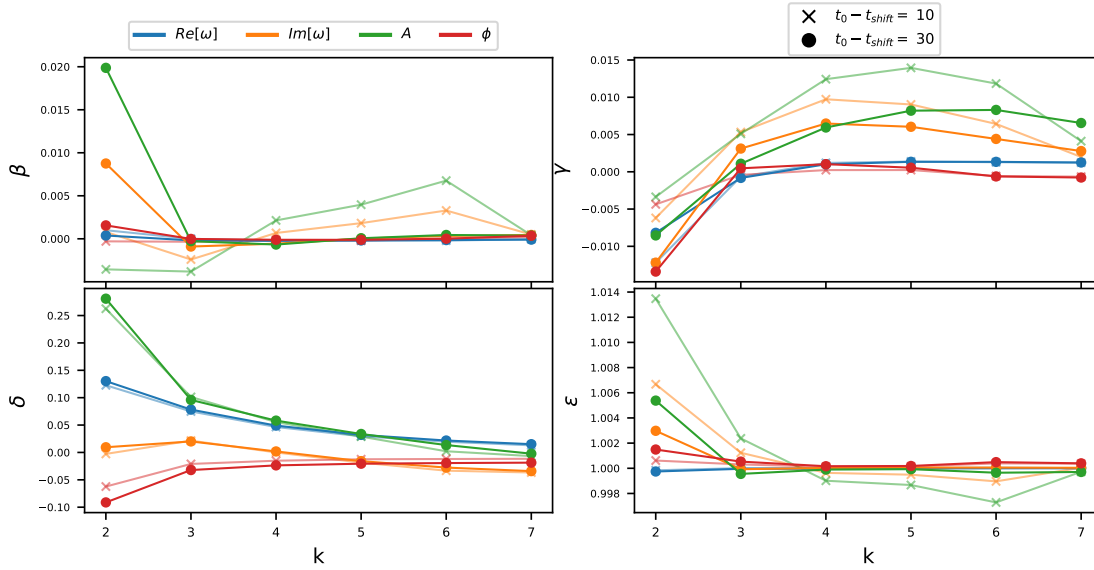


Figure 7.6: For each curve of Figure 7.5 we fit a cubic polynomial $f(\alpha^{(k)}) = \beta \cdot (\alpha^{(k)})^3 + \gamma \cdot (\alpha^{(k)})^2 + \delta \cdot (\alpha^{(k)}) + \epsilon$. The coefficients of these fit are shown in this Figure, showing that for the range of modification amplitude $\alpha^{(k)} \in [-1.5, 1.5]$, all the parameters admit quadratic correction with respect to the GR value, except for the real part which admits linear. That is because the coefficients of the cubic and quadratic terms are zero.

7.2 MULTIPLE MODIFICATIONS AT A TIME

As a second application we increase the complexity by adding to the Regge-Wheeler (RW) potential multiple inverse powers of r at the same time. We introduce a parameter $\epsilon \in [-0.60, 0.60]$ that controls and correlates all the modifications. As we have already seen in Chapter 4, the condition

$$\alpha^{(k)} \ll (k+1)(1+1/k)^k = \alpha_{\max}^{(k)}, \quad (7.2)$$

gives an estimation for the upper bound of the amplitudes. This upper bound is different for each k . In that sense, the parameter ϵ refers to the percentage of the maximum amplitude of each modification that is included in the potential, which now becomes

$$V(r) = V^{GR}(r) + \epsilon \frac{1}{r_H^2} \sum_{k=2}^7 \alpha_{\max}^{(k)} \left(\frac{r_H}{r}\right)^k. \quad (7.3)$$

We fit the generated linear ringdown waveforms with the model from equation (6.2) using $N = 1$ mode and excluding the tail. In Figure 7.7 we show in two different formats the results for the mismatches as a function of stating time of the fit and the parameter $\epsilon \in [-0.60, 0.60]$. In the left panel we show a colormap of mismatch in logarithmic scale, while in the right panel we present the evolution of the mismatch with $t_0 - t_{\text{peak}}$ and the colors refer to the value of ϵ .

Observe again the abrupt fall of the mismatch up to $t_0 - t_{\text{peak}} \sim 10M - 20M$ and then an oscillatory behavior with gradual rise. The oscillations and the rise, can be attributed due

to the lack of modeling of the power-law tail. As we see, negative ϵ modifications yield smaller mismatches in general.

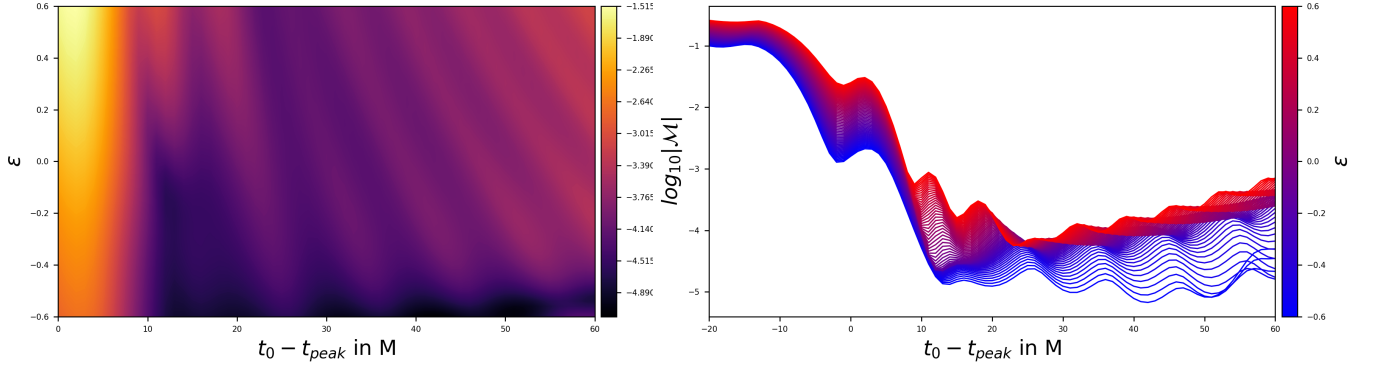


Figure 7.7: Results for the obtained mismatches shown in two different ways. **Left panel:** The horizontal axis shows the starting time of the fit $t_0 - t_{peak}$ and the vertical the parameter ϵ . The colormap depicts the value of each mismatch on logarithmic scale with orange being large and purple being small. **Right panel:** Mismatch as a function of the starting time of the fit. Negative values of ϵ are shown in blue and positive values in red.

Next, in Figure 7.8, we present the results for the four fitted parameters. All plots have the same structure, where the horizontal axis corresponds to $t_0 - t_{peak}$ and the vertical axis represents the value of ϵ . The colormap reflects the value of the extracted parameter. For the real and imaginary parts, we can compare with their GR counterparts. For that, we center the colormap so that white corresponds to the GR value, with the red and blue indicating values larger and smaller than the GR reference, respectively. For amplitude and phase, though, no GR reference value exists, therefore the white color has no significance. We also show some slices of the contours either for constant ϵ in Figure 7.9 or constant starting time $t_0 - t_{peak}$ in Figure 7.10. The horizontal lines on the top figure and the red lines on the bottom figure are the theoretical predictions from the PF. The horizontal and vertical lines from the previous Figure 7.8 correspond to the slices that we took.

In all Figures, the oscillations caused by the tails are evident. From all the parameters, the real part is the most stable one. Clearly, it is larger than the GR value for positive ϵ and smaller for negative. On the other hand, the imaginary part has richer structure regarding its oscillation and as we see there are circular regions inside of which the extracted value is smaller than GR and the amplitude and phase behave completely different.

From Figure 7.9 observe that the theoretical predictions for the frequency parameters deviate more as ϵ increases and that the imaginary part deviates less. The last point is evident also in Figure 7.10, where we see that for various starting times the imaginary part falls closer to the theoretical line and for a larger region than the real part.

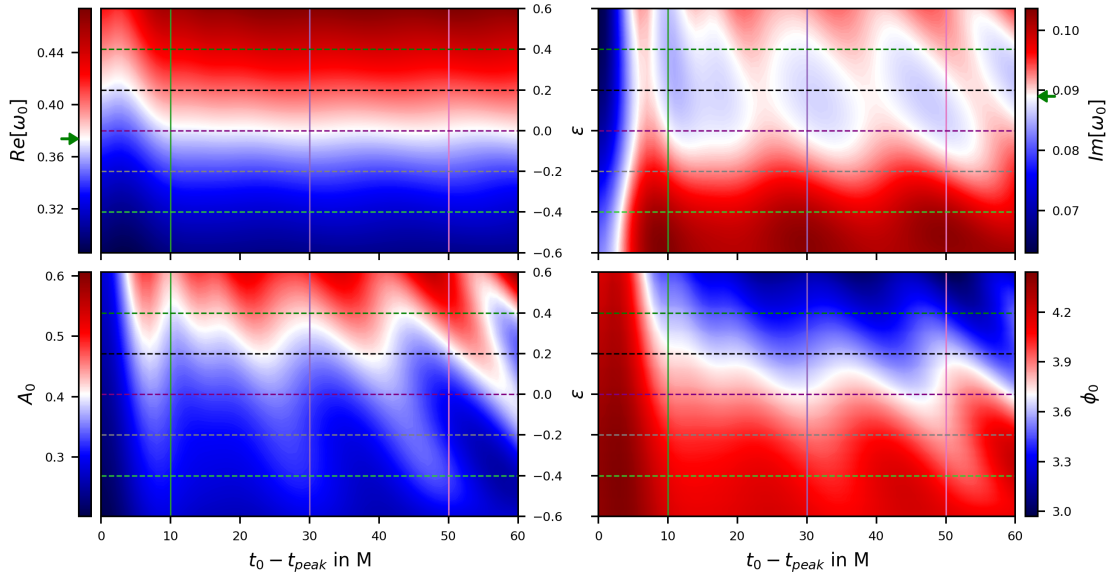


Figure 7.8: Results for the parameters that model the fundamental mode. In horizontal axes we show the starting time of the fit $t_0 - t_{peak}$ and in vertical the value of the parameters parameter ϵ . The colorbar stands for something different in each panel, **Top left:** Real part, **Top right:** imaginary part, **Bottom left:** amplitude and **Bottom right:** phase. For the top panel, the white color and the green arrows on the colormap, indicate the GR value. For the bottom panel, there is not theoretical GR value therefore the white color has no special significance.

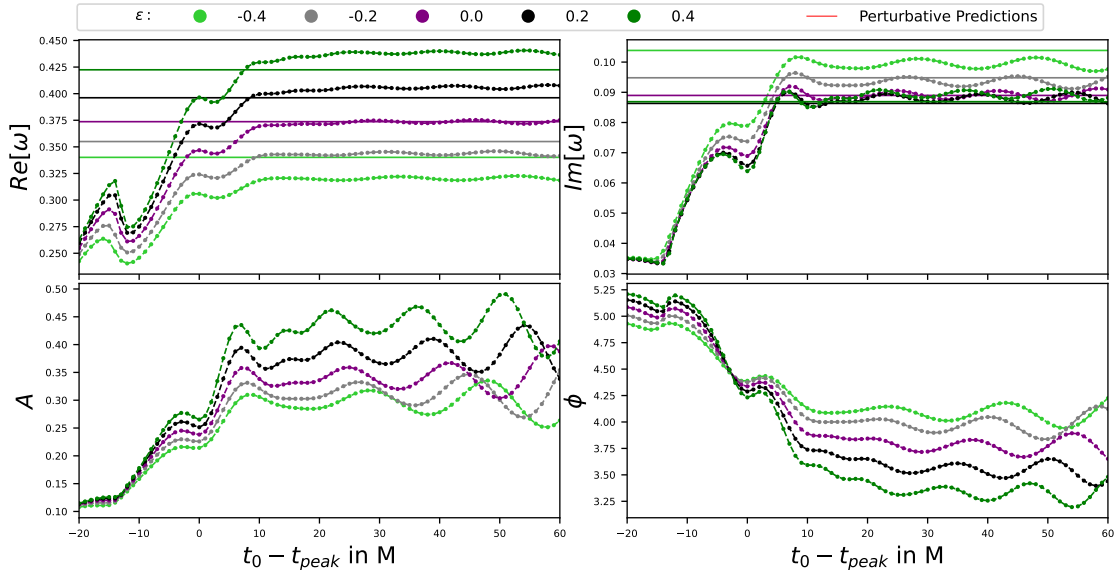


Figure 7.9: Results for the parameters that model the fundamental mode. In horizontal axes we show the starting time of the fit $t_0 - t_{peak}$ and in vertical the values of the parameters which is different for each panel. The horizontal solid lines correspond to the prediction from the PF

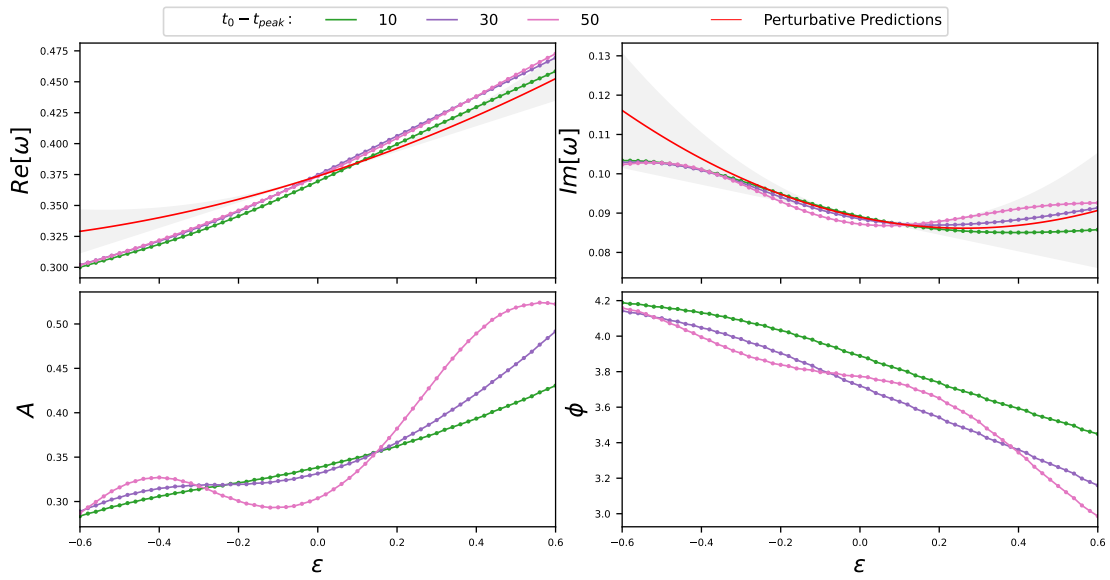


Figure 7.10: Results for the parameters that model the fundamental mode. In horizontal axes we show the parameter ϵ and in vertical the values of the parameters which is different for each panel. The red solid lines show the prediction from the PF, and the gray shaded area the error that comes from the quadratic correction on top of the linear.

FUTURE WORK

An extension of the above would be to incorporate into the models the exact form of the tail on the part with the simultaneous modifications. Additionally, we could also study the limits of the Parametrized Quasi-Normal Mode Framework by introducing multiple modifications at a time but this time to pick their amplitudes independently and randomly out of a prior range.

Chapter Summary

In this chapter, we discussed the following key points:

- Modification of the Regge-Wheeler potential with a single $1/r$ power at a time, from which we can infer
 - The extracted frequencies from the time-domain agree with the theoretically predicted values from the Parametrized Quasi-Normal Mode Framework.
 - The agreement is better for small amplitudes of the modification.
 - For all parameters modeling the fundamental mode, except for the imaginary part, the deviation from the GR value increases with larger amplitudes of the modification $\alpha^{(k)}$.
- Modification of the Regge-Wheeler potential with multiple $1/r$ powers at a time, from which we can infer the following if the late-time tail is not included in the models:
 - The extracted parameters show oscillatory behavior.
 - The imaginary part is closer to the theoretical predictions obtained from the Parametrized Quasi-Normal Mode Framework than the real part.

Appendix

ADDITIONAL MATERIAL FOR THE EXTRACTED PHASES AND ACCURACY OF THE

A.1 PÖSCHL TELLER POTENTIAL

In the next two Figures [A.1](#) and [A.2](#), we plot the extracted phase and the relative error of the extracted frequencies as a function of the starting time of the fit for the **PT** potential. We observe a jump in the phase for the first overtone of the TS models. This is due to the fact that the prior range that we provide to the fitting algorithm for the phase is $[0, 2\pi]$, so when exceeding it, continues to the other side of the range.

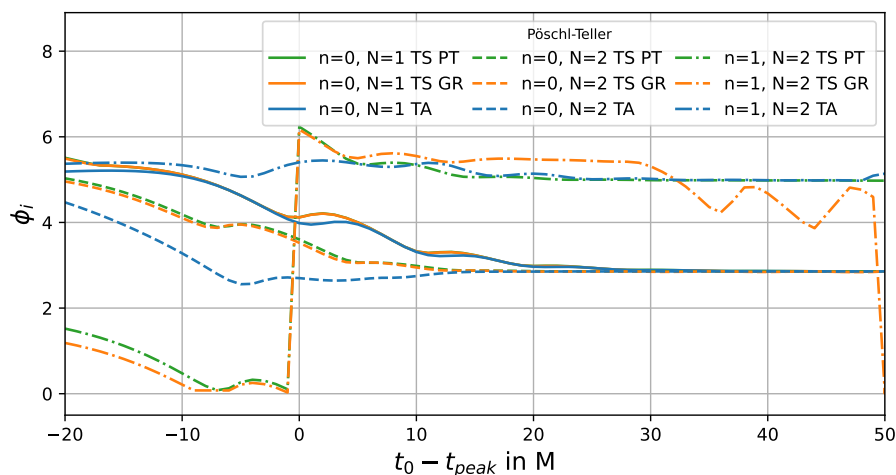


Figure A.1: Phases of the modes as a function of starting time of the fit for the **PT** waveform. *Solid lines* correspond to models containing $N = 1$ mode and the two types of *dashed lines* to models containing $N = 2$ modes.

The relative errors can also be explained. The TS GR models that assume the wrong frequency have limited accuracy (orange lines), whereas TA and TS PT further improve and reach their plateaus at later times. Also, the first overtone is obtained with smaller accuracy for all models.

A.2 REGGE-WHEELER POTENTIAL

In Figure [A.3](#) we show the extracted phases as functions of the starting time of the fit. Their behavior is similar to the other parameters. The phase of the fundamental mode (left

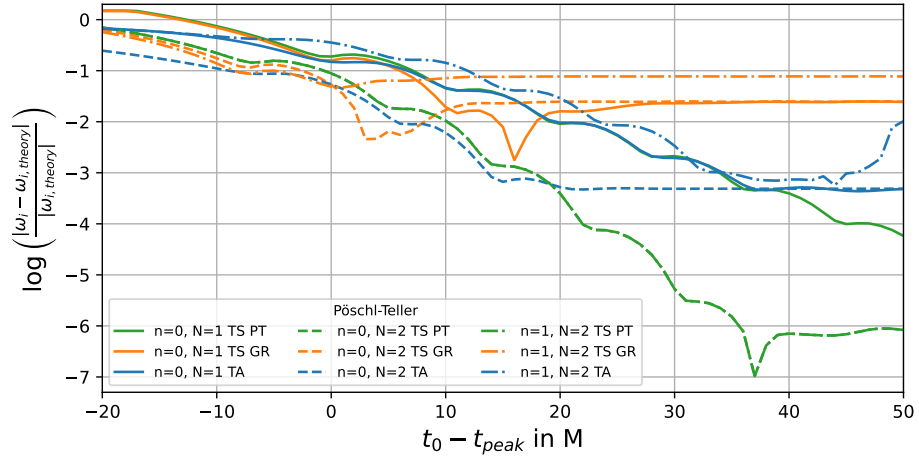


Figure A.2: Relative errors of the extracted frequencies as a function of starting time of the fit for the **PT** waveform. *Solid lines* correspond to models containing $N = 1$ mode and the two types of *dashed lines* to models containing $N = 2$ modes.

panel) oscillates for models the do not include the power-law tail and is stabilized for those who do. The phase of the first overtone could not be recovered from any model.

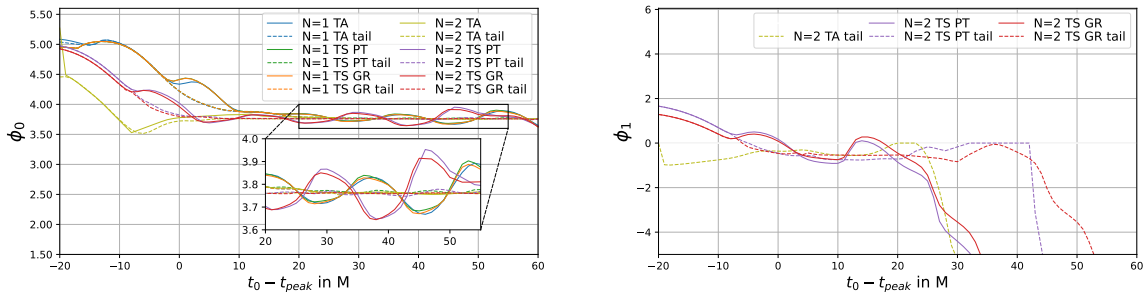


Figure A.3: Phases of the modes as a function of the starting time of the fit. **Left panel:** Fundamental mode results. **Right panel:** First overtone results.

B

ADDITIONAL MATERIAL FOR THE SINGLE K MODIFICATION

In this Appendix we present similar results with Section 7.1 but now we perform the fits only including the fundamental mode, without the tail. At first, in Figure B.1, we show the mismatches obtained for various powers k and amplitudes $\alpha^{(k)}$. The layout is the same as Figure 7.1. Observe the difference here, that the mismatch have the usual behavior of declining at first and then rise gradually for late times. This rise can be attributed to the non inclusion of tails in the model.

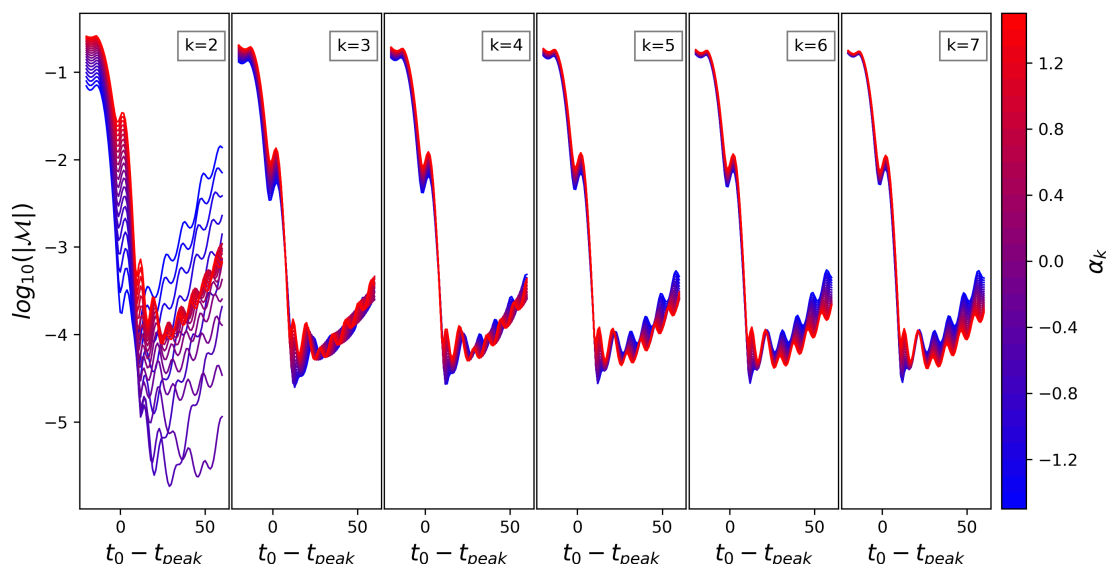


Figure B.1: Mismatches between fit results and the generated waveforms of the same initial data, as a function of the starting time. Each panel shows different power of k and the colorbar indicates the value of the amplitude varying from $\alpha^{(k)} = -1.5$ (blue) to $+1.5$ (red).

The fundamental modes for all the modifications were successfully recovered with non gradual rise of the amplitudes and phases but instead with oscillating. In Figures ?? we show the results for the complex frequency, for the real part in the left and for the imaginary in the right. The structure of both figures is the following: All horizontal axes show the starting time of the fit $t_0 - t_{peak}$ and all the vertical axes show the amplitude of the modification $\alpha^{(k)}$. Each panel refers to different power k . The colormap shows the values of the complex frequency. White is the GR value (meaning with $\alpha^{(k)} = 0$) which is also denoted in the colormap with a green arrow. Red color means that the extracted frequency is higher than the GR counterpart and blue that is lower.

Observe the oscillations of the extracted frequencies. By picking a certain value of $\alpha^{(k)}$, the extraction is not stable and especially for the imaginary part where we see that even for a specific amplitude it oscillates to greater and lower than the GR value.

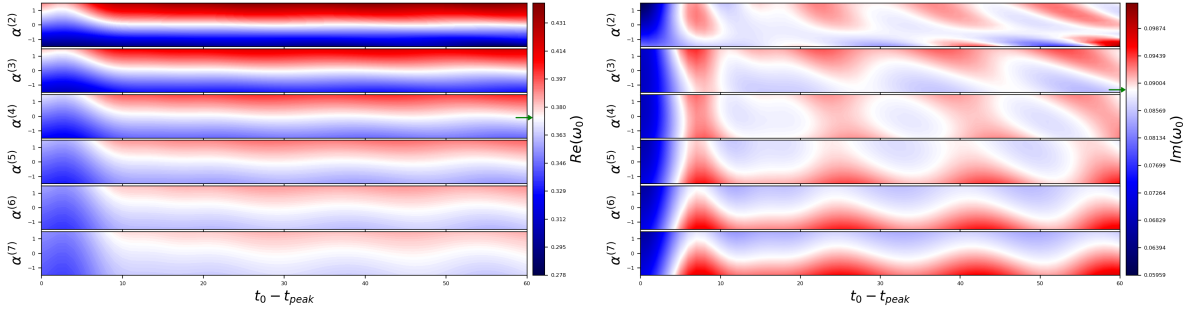


Figure B.2: **Left panel:** Real part of the frequency. **Right panel:** Imaginary part of the frequency. The layout is common for both panels. The horizontal axes correspond to the starting time of the fit $t_0 - t_{peak}$ and the vertical to the amplitude of the modification. The color shows the value of the extracted frequency with white being the GR value, red larger than that and blue smaller. The green arrow on the colormap also shows the GR value.

For direct comparison for results of Section 7.1 we provide Figure B.3, which has the same layout as Figure 7.2. Observe that for small k , the extracted frequencies deviate a lot from the perturbative predictions.

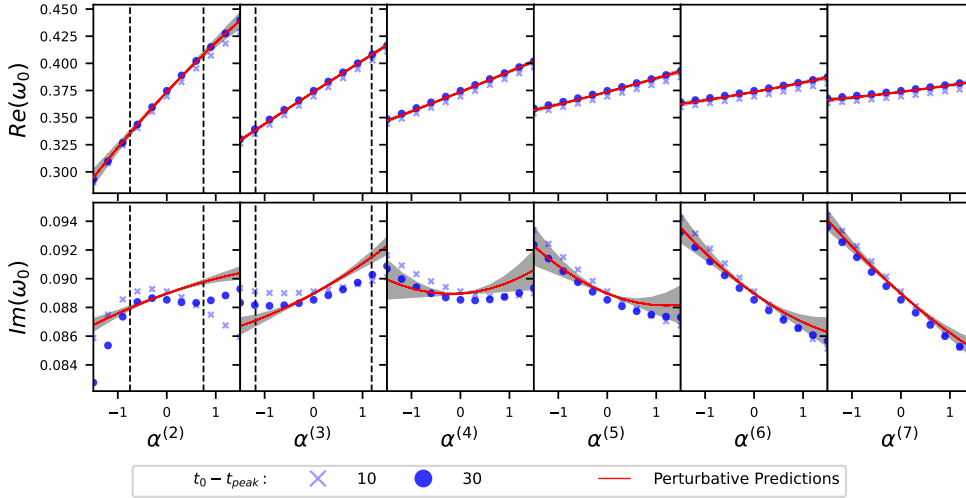


Figure B.3: Results for the extracted frequencies as a function of the amplitude $\alpha^{(k)}$, for two starting times indicated by two different blue markers. **Top panel:** real part. **Bottom panel:** imaginary part. Each *vertical panel* refers to a different power $k \in [2, 7]$. *Red lines:* quadratic perturbative predictions *Gray errorband:* systematic error coming from the quadratic correction on top of the linear. *Vertical dashed lines* refer to the upper bounds of the amplitudes, under which the framework should be accurate. These lines are not shown for the last four k 's since they are outside of the range of amplitudes.

Extensive Greek Abstract

ΓΕΝΙΚΉ ΣΧΕΤΙΚΌΤΗΤΑ, ΜΕΛΑΝΉΣ ΟΠΉΣ ΚΑΙ ΒΑΡΥΤΙΚΆ ΚΎΤΜΑΤΑ

Αυτό το Κεφάλαιο παρέχει μια σύντομη εισαγωγή σε ορισμένες προαπαιτούμενες έννοιες για τα επόμενα μέρη της εργασίας. Συγκεκριμένα, συζητούμε τη σύνδεση της παλαιάς Νευτώνειας θεωρίας με τη Γενική Σχετικότητα, προχωρούμε στην εξαγωγή της σφαιρικά συμμετρικής λύσης των εξισώσεων του Einstein και αναλύουμε τις ιδιαιτερότητές της. Τέλος, συζητούμε για τα βαρυτικά κύματα και ειδικότερα για μια **multi-messenger** ανίχνευση μιας Συγχώνευση Δυαδικού Συστήματος Άστρων Νετρονίων, τα διάφορα στάδια συγχώνευσης δυαδικού συστήματος Μελανής Οπής και επικεντρωνόμαστε στο τελικό στάδιο, το **ringdown**.

ΠΑΛΑΙΑ ΚΑΙ ΝΕΑ ΘΕΩΡΙΑ

Η Γενική Σχετικότητα είναι πιά επιτυχημένη θεωρία της βαρύτητας που διαθέτουμε. Οι βάσεις της διατυπώθηκαν από τον Άλμπερτ Αϊνστάιν το 1915 στα πρακτικά της Ακαδημίας Επιστημών της Πρωσίας [1]. Βήματα προς την πειραματική επιβεβαίωση της Γενικής Σχετικότητας έγιναν πολύ νωρίς, με την πρώτη σωστή ποσοτική εξήγηση και πρόβλεψη της μετάπτωσης του περιηλίου της τροχιάς του Ερμή το 1916, ένα φαινόμενο που δεν μπορούσε να εξηγήσει η Νευτώνεια θεωρία. Αν και αυτή η επιτυχία ήταν καθοριστική για την επικύρωση της Γενικής Σχετικότητας, όπως ήταν αναμενόμενο, δεν ήταν αρκετή για να διαλύσει όλη τη δυσπιστία της εποχής [2].

Η θεωρία έκανε κάτι περισσότερο από απλή βελτίωση του προδρόμου της. Αντιπροσώπευσε μια αλλαγή παραδείγματος στην κατανόηση της βαρύτητας. Αντί να αντιμετωπίζει τη βαρύτητα ως μια δύναμη, όπως έκανε η παλαιά θεωρία, η θεωρία του Einstein περιέγραψε τη βαρύτητα ως καμπυλότητα του χωροχρόνου. Αυτή η νέα οπτική άλλαξε ριζικά την προσέγγισή μας στα βαρυτικά φαινόμενα και οδήγησε τόσο σε ποιοτικές όσο και σε ποσοτικές βελτιώσεις.

Για να τονιστεί το μέγεθος αυτής της αλλαγής, ας σκεφτούμε μια ιστορική αναλογία: τη μετάβαση από το γεωκεντρικό σύστημα του Πτολεμαίου στο ηλιοκεντρικό σύστημα του Κοπέρνικου. Υποβαθμίζοντας τη Γη από το κέντρο του σύμπαντος σε έναν περιφερειακό πλανήτη, αυτή η επανάσταση είχε βαθιές επιπτώσεις, επηρεάζοντας όχι μόνο την επιστήμη αλλά και τη φιλοσοφία, τη θρησκεία, την πολιτική σκέψη και τις τέχνες [2].

Στην περίπτωση της Γενικής Σχετικότητας, η αλλαγή ήταν από τη Νευτώνεια αντίληψη της βαρύτητας ως μιας άμεσης και στιγμιαίας δύναμης, σε μια θεώρηση της βαρύτητας ως καμπυλότητας του χωροχρόνου, όπου τα αντικείμενα ακολουθούν διαδρομές που καθορίζονται από αυτή την καμπυλότητα. Στο νέο πλαίσιο, όταν δύο σώματα αλληλεπιδρούν, το ένα καμπυλώνει τον χωροχρόνο, ενώ το άλλο καθοδηγείται από αυτή την καμπυλότητα και αντίστροφα.

Η παλαιά θεωρία περιγράφεται από τον Νόμο της Παγκόσμιας Έλξης του Νεύτωνα

$$\mathbf{F} = -\frac{Gm_1m_2}{r^2}\hat{e}_{(r)}, \quad (\text{B.1})$$

ο οποίος προσδιορίζει μια ακτινική δύναμη που μεταβάλλεται αντιστρόφως ανάλογα με το τετράγωνο της απόστασης μεταξύ δύο σωματιδίων μάζας m_1 και m_2 . Λόγω της συντηρητικής φύσης αυτής της δύναμης, μπορεί να εκφραστεί ως κλίση ενός βαρυτικού δυναμικού Φ που υπακούει στην εξίσωση Poisson

$$\nabla^2\Phi = -4\pi G\rho, \quad (\text{B.2})$$

όπου ρ είναι η πυκνότητα μάζας. Αυτές οι εξισώσεις δηλώνουν ότι η επίδραση της Νευτώνειας βαρύτητας είναι στιγμιαία και καθολική, δηλαδή, όλοι οι πιθανοί παρατηρητές αντιλαμβάνονται τον χώρο και τον χρόνο με τον ίδιο τρόπο. Συνεπώς, υπάρχει απόλυτος χώρος και απόλυτος χρόνος.

Οι εξισώσεις κίνησης της νέας θεωρίας είναι:

$$R_{\mu\nu} - \frac{1}{2}Rg_{\mu\nu} = \frac{8\pi G}{c^4}T_{\mu\nu}. \quad (\text{B.3})$$

Στην αριστερή πλευρά έχουμε τον ταυστή καμπυλότητας του Ricci $R_{\mu\nu}$, τον βαθμωτό ταυστή του Ricci $R = g^{\mu\nu}R_{\mu\nu}$ και τον μετρικό ταυστή $g_{\mu\nu}$. Ο ταυστής Ricci και ο βαθμωτός ταυστής εξαρτώνται από τον μετρικό ταυστή, και η μετρική δείχνει πώς παραμορφώνεται ο χώρος λόγω της παρουσίας μάζας. Στη δεξιά πλευρά έχουμε τον ταυστή ενεργειακής-ορμής $T_{\mu\nu}$, που περιγράφει την κατανομή και τη ροή ενέργειας και ορμής στον χωροχρόνο. Έτσι, τα γεωμετρικά αντικείμενα που περιγράφουν την καμπυλότητα συνδέονται με την περιγραφή της ύλης. Στόχος είναι να λύσουμε αυτές τις εξισώσεις ως προς τον μετρικό ταυστή και, συνεπώς, να ορίσουμε τον χωροχρόνο του συστήματος υπό εξέταση.

Μια αναγκαία απαίτηση για τη Γενική Σχετικότητα είναι ότι πρέπει να αναπαράγει τις εξισώσεις της Νευτώνειας βαρύτητας στο καθεστώς ασθενούς πεδίου και μικρών ταχυτήτων. Η τροχιά ενός ελεύθερου σωματιδίου που κινείται σε καμπυλωμένο χωροχρόνο περιγράφεται από την γεωδαιτική εξίσωση

$$\frac{d^2x^\mu}{d\tau^2} + \Gamma^\mu_{\nu\sigma} \frac{dx^\nu}{d\tau} \frac{dx^\sigma}{d\tau} = 0, \quad (\text{B.4})$$

όπου τ είναι ο ιδιοχρόνος και $\Gamma^\mu_{\nu\sigma}$ είναι οι σύμβολα του Christoffel που χρησιμοποιούνται για γενίκευση των παραγώγων σε καμπυλωμένο χωροχρόνο και σχετίζονται άμεσα με τη μετρική

$$\Gamma^\mu_{\nu\sigma} = \frac{1}{2}g^{\mu\alpha} (\partial_\nu g_{\alpha\sigma} + \partial_\sigma g_{\alpha\nu} - \partial_\alpha g_{\nu\sigma}). \quad (\text{B.5})$$

Σε ασθενές πεδίο και μικρές ταχύτητες γεωδαιτική εξίσωση γίνεται

$$\frac{d^2\vec{x}}{d\tau^2} = -\frac{1}{2}c^2\nabla h_{00}, \quad (\text{B.6})$$

όπου h είναι η μικρή διόρθωση στην επίπεδη μετρική $g_{\mu\nu} = \eta_{\mu\nu} + h_{\mu\nu}$. Συνεπώς, για να υπάρχει συμφωνία με την παλαιά θεωρία, πρέπει να ισχύει $g_{00} = 1 - 2\Phi/c^2$.

Τονίζουμε ότι, ενώ η Νευτώνεια θεωρία συμφωνεί με τη Γενική Σχετικότητα! σε αυτό το συγκεκριμένο καθεστώς, αυτό δεν σημαίνει ότι η Νευτώνεια θεωρία είναι απλώς υποσύνολο της Γενικής Σχετικότητας!. Το γεγονός ότι οι μαθηματικές εξισώσεις είναι ίδιες δεν σημαίνει ότι έχουν

και την ίδια σημασία. Η μία προέρχεται από μια θεωρία που ενσωματώνει τη στιγμιαία δράση από απόσταση και την καθολικότητα του χώρου και του χρόνου, ενώ η άλλη βασίζεται στην αρχή της ισοδυναμίας. Η αρχή ισοδυναμίας του Einstein αποτελείται από τρία μέρη. Πρώτον, αποδέχεται την ισότητα της βαρυτικής και της αδρανειακής μάζας, η οποία περιλαμβανόταν ήδη στη Νευτώνεια θεωρία. Τα άλλα δύο σχετίζονται με τα μη βαρυτικά πειράματα, αναφέροντας ότι το αποτέλεσμα τους θα πρέπει να είναι ανεξάρτητο από την ταχύτητα του ελεύθερα κινούμενου συστήματος στο οποίο εκτελούνται και επίσης ανεξάρτητο από τη χρονική και χωρική του τοποθεσία στο σύμπαν [3, 4].

ΒΑΡΥΤΙΚΑ ΚΥΜΑΤΑ

ΗΛΕΚΤΡΟΜΑΓΝΗΤΙΚΑ & ΒΑΡΥΤΙΚΑ ΚΥΜΑΤΑ

Τα αστροφυσικά αντικείμενα αποκαλύπτουν τις ιδιότητές τους με διάφορους τρόπους, με την ηλεκτρομαγνητική και τη βαρυτική ακτινοβολία να είναι δύο από τους σημαντικότερους [14]. Αυτοί οι δύο τύποι ακτινοβολίας είναι θεμελιωδώς διαφορετικοί, φωτίζοντας ξεχωριστές και συμπληρωματικές όψεις των αντικειμένων που μελετώνται.

Η ηλεκτρομαγνητική ακτινοβολία εκπέμπεται από φορτισμένα στοιχειώδη σωματίδια όπως τα ηλεκτρόνια που επιταχύνονται. Καθώς τα αστροφυσικά αντικείμενα είναι γενικά ηλεκτρικά ουδέτερα, αυτή η ακτινοβολία συνήθως προέρχεται από μικρές, τοπικές περιοχές αντικειμένου, γεγονός που οδηγεί σε μικρά μήκη κύματος. Τα ηλεκτρομαγνητικά κύματα παρέχουν λεπτομερείς πληροφορίες για αυτές τις τοπικές περιοχές. Επίσης, αν καταφέρουν να φτάσουν στη Γη χωρίς να απορροφηθούν ή να σχεδαστούν από την ύλη που παρεμβάλλεται, είναι σχετικά εύκολη η ανίχνευσή τους λόγω της ισχυρής αλληλεπίδρασής τους με τα ηλεκτρικά φορτία [14].

Αντίθετα, τα βαρυτικά κύματα εκπέμπονται από το σύστημα συνολικά, με αποτέλεσμα να έχουν μεγαλύτερα μήκη κύματος. Μεταφέρουν πληροφορίες για τη συνολική δυναμική και τη δομή του συστήματος. Η ασθενής τους αλληλεπίδραση με την ύλη καθιστά την ανίχνευσή τους εξαιρετικά δύσκολη. Ωστόσο, όταν ανιχνευτούν, το σήμα τους διατηρεί σχεδόν την ίδια μορφή με εκείνη που εκπέμφθηκε από την πηγή, καθώς η αλληλεπίδρασή τους με άλλα αντικείμενα είναι ελάχιστη [14].

Ένα παράδειγμα συνεργασίας των δύο τύπων ακτινοβολίας είναι η ανίχνευση ενός δυαδικού συστήματος αστέρων νετρονίων, τον Αύγουστο του 2017. Οι ανιχνευτές LIGO και VIRGO έλαβαν πρώτοι το σήμα βαρυτικών κυμάτων, GW170817, και λίγα δευτερόλεπτα αργότερα το διαστημικό τηλεσκόπιο ακτίνων γάμμα Fermi, κατέγραψε την έκρηξη ακτίνων γ, GRB 170817A [15, 16]. Και τα δύο σήματα εντοπίστηκαν από την ίδια πηγή λόγω της παρόμοιας τοποθέτησής τους στον ουρανό. Μετά από περίπου 11 ώρες, η συνεργασία "One-Meter, Two-Hemisphere" κατέγραψε οπτική παρατήρηση [17]. Τα οπτικά δεδομένα εντόπισαν την πηγή στον γαλαξία NGC 4993, που βρίσκεται 40 Mpc μακριά από τη Γη, απόσταση που ήταν συμβατή με την εκτίμηση της απόστασης από τα βαρυτικά κύματα.

Η Εικόνα 1.2, παρουσιάζει την ανίχνευση του GW170817 και τα ηλεκτρομαγνητικά αντίστοιχα σήματα. Στην αριστερή εικόνα, οι χρονικές-συχνότητες από το LIGO και το Kagra δείχνουν πώς οι κυρίαρχες συχνότητες (ενδεικτικά με κίτρινο) των βαρυτικών κυμάτων αυξάνονται με τον

χρόνο καθώς τα δυαδικά άστρα νετρονίων σπειροειδώς πλησιάζουν το ένα το άλλο. Στο μεσαίο τμήμα εμφανίζεται μια τυπική ανίχνευση έκρηξης ακτίνων γ στα 229 eV, ενώ στο δεξί τμήμα παρουσιάζεται η οπτική παρατήρηση, συγκρίνοντας μια εικόνα που λήφθηκε τέσσερις μήνες πριν την ανίχνευση των BK, με μια άλλη που λήφθηκε 11 ώρες μετά.

Ενώ ο συνδυασμός παρατηρήσεων ηλεκτρομαγνητικών και βαρυτικών κυμάτων, μέρος της λεγόμενης **multi-messenger** αστροφυσικής, δεν εκπέμπουν όλα τα αστροφυσικά συστήματα ηλεκτρομαγνητικά σήματα. Ένα τέτοιο σύστημα είναι η Συγχώνευση Δυαδικών Μαύρων Τρυπών, που δεν παράγει ηλεκτρομαγνητική ακτινοβολία και το τελικό της στάδιο είναι το θέμα αυτής της διπλωματικής. Ας επικεντρωθούμε στα βαρυτικά κύματα που παράγονται από αυτά τα συστήματα.

ΣΤΑΔΙΑ ΣΥΓΧΩΝΕΥΗΣ

Η εξέλιξη των δυαδικών συστημάτων, αποτελείται από τρία κύρια στάδια, τα οποία έχουν σημαντικές διαφορές στις διορθώσεις που πρέπει να συμπεριληφθούν στην κυματομορφή για να περιγραφεί η διαδικασία με ακρίβεια. Συγκεκριμένα, τα συστήματα που περιλαμβάνουν νετρονικούς αστέρες είναι πάντα πιο περίπλοκα να μοντελοποιηθούν, καθώς πρέπει να ληφθούν υπόψη επιπλέον φαινόμενα και ιδιότητες, όπως η εσωτερική δομή του αστέρα νετρονίων και οι παλιρροιακές επιδράσεις. Επιπλέον, η πολυπλοκότητα αυξάνεται αν τα αντικείμενα περιστρέφονται και αυξάνεται ακόμη περισσότερο αν οι ιδιοπεριστροφές δεν είναι ευθυγραμμισμένες.

Θα εστιάσουμε στη συγχώνευση διπλών μαύρων οπών, καθώς όλα τα άλλα συστήματα είναι πέρα από το πεδίο της παρούσας διπλωματικής. Αποτελείται από τα τρία στάδια που παρουσιάζονται στην Εικόνα 1.3, και κάθε στάδιο ή διαφορετικές τιμές μαζών και αποστάσεων αντιμετωπίζεται με διαφορετικές τεχνικές και μεθόδους, όπως δείχνεται στην Εικόνα 1.4. Οι τρεις φάσεις της συγχώνευσης είναι οι εξής:

- a) *Inspiral*: Αυτή είναι η πιο πρόωμη φάση της εξέλιξης, όπου τα δύο συμπαγή αντικείμενα έχουν μικρές ταχύτητες και μεγάλη απόσταση, η οποία μειώνεται σταδιακά λόγω της απώλειας ενέργειας προς τα βαρυτικά κύματα. Όπως βλέπουμε στο μπλε πλαίσιο της Εικόνας 1.4, η αναλυτική προσέγγιση **Post-Newtonian** χρησιμοποιείται ως εργαλείο για να μοντελοποιήσει το κύμα σε μεγάλες αποστάσεις. Από αυτή τη μέθοδο, οι εξισώσεις πεδίου του **Einstein** αναπτύσσονται γύρω από το Νευτώνειο όριο σε δυνάμεις της μικρής παραμέτρου $\epsilon \sim u/c$. Κάθε δύναμη n ενσωματώνει ένα νέο φαινόμενο στο μοντέλο της κυματομορφής, για παράδειγμα, $n = 2$ περιλαμβάνει την μετάπτωση της τροχιάς, $n = 3$ περιλαμβάνει την σύζευξη **spin**-τροχιάς, $n = 4$ την σύζευξη **spin-spin** και η εκπομπή βαρυτικών κυμάτων εμφανίζεται για $n \geq 5$ [22–24].
- b) *Merger*: Αυτή είναι η ενδιάμεση φάση της εξέλιξης. Ξεκινά όταν η απόσταση διαχωρισμού είναι μικρότερη από την Ελάχιστη Σταθερή Κυκλική Τροχιά και τελειώνει όταν σχηματίζεται το τελικό υποκείμενο. Οι μη γραμμικότητες κυριαρχούν σε αυτή τη φάση, και τα εργαλεία που χρησιμοποιούνται για να την αντιμετωπίσουν είναι πολλά, όπως φαίνεται στο Σχήμα 1.4. Η Αριθμητική Σχετικότητα, μια καθαρά αριθμητική προσέγγιση των εξισώσεων πεδίου του **Einstein** που λειτουργεί καλύτερα για μικρούς και ενδιάμεσους λόγους μάζας,

και η θεωρία διαταραχών της βαρυτικής ιδιο-δύναμης, η οποία χρησιμοποιείται σε περιοχές μεγάλου λόγου μάζας και λαμβάνει υπόψη την επίδραση ενός μικρού αντικειμένου στην κίνησή του ενώ κινείται στο πεδίο ενός αντικειμένου μεγάλης μάζας[25].

- c) Ringdown: Αυτή είναι η τελευταία φάση της εξέλιξης όπου απομένει μια μοναδική μελανή οπή. Διεγερμένο από την προηγούμενη φάση, το τελικό αντικείμενο καταλήγει εκθετικά σε ισορροπία εκπέμποντας βαρυτικά κύματα κατά τη διαδικασία. Το παραγόμενο σήμα περιγράφεται επαρκώς από τις μιγαδικές συχνότητες που ονομάζονται Ψευδο-Κανονικοί Τρόποι Ταλάντωσης (Quasi-Normal Modes).

RINGDOWN

Η **ringdown** φάση μιας περιστρεφόμενης μελανής οπής μπορεί να περιγραφεί επαρκώς από ένα άπειρο άθροισμα διακριτών μιγαδικών συχνοτήτων:

$$h(t) \simeq \sum_{\ell, m, n} A_{\ell mn} e^{-i(M\omega_{n\ell m}t + \phi_{n\ell m})},$$

όπου M είναι η μάζα της μελανής οπής, $n \geq 0$ καθορίζει την αρμονική, και $|m| \leq \ell$ είναι ο αζιμουθιακός αριθμός, περιγράφοντας πλήρως κάθε συχνότητα. Αυτή η ομάδα συχνοτήτων $\omega_{\ell mn}$ ονομάζεται Ψευδο-Κανονικό Φάσμα Συχνοτήτων.

Το φάσμα φέρει πληροφορίες για τον εκπομπέα, και στην περίπτωση μας, αν ισχύει το θεώρημα **no-hair**, περιγράφει πλήρως τις ιδιότητες μίας αστροφυσικής μελανής οπής, οι οποίες είναι η μάζα της, M , και η περιστροφή της, a [28].

Η σημασία της φάσης **ringdown** έγκειται στην ικανότητά της να προσφέρει πολύτιμες ευκαιρίες για τη δοκιμή της γενικής σχετικότητας [28, 29]. Ωστόσο, η μέτρηση μόνο της θεμελιώδους συχνότητας ($n = 0$) δεν είναι αρκετή για να προσδιορίσει πλήρως τις ιδιότητες του αντικειμένου, όπως η περιστροφή του, a , και η μάζα του, M . Αυτό συμβαίνει επειδή διαφορετικοί τύποι αντικειμένων μπορεί να έχουν ρυθμισμένες παραμέτρους που συμπτωματικά αποδίδουν την ίδια θεμελιώδη συχνότητα. Από την άλλη πλευρά, αν μετρήσουμε δύο ή περισσότερες συχνότητες από το ίδιο αντικείμενο, μπορούμε να κάνουμε μια έλεγχο συνέπειας για τη γενική σχετικότητα [28]. Συγκρίνοντας αυτές τις πολλές συχνότητες με τις θεωρητικές προβλέψεις, μπορούμε να επαληθεύσουμε αν αντιστοιχούν στο ίδιο ζευγάρι τιμών a και M , όπως προβλέπεται από τη γενική σχετικότητα. Αν υπάρχει ασυνέπεια, η πηγή της θα μπορούσε να είναι είτε ότι η γενική σχετικότητα δεν είναι η σωστή περιγραφή της βαρύτητας είτε ότι το αντικείμενο δεν είναι απομονωμένο και υπάρχει συγκεντρωμένη μάζα γύρω του που αλλοιώνει το φάσμα.

ΕΦΑΡΜΟΓΕΣ ΚΑΙ ΑΠΟΤΕΛΕΣΜΑΤΑ I

Σε αυτό το κεφάλαιο, παρουσιάζουμε το πρώτο σύνολο αποτελεσμάτων, εστιάζοντας σε περιπτώσεις που σχετίζονται με τη γενική σχετικότητα. Μία σύντομη εξήγηση της διαδικασίας είναι η εξής: δημιουργούμε κυματομορφές **ringdown** λύνοντας αριθμητικά τις εξισώσεις γραμμικών διαταραχών με δυναμικά που σχετίζονται με τη γενική σχετικότητα. Στη συνέχεια, χρησιμοποιούμε διαφορετικά μοντέλα για να προσαρμόσουμε αυτά τα κύματα και να εξάγουμε τις παραμέτρους τους, ρυθμίζοντας συστηματικά το τμήμα του κύματος που περιλαμβάνεται στις προσαρμογές (το παράθυρο προσαρμογής) για να αξιολογήσουμε πώς επηρεάζει την εξαγωγή των παραμέτρων.

Πιο συγκεκριμένα, τα δυναμικά που χρησιμοποιούμε είναι το **Pöschl-Teller (PT)**, προσαρμοσμένο στο δυναμικό **Regge-Wheeler (RW)**, καθώς και η ίδια η δυναμική **RW**. Τα μοντέλα που χρησιμοποιούνται περιλαμβάνουν διαφορετικό αριθμό συχνοτήτων, με κάποια να περιλαμβάνουν επίσης την ουρά. Τα αποτελέσματα εδώ αναπαράγουν εν μέρει αυτά της αναφοράς [39], με μια επέκταση για να ενσωματώσουν μοντέλα που περιλαμβάνουν ουρές.

ΜΕΘΟΔΟΙ

Μία κοινή μέθοδος για τη μελέτη εξισώσεων κύματος της μορφής (3.11) με δυναμικό V , στο χρονικό πεδίο, περιλαμβάνει αρχικά τη λύση τους αριθμητικά και στη συνέχεια την ανάλυση των αποτελεσμάτων.

Χρησιμοποιούμε το σχήμα **Leapfrog**, το οποίο είναι ένα σχήμα πεπερασμένων διαφορών, κεντρικό στο χρόνο και τον χώρο, για ένα πλέγμα με αναλύσεις $\Delta t = 0.01$ και $\Delta r^* = 0.02$. Τα επιλεγμένα αρχικά δεδομένα είναι

$$\Psi(0, r) = Ae^{-\frac{(r-\mu)^2}{2\sigma^2}}, \quad (\text{B.7a})$$

$$\partial_t \Psi(0, r) = \partial \Psi(0, r^*), \quad (\text{B.7b})$$

για $A \sim \max\{V\}$, $\mu = 30M$ και $\sigma = 1M$. Η δεύτερη συνθήκη αναγκάζει την Γκαουσιανή να γίνει εισερχόμενη, κι έτσι να κινείται μόνο προς το δυναμικό.

Οι συνθήκες οριακής τιμής (ψBC) επιβάλλονται ως εξερχόμενες. Ωστόσο, καθώς οι εξερχόμενες συνθήκες οριακής τιμής υλοποιούνται αριθμητικά, η εφαρμογή τους είναι ελλιπής, εισάγοντας αριθμητικά σφάλματα. Για να μετριάσουμε την πιθανή μόλυνση του σήματος λόγω ανακλάσεων από αυτές τις ελλειπείς οριακές συνθήκες τοποθετούμε τα όρια του πεδίου αρκετά μακριά από την περιοχή ενδιαφέροντος.

Η προκύπτουσα αριθμητική λύση εξαρτάται από το χρόνο και το χώρο. Για να εξάγουμε το σήμα στο χρονικό πεδίο, τοποθετούμε έναν παρατηρητή στη σταθερή θέση $R = 100M$ και μελετάμε το καταγραφόμενο σήμα. Αυτή η τοποθεσία έχει επιλεγεί αρκετά μακριά από τον δακ-

τύλιο φωτός, διασφαλίζοντας ότι το καταγραφόμενο κύμα έχει σταματήσει να αλληλεπιδρά με το δυναμικό της μελανής οπής και είναι σχεδόν στην τελική του μορφή. Αν και η ιδανική θέση θα ήταν στο χωρικό άπειρο, αυτό δεν είναι εφικτό λόγω της αυξανόμενης αριθμητικής δαπάνης.

Γενικά, το καταγραφόμενο σήμα μπορεί να χωριστεί σε τρία μέρη: το κεντρικό μέρος, που περιγράφεται επαρκώς από τους QNM, το αρχικό μεταβατικό στάδιο όπου οι συχνότητες δεν έχουν αναπτυχθεί πλήρως και την ουρά του νόμου δύναμης σε μεγάλους χρόνους. Οι δύο τελευταίες συνεισφορές επηρεάζουν την εξαγωγή των παραμέτρων. Μία πρώτη και απλή ένδειξη γι' αυτό φαίνεται στο Σχήμα 6.1, όπου η μπλε γραμμή είναι το εξαγόμενο σήμα και οι άλλες αναφέρονται σε διάφορα μοντέλα προσαρμογής που περιλαμβάνουν μία ταλάντωση με απόσβεση (κίτρινη γραμμή), την ουρά νόμου δύναμης (κόκκινη γραμμή) ή και τα δύο (πράσινη γραμμή). Παρατηρήστε ότι όταν συμπεριλαμβάνεται η ουρά νόμου δύναμης, το αποτέλεσμα της προσαρμογής σχεδόν συμπίπτει με το καταγραφόμενο σήμα, ειδικά στους μεγάλους χρόνους. Ας προσπαθήσουμε να ποσοτικοποιήσουμε αυτό καλύτερα προσδιορίζοντας ακριβώς τη διαδικασία προσαρμογής και τα μοντέλα προσαρμογής.

TA MONTEΛA

Ο στόχος αυτού του κεφαλαίου είναι να μελετήσει πώς το τμήμα του κύματος που περιλαμβάνεται στην προσαρμογή επηρεάζει την εξαγωγή παραμέτρων. Για τον λόγο αυτό, χρησιμοποιούμε και συγκρίνουμε διάφορους τύπους αναλυτικών μοντέλων για να εξάγουμε τα κύρια χαρακτηριστικά του παραγόμενου γραμμικού κύματος. Αυτά τα μοντέλα είναι είτε αγνωστικά μοντέλα (Theory Agnostic (TA)) είτε εξειδικευμένα μοντέλα (Theory Specific (TS)) και μπορεί επίσης να περιλαμβάνουν την ουρά νόμου δύναμης του Price [52].

Τα μοντέλα TA δεν κάνουν υποθέσεις για τις συχνότητες QNM που περιλαμβάνονται στο κύμα και κάθε τρόπος, n , απαιτεί τέσσερις ελεύθερες παραμέτρους για να μοντελοποιηθεί. Αντίθετα, τα μοντέλα TS υποθέτουν συγκεκριμένες τιμές για τις συχνότητες QNM που περιλαμβάνονται στο κύμα. Οι λεπτομέρειες κάθε μοντέλου περιγράφονται παρακάτω.

- (i.) Ψ_N^{TA} : Αυτό είναι ένα μοντέλο TA, το οποίο δεν κάνει υποθέσεις για τις συχνότητες QNM και περιλαμβάνει N τρόπους:

$$\Psi_N^{TA}(t - t_{\text{peak}}) = \sum_{n=0}^{N-1} A_n e^{-Im(\omega_n^{TA})(t-t_{\text{peak}})} \cdot \sin\left(Re(\omega_n^{TA})(t - t_{\text{peak}}) + \phi_n\right), \quad t \in [t_0, t_f].$$

Οι παράμετροι που περιγράφουν κάθε τρόπο είναι τέσσερις: η μιγαδική συχνότητα $\omega_n = Re(\omega_n) - iIm(\omega_n)$, το πλάτος A_n και η φάση ϕ_n , οδηγώντας σε συνολικά $4N$ παραμέτρους.

- (ii.) Ψ_N^{TS} : Αυτό είναι ένα μοντέλο TS, το οποίο ενσωματώνει υποθέσεις για τις συχνότητες και περιλαμβάνει N τρόπους:

$$\Psi_N^{TS}(t - t_{\text{peak}}) = \sum_{n=0}^{N-1} A_n e^{-Im(\omega_n^{TS})(M)(t-t_{\text{peak}})} \cdot \sin\left(Re(\omega_n^{TS})(M)(t - t_{\text{peak}}) + \phi_n\right), \quad t \in [t_0, t_f].$$

Η υπόθεση της συχνότητας εμφανίζεται στο μοντέλο μέσω της επιβολής μιας συχνότητας ω_n^{inj} και μιας μάζας M^{inj} . Συγκεκριμένα, χρησιμοποιούμε το γεγονός ότι το γινόμενο της συχνότητας με τη μάζα είναι σταθερό, και με αυτόν τον τρόπο μπορούμε να θεωρήσουμε τη μάζα ως ελεύθερη παράμετρο:

$$\omega_n^{TS} \cdot M^{TS} = \omega_n^{inj} \cdot M^{inj} \xrightarrow{M^{inj}=1} \omega_n^{TS}(M) = \frac{\omega_n^{inj}}{M^{TS}},$$

όπου η επιβαλλόμενη μάζα ορίζεται στο ένα. Οι παράμετροι που περιγράφουν κάθε τρόπο είναι δύο: το πλάτος A_n και η φάση ϕ_n . Επιπλέον, η μάζα M^{TS} λειτουργεί ως καθολική παράμετρος που περιγράφει και ελέγχει τις τιμές των συχνοτήτων για όλα τα n , όπως φαίνεται στο (6.4), οδηγώντας σε συνολικά $2N + 1$ παραμέτρους.

- (iii.) Ψ_N^{TA-t} : Αυτό είναι το ίδιο μοντέλο **TA** όπως προηγουμένως, το οποίο δεν κάνει υποθέσεις για τις συχνότητες και περιλαμβάνει N τρόπους, αλλά τώρα λαμβάνουμε υπόψη και την ουρά:

$$\begin{aligned} \Psi_N^{TA-t}(t - t_{\text{peak}}) = \sum_{n=0}^{N-1} A_n e^{-Im(\omega_n^{TA})(t-t_{\text{peak}})} \cdot \sin \left(Re(\omega_n^{TA})(t - t_{\text{peak}}) + \phi_n \right) \\ + A_{tail} (t - t_{tail})^{-(2\ell+3)}, \quad t \in [t_0, t_f]. \end{aligned} \quad (\text{B.8})$$

Οι παράμετροι που περιγράφουν κάθε τρόπο είναι τέσσερις: η μιγαδική συχνότητα $\omega_n = Re(\omega_n) - iIm(\omega_n)$, το πλάτος A_n και η φάση ϕ_n , και επιπλέον έχουμε δύο παραμέτρους για να μοντελοποιήσουμε την ουρά: A_{tail}, t_{tail} , οδηγώντας σε συνολικά $4N + 2$ παραμέτρους. Για την περίπτωση μας με $\ell = 2$ και μη στατικά αρχικά δεδομένα, από την εξίσωση (3.13), ο εκθέτης για την ουρά είναι -7 .

- (iv.) Ψ_N^{TS-t} : Αυτό είναι το ίδιο μοντέλο **TS** όπως προηγουμένως, το οποίο ενσωματώνει υποθέσεις για τις συχνότητες και περιλαμβάνει N τρόπους, αλλά τώρα λαμβάνουμε υπόψη την ουρά νόμου δύναμης:

$$\begin{aligned} \Psi_N^{TS}(t - t_{\text{peak}}) = \sum_{n=0}^{N-1} A_n e^{-Im(\omega_n^{TS})(M)(t-t_{\text{peak}})} \cdot \sin \left(Re(\omega_n^{TS})(M)(t - t_{\text{peak}}) + \phi_n \right) \\ + A_{tail} (t - t_{tail})^{-(2\ell+3)}, \quad t \in [t_0, t_f]. \end{aligned} \quad (\text{B.9})$$

Η εξήγηση σχετικά με τις συχνότητες και τη μάζα είναι η ίδια όπως προηγουμένως. Οι παράμετροι που περιγράφουν κάθε τρόπο είναι δύο: το πλάτος A_n και η φάση ϕ_n , και επιπλέον η μάζα είναι παγκόσμια παράμετρος για όλες τις συχνότητες. Έχουμε επίσης δύο επιπλέον παραμέτρους για να μοντελοποιήσουμε την ουρά: A_{tail}, t_{tail} , οδηγώντας σε συνολικά $4N + 1 + 2$ παραμέτρους. Για την περίπτωση μας με $\ell = 2$, ο εκθέτης για την ουρά είναι -7 .

Γενικά, τα μοντέλα **TS** υποδηλώνουν ότι οι υποθέσεις για τις συχνότητες θα μπορούσαν να προέρχονται από οποιαδήποτε θεωρία. Ωστόσο, σε αυτό το κεφάλαιο εστιάζουμε συγκεκριμένα στις δυναμικές **RW** και **PT**. Ανάλογα, κάνουμε δύο διακριτές υποθέσεις: οι τρόποι για κάθε κύμα

αντιστοιχούν είτε στο δυναμικό **Regge-Wheeler** που δίνεται από την εξίσωση (2.31) είτε στο δυναμικό **Pöschl-Teller** που περιγράφεται στην εξίσωση (3.16).

Για το δυναμικό **PT**, θα πρέπει να σημειωθεί ότι την προσαρμόσαμε με το **RW** χρησιμοποιώντας τη μέθοδο που περιγράφεται στην υποενότητα 3.4.5). Οι ακριβείς τιμές για τους πρώτους τρόπους προέρχονται από [77], ενώ οι άλλοι μπορούν να υπολογιστούν αναλυτικά μέσω της εξίσωσης (3.18) αφού γίνει η προσαρμογή του δυναμικού **PT** στο δυναμικό **RW**.

Για να το τονίσουμε ξανά, για κάθε κύμα χρησιμοποιούμε δύο μοντέλα **TS**. Ένα υποθέτει τη σωστή συχνότητα και το άλλο εισάγει σκόπιμα τη λανθασμένη. Συνολικά, χρησιμοποιούμε έξι μοντέλα όταν μελετάμε τα κύματα **PT**, τα οποία δεν περιέχουν την ουρά δύναμης, καθώς αυτή δεν παράγεται από τη δυναμική **PT**, και δώδεκα μοντέλα όταν μελετάμε τα κύματα **RW**.

Ένας τρόπος να μετρήσουμε την ποιότητα κάθε μοντέλου είναι να συγκρίνουμε τις παραμέτρους του με γνωστές τιμές, όποτε αυτό είναι δυνατό. Στην περίπτωσή μας, μπορούμε να το εφαρμόσουμε για δύο παραμέτρους: για τη μάζα, που εξάγεται από τα μοντέλα **TS**,

$$\delta M = \frac{|M_{fit} - M_{inj}|}{M_{inj}}, \quad (\text{B.10})$$

όπου $M_{inj} = 1$ και την συχνότητα

$$\delta \omega = \frac{|\omega_i - \omega_{i,theory}|}{|\omega_{i,theory}|}, \quad (\text{B.11})$$

όπου $\omega_{i,theory}$ είναι η θεωρητική τιμή των σύνθετων συχνοτήτων που αντιστοιχούν στις υποκείμενες δυναμικές, η οποία είναι πάντα γνωστή.

ΔΙΑΔΙΚΑΣΙΑ ΠΡΟΣΑΡΜΟΓΗΣ

Για να προσαρμόσουμε τα μοντέλα στα αριθμητικά δεδομένα, χρησιμοποιούμε τη βιβλιοθήκη **PYTHON scipy** και συγκεκριμένα τη συνάρτηση **curve_fit**, η οποία χρησιμοποιεί τον αλγόριθμο **Levenberg–Marquardt** για να ελαχιστοποιήσει το **Sum of Square Error Function**, όπως ορίζεται στην εξίσωση (5.17). Για περισσότερες λεπτομέρειες, δείτε την Ενότητα 5.2.

Η συνάρτηση **curve_fit** απαιτεί ορισμένα ορίσματα που χρήζουν ειδικής προσοχής. Για παράδειγμα, πρέπει να παρέχουμε εκ των προτέρων τα όρια για τις παραμέτρους. Αν τα όρια είναι πολύ στενά, ορισμένες από τις παραμέτρους μπορεί να περιοριστούν από αυτά και να αποτρέψουν τον αλγόριθμο βελτιστοποίησης από το να βρει το παγκόσμιο ελάχιστο. Για να το αποφύγουμε αυτό, διασφαλίζουμε ότι τα όρια είναι αρκετά ευρύτατα.

Όλα τα μοντέλα απαιτούν ένα προκαθορισμένο παράθυρο προσαρμογής που ξεκινά από $t_0 - t_{\text{peak}}$ και τελειώνει στο $t_f - t_{\text{peak}}$. Γι' αυτόν τον λόγο, στους ορισμούς των μοντέλων έχουμε $t \in [t_0, t_f]$. Για να καθορίσουμε το παράθυρο προσαρμογής, πρέπει να προσδιορίσουμε τις αρχικές και τελικές χρονικές στιγμές. Αυτά τα όρια δεν είναι αυστηρά καθορισμένα [78] και, για παράδειγμα, η επιλογή του t_0 σχετίζεται με την ακόμη σε εξέλιξη συζήτηση σχετικά με τον χρόνο εγκυρότητας της γραμμικής υποχώρησης σε σχέση με το πλήρες κύμα που εξάγεται από προσομοιώσεις αριθμητικής σχετικότητας [39–41].

Η επιλογή της τελικής χρονικής στιγμής φαίνεται πιο απλή με την πρώτη ματιά. Θα μπορούσε κανείς να πει ότι αν δεν θέλαμε να μελετήσουμε την επίδραση της ουράς δύναμης, θα μπορούσαμε να επιλέξουμε μια τελική χρονική στιγμή που να μην την περιλαμβάνει, όπως γίνεται στην [39]. Για να είμαστε πιο ακριβείς, δεν είναι ότι η ουρά είναι απύσαστο στο πρώτο κύμα, αλλά μάλλον ότι οι QNMs κυριαρχούν σε αυτήν. Παρατηρήστε, για παράδειγμα, ότι στην Εικόνα 6.1, η συνεισφορά της εξωθημένης ουράς είναι 22 παραγόντων μεγέθους μικρότερη από εκείνη των QNMs. Ωστόσο, στην επόμενη Ενότητα 6.4, αντιμετωπίζουμε την τελική χρονική στιγμή ως ελεύθερη παράμετρο και βλέπουμε ότι η επίδρασή της στις εξαγόμενες παραμέτρους δεν είναι τόσο σημαντική. Αυτό σημαίνει ότι για σταθερό χρόνο εκκίνησης $t_0 - t_{\text{peak}}$, η εξαγωγή της σύνθετης συχνότητας του θεμελιώδους τρόπου παραμένει πιο σταθερή καθώς μεταβάλλουμε την τελική χρονική στιγμή $t_f - t_{\text{peak}}$, σε σύγκριση με το να μεταβάλλουμε αντίστοιχα τον χρόνο εκκίνησης.

Αντίθετα, ο χρόνος εκκίνησης του παραθύρου προσαρμογής $t_0 - t_{\text{peak}}$ είναι λίγο πιο περίπλοκος. Υπάρχουν διαφορετικές προσεγγίσεις για να τον επιλέξουμε [78]. Εδώ αντιμετωπίζεται ως ελεύθερη παράμετρος και για να ποσοτικοποιήσουμε αυτές τις επιπτώσεις στην απόδοση των μοντέλων, ορίζουμε την εξής ποσότητα:

$$M = 1 - \frac{\langle \Psi_{\text{signal}}, \Psi_{\text{fit}} \rangle}{\sqrt{\langle \Psi_{\text{signal}}, \Psi_{\text{signal}} \rangle \langle \Psi_{\text{fit}}, \Psi_{\text{fit}} \rangle}}, \quad (\text{B.12})$$

όπου

$$\langle \Psi_{\text{signal}}(t), \Psi_{\text{fit}}(t) \rangle = \int_{t_0}^{t_f} \Psi_{\text{signal}}(t) \cdot \Psi_{\text{fit}}(t) dt. \quad (\text{B.13})$$

που ονομάζεται *Mismatch*. Καθώς το προσαρμοσμένο μοντέλο Ψ_{fit} πλησιάζει το παραγόμενο κύμα Ψ_{signal} , η διαφορά (*mismatch*) πλησιάζει το μηδέν, γεγονός που υποδηλώνει ότι μια καλή προσαρμογή οδηγεί σε πολύ μικρή διαφορά. Επομένως, αλλάζοντας το t_0 , μελετάμε πόσο τα μοντέλα ταιριάζουν με το παραγόμενο κύμα, εξετάζοντας τη διαφορά.¹

Τέλος, για κάθε t_0 , πρέπει να παρέχουμε μια αρχική εκτίμηση για τις παραμέτρους προκειμένου να ξεκινήσουμε τον αλγόριθμο βελτιστοποίησης. Εάν αυτή η αρχική εκτίμηση είναι κοντά στο πραγματικό ελάχιστο της *Sum of Square Error Function*, ο αλγόριθμος συγκλίνει πιο γρήγορα σε αυτό. Έτσι, αν κάνουμε μια καλή αρχική εκτίμηση, μπορούμε να επιταχύνουμε τη διαδικασία. Αν κάνουμε μια εξαιρετικά κακή αρχική εκτίμηση, μπορεί να κολλήσουμε σε ένα τοπικό ελάχιστο και να αποκτήσουμε μεροληπτικές παραμέτρους.

Υποθέτοντας ότι οι εξαγόμενες παράμετροι βελτιώνονται καθώς αυξάνεται το t_0 , δεδομένου ότι το μεταβατικό μέρος του κύματος αποκλείεται όλο και περισσότερο από την προσαρμογή, εφαρμόζουμε την ακόλουθη διαδικασία, η οποία απεικονίζεται σχηματικά στην Εικόνα 6.2. Για το πρώτο t_0 , δεν έχουμε προηγούμενες παραμέτρους στις οποίες να βασιστούμε. Έτσι, σχεδιάζουμε την αρχική εκτίμηση τυχαία από μια ομοιόμορφη κατανομή, καλύπτοντας το επιτρεπτό εύρος των παραμέτρων. Για τα επόμενα t_0 , με βάση την υπόθεσή μας ότι οι παράμετροι βελτιώνονται,

¹ Υπάρχει μια πιθανή παγίδα στο παραπάνω. Οι καλύτερες προσαρμοσμένες συναρτήσεις που διαφέρουν μόνο κατά ένα σταθερό παράγοντα δίνουν την ίδια διαφορά, καθώς αυτός ο παράγοντας ακυρώνεται. Έτσι, θα μπορούσαμε να έχουμε σχεδόν μηδενική διαφορά αλλά λάθος καλύτερες παραμέτρους προσαρμογής.

αντικαθιστούμε την ομοιόμορφη κατανομή με μια κομμένη Γκαουσιανή. Αυτή η προσαρμογή μας επιτρέπει να δώσουμε περισσότερη βαρύτητα σε ορισμένες περιοχές του χώρου παραμέτρων. Αυτή η Γκαουσιανή κόβεται στις άκρες του επιτρεπτού εύρους παραμέτρων και η μέση τιμή της τοποθετείται ακριβώς στις παραμέτρους που εξήχθησαν από την προηγούμενη προσαρμογή του t_0 . Το πλάτος ορίζεται στο $25M$ με αυτόν τον τρόπο, επιταχύνουμε τη διαδικασία ξεκινώντας από μια εκτίμηση που είναι σχετικά κοντά στο ελάχιστο.

Τέλος, επαναλαμβάνουμε την προσαρμογή για κάθε t_0 τουλάχιστον 50 φορές, ανάλογα με το μοντέλο, καθεμία με τυχαίες παραμέτρους που αντλούνται από την κομμένη Γκαουσιανή, προκειμένου να διασφαλίσουμε ότι ο αλγόριθμος βελτιστοποίησης δεν έχει κολλήσει σε ένα τοπικό ελάχιστο. Από αυτές τις προσαρμογές, επιλέγουμε τις παραμέτρους που αντιστοιχούν στη ελάχιστη διαφορά M .

Παρατηρούμε ότι, όπως συζητείται εκτενώς στο [40], ένα μικρό **mismatch** δεν είναι πανάκεια; μπορεί επίσης να οδηγήσει σε **overfitting**. Οι συγγραφείς δείχνουν ότι περιλαμβάνοντας έως και $N = 8$ συχνότητες σε διάφορα μοντέλα, η ασυμφωνία είναι πολύ μικρή, ακόμη και κοντά στην κορυφή. Αυτό το φαινομενικά θετικό αποτέλεσμα, κρύβει το γεγονός ότι η ανθεκτικότητα των εξαγόμενων παραμέτρων επιδεινώνεται για υψηλότερες αρμονικές. Ως εκ τούτου, ενώ η προσαρμογή φαίνεται ακριβής, μπορεί στην πραγματικότητα να είναι ένα αποτέλεσμα του **overfit**.

ΑΠΟΤΕΛΕΣΜΑΤΑ ΓΙΑ ΔΥΝΑΜΙΚΟ PÖSCHL-TELLER

Η αρχική εφαρμογή εστιάζει στη μελέτη των κυματομορφών που παράγονται από τη σκέδαση ενός Γκαουσιανού κυματοπακέτου στο το δυναμικό Pöschl-Teller (PT). Πραγματοποιούμε τις προσαρμογές χρησιμοποιώντας τα μοντέλα TA και TS, συνολικά έξι διαφορετικά, που ορίζονται στις εξισώσεις (??) και (??) αντίστοιχα. Για το TS εξετάζουμε τις συχνότητες που προέρχονται είτε από το δυναμικό PT (σωστές) είτε από το RW (λανθασμένες). Οι προσαρμογές επαναλαμβάνονται για διαφορετικούς χρόνους έναρξης που κυμαίνονται από $t_0 - t_{\text{peak}} = -20M$ έως $50M$ με βήμα $1M$ και απεικονίζουμε όλες τις εξαγόμενες παραμέτρους ως συνάρτηση του χρόνου έναρξης.

Η απόδοση κάθε μοντέλου απεικονίζεται στην Εικόνα 6.3, όπου απεικονίζουμε τις διαφορές για διαφορετικούς χρόνους έναρξης της προσαρμογής. Στην περιοχή πριν την κορυφή - όπου οι συχνότητες δεν έχουν σχηματιστεί πλήρως ακόμα - όλες οι διαφορές είναι μεγάλες, υποδεικνύοντας ότι οι εξασθενημένες ημιτονοειδείς δεν μπορούν να περιγράψουν με ακρίβεια αυτήν την περιοχή του κύματος, όπως αναμενόταν.

Μπορούν να παρατηρηθούν δύο γενικές τάσεις: οι διαφορές μειώνονται καθώς αυξάνεται ο χρόνος έναρξης και οι διαφορές των μοντέλων με $N = 2$ είναι μικρότερες από τις αντίστοιχες με $N = 1$. Η πρώτη τάση μπορεί να αποδοθεί στο γεγονός ότι σε αρκετά καθυστερημένους χρόνους, το μεταβατικό περιεχόμενο έχει εξαφανιστεί και το περιεχόμενο υψηλών αρμονικών έχει αποσβεστεί, με αποτέλεσμα η θεμελιώδης συχνότητα να κυριαρχεί πάνω στο σήμα. Η δεύτερη τάση οφείλεται στον μεγαλύτερο χώρο παραμέτρων που παρέχει μεγαλύτερη ευελιξία.

Επισημαίνεται ότι και τα δύο μοντέλα Theory Specific επιδεικνύουν παρόμοια απόδοση σε πρώιμους χρόνους. Τα μοντέλα TS GR έχουν χειρότερη απόδοση από τα TS PT μόνο σε

καθυστερημένους χρόνους, μετά από $30M$ για το μοντέλο $N = 1$ και $20M$ για το μοντέλο $N = 2$, όπου επίπεδωσαν σε σχεδόν σταθερή τιμή περίπου $\sim 10^{-6}$.

Τέλος, το μοντέλο TA με $N = 2$ φαίνεται να επιτυγχάνει ελαφρώς καλύτερα από το αντίστοιχο TS PT σε πολύ καθυστερημένους χρόνους. Μια πιθανή εξήγηση για αυτό μπορεί να αποδοθεί στον μεγαλύτερο χώρο παραμέτρων του, ο οποίος παρέχει μεγαλύτερη ευελιξία και του επιτρέπει να αποτυπώσει καλύτερα τα αριθμητικά σφάλματα, τα οποία θα πρέπει να είναι παρόντα για τόσο μικρές διαφορές [39]. Δεδομένων των μικρών διαφορών που αποκτήθηκαν, μπορούμε να συμπεράνουμε ότι τα μοντέλα μας μπορούν να προσαρμοστούν ικανοποιητικά στο κύμα. Από εδώ και πέρα, η προσοχή μετατοπίζεται στην ποιότητα της εξαγωγής παραμέτρων.

Ξεκινάμε από τη μάζα, M_{fit} . Όπως φαίνεται στην επάνω εικόνα της Εικόνας 6.4, όλα τα μοντέλα TS PT πλησιάζουν την τιμή 1 και τα μοντέλα TS GR πλησιάζουν μια τιμή κοντά σε αυτήν αλλά όχι ακριβώς 1. Επομένως, τα μοντέλα TS PT που υποθέτουν σωστές συχνότητες προσεγγίζουν καλύτερα τη μάζα που έχει εγχυθεί, ενώ η απόδοση των μοντέλων TS GR επίπεδωσε σε μια λανθασμένη τιμή περίπου $10M$ και $30M$ για το μοντέλο που περιέχει τρόπους $N = 1$ και $N = 2$ αντίστοιχα. Στην κάτω εικόνα δείχνουμε το σχετικό σφάλμα της εξαγόμενης μάζας που υπολογίζεται από την εξίσωση (B.10) και βλέπουμε ότι η τιμή της για τα μοντέλα TS GR σταθεροποιείται, ενώ για τα TS PT συνεχίζει να βελτιώνεται. Το αναμενόμενο σε αυτά τα διαγράμματα είναι ότι τα μοντέλα TS GR, τα οποία περιέχουν τη λανθασμένη συχνότητα, αποκαθιστούν τη μάζα πιο ακριβώς σε πρώιμους χρόνους, όπως φαίνεται στην κάτω Εικόνα.

Η επόμενη παράμετρος που συζητάμε είναι η ανακτηθείσα συχνότητα $\omega = Re(\omega) - iIm(\omega)$. Σημειώστε ότι το φάσμα PT έχει το ίδιο πραγματικό μέρος για όλες τις συχνότητες. Τα αποτελέσματα για τα πραγματικά και φανταστικά μέρη εμφανίζονται στα επάνω και κάτω πάνελ αντίστοιχα της Εικόνας 6.5). Η πρώτη παρατήρηση είναι ότι για πρώιμους χρόνους, και ειδικά πριν από την κορυφή, οι προβλέψεις αποκλίνουν πολύ από τις αναμενόμενες τιμές που απεικονίζονται με μαύρες γραμμές. Η σύγκλιση στις αναμενόμενες τιμές αρχίζει μετά την κορυφή και ειδικά για αρκετά καθυστερημένους χρόνους, όλα τα μοντέλα βρίσκουν τις σωστές συχνότητες, εκτός από τα μοντέλα TS GR (βλ. την ενσωματωμένη εικόνα που εστιάζει στην περιοχή των καθυστερημένων χρόνων).

Ακόμη, τα μοντέλα που είναι TS συγκλίνουν γρηγορότερα από τα TA, αλλά τα τελευταία πλησιάζουν πιο κοντά στις σωστές συχνότητες (βλ. Παράρτημα A και Εικόνα A.1). Επιπλέον, η θεμελιώδης συχνότητα που εξάγεται από μοντέλα που περιέχουν δύο καταστάσεις συγκλίνει γρηγορότερα από τα μοντέλα που περιέχουν μία συχνότητα.

Στη θεωρία γραμμικών διαταραχών, κάθε συχνότητα έχει σταθερό πλάτος και φάση. Ως εκ τούτου, για να ισχυριστεί κανείς ότι μια συχνότητα βρίσκεται σε ένα σήμα, το πλάτος και η φάση της πρέπει επίσης να εξάγονται σταθερά. Αυτές οι παράμετροι δεν είναι τόσο θεμελιώδεις όσο οι ίδιες οι συχνότητες, καθώς εξαρτώνται από την Initial Condition που χρησιμοποιήθηκε για την παραγωγή του κύματος. Ωστόσο, η σταθερή εξαγωγή της συχνότητας από μόνη της δεν εγγυάται την ανίχνευση της συχνότητας. Στην Εικόνα 6.6 απεικονίζουμε τα πλάτη για τη θεμελιώδη συχνότητα A_0 και την πρώτη αρμονική A_1 (βλ. Παράρτημα A και Εικόνα A.1 για τα αντίστοιχα διαγράμματα για τη φάση). Το πλάτος για τη θεμελιώδη συχνότητα εξάγεται με σταθερό και σταθερό τρόπο σε καθυστερημένους χρόνους από όλα τα μοντέλα, πιστοποιώντας τη σύγκλιση της συχνότητας. Ωστόσο, για την πρώτη αρμονική, το πλάτος γίνεται σταθερό μόνο

για πολύ καθυστερημένους χρόνους μόνο για τα μοντέλα TA και TS PT, ενώ για το TS GR αποκλίνει, πράγμα που σημαίνει ότι αυτό το συγκεκριμένο μοντέλο απέτυχε να βρει την πρώτη αρμονική του σήματος.

Μια τελευταία γενική παρατήρηση μπορεί να γίνει σχετικά με το γεγονός ότι τα μοντέλα TS GR προβλέπουν λανθασμένες συχνότητες με αρκετή ακρίβεια και σταθερότητα. Αυτό σημαίνει ότι αν δεν γνωρίζαμε το σωστό υποκείμενο φάσμα του κύματος και υποθέταμε ότι προερχόταν από ένα δυναμικό GR, θα μπορούσαμε ενδεχομένως να είμαστε ικανοποιημένοι με τα αποτελέσματα, εάν δεν είχαμε πολλά μοντέλα για σύγκριση. Επομένως, αυτό θα μπορούσε να χρησιμεύσει ως ένα πειραματικό παράδειγμα για μεροληπτικά μοντέλα. Για λανθασμένες υποθέσεις, δηλαδή συχνότητες GR για ένα κύμα PT, οι εξαγόμενες παράμετροι ήταν σταθερές, αν και λανθασμένες.

ΑΠΟΤΕΛΕΣΜΑΤΑ ΓΙΑ ΔΥΝΑΜΙΚΟ REGGE-WHEELER

Η δεύτερη εφαρμογή είναι μια επανάληψη των προηγούμενων υπολογισμών, αλλά για το δυναμικό RW. Η κύρια διαφορά μεταξύ των δύο περιπτώσεων είναι ότι το RW έχει διαφορετική ασυμπτωτική συμπεριφορά, η οποία οδηγεί σε μια ουρά για μεγάλους χρόνους έναρξης της προσαρμογής. Όπως θα συζητήσουμε, αυτό επιδεινώνει την εξαγωγή των παραμέτρων. Πιθανές λύσεις γι' αυτό θα μπορούσαν να είναι η συμπερίληψη της ουράς στα μοντέλα ή η εξαίρεση της ουράς από το παράθυρο προσαρμογής. Όπως θα δούμε με περισσότερες λεπτομέρειες στην Ενότητα 6.4, η πρώτη προσέγγιση λειτουργεί, ενώ η δεύτερη όχι.

Χρησιμοποιούμε όλα τα συγκεκριμένα μοντέλα TA και TS που ορίζονται στις εξισώσεις (6.2), (B.8), (6.3) και (B.9), με συμπεριλαμβανόμενους τρόπους $N = 1$ ή $N = 2$ και λαμβάνουμε επίσης υπόψη την ουρά. Συνολικά, εφαρμόζουμε δώδεκα διαφορετικά μοντέλα. Όπως και πριν, για τα μοντέλα TS, εξετάζουμε τόσο τις σωστές συχνότητες GR όσο και τις λανθασμένες PT και επαναλαμβάνουμε τις προσαρμογές από $t_0 - t_{\text{peak}} = -20M$ έως $60M$ με βήμα $1M$.

Πρώτα έρχονται τα διαγράμματα Mismatch στην Εικόνα 6.7, τα οποία παρουσιάζουν παρόμοια συμπεριφορά με πριν, υποδεικνύοντας τη συμφωνία μεταξύ της προσαρμοσμένης συνάρτησης και της αριθμητικής κυματομορφής. Όλα τα μοντέλα με κατάσταση $N = 1$ (στερεές γραμμές στο επάνω πάνελ) αποδίδουν αρκετά παρόμοια. Παρατηρήστε το ελάχιστο γύρω από $t_0 - t_{\text{peak}} \simeq 10M$ και τη ανιούσα συμπεριφορά στη συνέχεια. Δεν παρατηρήσαμε μια τέτοια συμπεριφορά για το κύμα PT, οπότε μπορεί να αποδοθεί στην καθυστερημένη ουρά. Πράγματι, όταν μοντελοποιούμε την ουρά (διακεκομμένες γραμμές στο επάνω πάνελ), οι ασυμφωνίες μειώνονται από δύο έως τέσσερις τάξεις μεγέθους (ανάλογα με το μοντέλο) και ταυτόχρονα δεν παρατηρείται καμία ανιούσα τάση.

Παρόμοια είναι η συμπεριφορά των προσαρμογών με συχνότητες $N = 2$. Η διαφορά εδώ είναι ότι φτάνουν το ελάχιστο ασυμφωνίας νωρίτερα από τα αντίστοιχα μοντέλα με $N = 1$, καθώς αποτυπώνουν καλύτερα την πρώτη αρμονική που είναι παρούσα νωρίτερα στο κύμα και έχει εξασθενήσει σε μεταγενέστερους χρόνους. Η ένδειξη από τα διαγράμματα ασυμφωνίας είναι και πάλι ότι τα μοντέλα ταιριάζουν αρκετά καλά με το σήμα και από εδώ και πέρα θα συζητήσουμε τη σχέση της μικρής ασυμφωνίας με την ποιότητα και τη σταθερότητα των εξαγόμενων παραμέτρων.

Τώρα περνάμε στη εξαγόμενη μάζα, που απεικονίζεται στην Εικόνα 6.8, φέρνοντάς μας

στο νέο σημείο όπου η βελτίωση που παρέχεται από την μοντελοποίηση της ουράς γίνεται πιο σαφής. Στο επάνω πάνελ απεικονίζουμε την εξαγόμενη μάζα M_{fit} ως συνάρτηση του χρόνου εκκίνησης της προσαρμογής και στο κάτω πάνελ, το σχετικό σφάλμα της. Σημειώστε ότι τα μοντέλα χωρίς την ουρά (στερεές γραμμές και στα δύο πάνελ) ταλαντώνονται γύρω από μια συγκεκριμένη τιμή. Τα μοντέλα TS PT με τη λανθασμένη συχνότητα, βρίσκουν μια λανθασμένη τιμή με σχετικό σφάλμα $\sim 10^{-2}$, ενώ τα μοντέλα TS GR που περιέχουν τη σωστή συχνότητα, ταλαντώνονται γύρω από τη σωστή τιμή του 1, με σχετικό σφάλμα περίπου ενός τάξης μεγέθους μικρότερο.

Αυτή η ταλαντευόμενη πλατφόρμα, ακόμη και για το μοντέλο που περιέχει τις σωστές συχνότητες, είναι αντίθεση με την αντίστοιχη Εικόνα 6.4 για το κύμα PT. Η διαφορά οφείλεται στην παρουσία της ουράς με νόμο δύναμης που περιορίζει τη συνεχή βελτίωση της τιμής της μάζας γύρω από $t_0 - t_{peak} \gtrsim 10M$ έως $20M$ για διαφορετικά μοντέλα.

Ωστόσο, όταν μοντελοποιούμε ρητά την καθυστερημένη ουρά (διακεκομμένες γραμμές), παρατηρούμε ακόμη και με γυμνό μάτι στο επάνω πάνελ ότι η εξαγόμενη μάζα σταθεροποιείται γύρω από τη λανθασμένη τιμή για τα μοντέλα TS PT και γύρω από τη σωστή τιμή για τα μοντέλα TS GR. Από το κάτω πάνελ βλέπουμε ότι, στην πραγματικότητα, όσον αφορά τα TS GR, η ταλάντωση του σχετικού σφάλματος είναι μικρότερη κατά δύο τάξεις μεγέθους.

Επιπλέον, οι γενικές τάσεις είναι ότι τα μοντέλα με δύο τρόπους και τα μοντέλα με ουρές φτάνουν στην "τελική τους κατάσταση", είτε ταλαντωμένα είτε σταθερά, πιο γρήγορα από τα μοντέλα με έναν τρόπο και τα μοντέλα χωρίς ουρές. Η εξαγωγή της μάζας συνολικά είναι αρκετά λογική, καθώς δεν αποκλίνει, είναι σταθερή και επιπλέον, τα διαφορετικά αποτελέσματα μεταξύ διαφορετικών μοντέλων μπορούν να εξηγηθούν λογικά.

Σε αυτό το στάδιο, πρέπει να επεξεργαστούμε ένα σημείο που, μόλις παρατηρηθεί, θα μπορούσε να καταταγεί στην κατηγορία "not even wrong". Συγκεκριμένα, δύο από τα μοντέλα που χρησιμοποιούνται είναι τα TS PT με ουρά. Δηλαδή, σε ένα μοντέλο συγκεκριμένου τύπου, του οποίου το φάσμα υποτίθεται ότι προέρχεται από μια δυνητική χωρίς ουρά, περιλαμβάνεται μια καθυστερημένη ουρά. Εννοιολογικά, αυτό είναι εντελώς λανθασμένο. Ωστόσο, υπάρχει μια εξήγηση για αυτό και προσφέρει κάτι πολύτιμο.

Αν παραμερίσουμε προσωρινά τον χωρίς ουρά χαρακτήρα του φάσματος PT και θεωρήσουμε αυτές τις εισαχθείσες συχνότητες απλώς ως δύο συχνότητες που είναι διαφορετικές από αυτές που περιλαμβάνονται στο σήμα, αυτό που παρατηρούμε είναι ένα ενδιαφέρον σημείο. Ο συνδυασμός της ουράς με τη λανθασμένη συχνότητα βελτιώνει την προσαρμογή μειώνοντας τη διαφορά (mismatch), όπως φαίνεται στην Εικόνα 6.7, και σταθεροποιώντας την εξαγωγή της μάζας, όπως φαίνεται στην Εικόνα 6.8. Έτσι, η σωστή μοντελοποίηση ορισμένων τμημάτων του σήματος οδηγεί σε πιο σταθερά αποτελέσματα, ακόμα κι αν υποτίθεται ότι οι συχνότητες είναι λανθασμένες.

Τώρα συζητάμε την εξαγωγή των συχνοτήτων που φαίνονται στην Εικόνα 6.9, όπου στην αριστερή και τη δεξιά στήλη βλέπουμε τις μιγαδικές συχνότητες της θεμελιώδους συχνότητας και της πρώτης αρμονικής αντίστοιχα. Υπάρχει επίσης η αντίστοιχη Εικόνα 6.10, η οποία δείχνει τα σχετικά σφάλματα των σύνθετων συχνοτήτων που ορίζονται στην εξίσωση (B.11). Αυτή η

συζήτηση απεικονίζει και πάλι την βελτίωση που προκύπτει από την μοντελοποίηση των ουρών και επίσης αποκαλύπτει τα προβληματικά χαρακτηριστικά ορισμένων μοντέλων.

Αναφορικά με τη θεμελιώδη συχνότητα (αριστερή στήλη), όλα τα μοντέλα TS PT προβλέπουν μια λανθασμένη τιμή με σχετικό σφάλμα περίπου 2%, ενώ όλα τα άλλα προσεγγίζουν τις σωστές τιμές με τουλάχιστον μία τάξη μεγέθους μικρότερο σχετικό σφάλμα. Σημειώστε ότι οι συχνότητες από τα μοντέλα χωρίς ουρά (στερεές γραμμές) ταλαντώνονται γύρω από μια συγκεκριμένη τιμή. Η εξαίρεση είναι το μοντέλο 2 TA, το οποίο σταθεροποιεί την εξαγωγή της θεμελιώδους συχνότητας (βλ. τη κίτρινη γραμμή στην εισαγωγή της Εικόνας 6.9 και την Εικόνα 6.10).

Οι συχνότητες της πρώτης αρμονικής (δεξιά πάνελ) εξάγονται με σταθερό τρόπο για τα μοντέλα TS (πάλι λανθασμένη τιμή για TS PT και σωστή για TS GR). Αυτό οφείλεται στο γεγονός ότι είναι ο λόγος της υποτιθέμενης συχνότητας προς την εξαγόμενη μάζα, η οποία εξάγεται σταθερά με διαφορετική ακρίβεια ανάλογα με το μοντέλο. Ωστόσο, το μοντέλο TA είναι εξαιρετικά ασταθές και δεν ανακατά καθόλου την αρμονική (κίτρινη γραμμή).

Εάν δεν είχαν παρουσιαστεί άλλες γραφικές παραστάσεις, θα μπορούσε κανείς να συμπεράνει ότι όλα τα μοντέλα TS μπορούν να εξάγουν αξιόπιστα την πρώτη αρμονική από το σήμα. Η Εικόνα 6.11 δείχνει τα εξαγόμενα πλάτη ως συνάρτηση του αρχικού χρόνου. Στο αριστερό πάνελ, παρουσιάζουμε τα αποτελέσματα για τη θεμελιώδη συχνότητα, A_0 , η οποία έχει παρόμοια συμπεριφορά με τις άλλες παραμέτρους. Τα μοντέλα που παραλείπουν την ουρά ταλαντώνονται σε μεταγενέστερους χρόνους γύρω από μια συγκεκριμένη τιμή, τα μοντέλα που περιλαμβάνουν την ουρά σταθεροποιούν την εξαγωγή και τα μοντέλα που περιλαμβάνουν την αρμονική επίσης σταθεροποιούν την εξαγωγή, αλλά σε μικρότερο βαθμό. Επιπλέον, τα μοντέλα TS PT αποδίδουν ελαφρώς διαφορετική τιμή από όλα τα άλλα.

Στο δεξί πάνελ της εικόνας, βλέπουμε ότι καμία από τα πλάτη για την πρώτη αρμονική δεν βρέθηκε αξιόπιστα. Όλα αποκλίνουν σε μεγάλες τιμές του αρχικού χρόνου. Έτσι, δεν μπορούμε να συμπεράνουμε με σιγουριά ότι ανιχνεύσαμε την πρώτη αρμονική σε αυτό το συγκεκριμένο παραγόμενο σήμα με τη διαδικασία που ακολουθήθηκε. Αν συγκρίνουμε με τα αντίστοιχα αποτελέσματα από το κύμα PT, όπου μόνο το μοντέλο 2 TA απέτυχε να ανιχνεύσει την αρμονική (Εικόνα 6.6), μπορούμε να εντοπίσουμε τον λόγο αυτής της διαφοράς πίσω από την ουρά. Παρόμοια αποτελέσματα για τις φάσεις μπορούν να βρεθούν στο Παράρτημα A στην Εικόνα A.3.

Τέλος, συζητάμε αν η εξαγωγή της ουράς ήταν σταθερή ή όχι και παρουσιάζουμε σχετικά αποτελέσματα στο Σχήμα 6.12. Και το πλάτος της και ο πόλος της βρέθηκαν να έχουν παρόμοια συμπεριφορά. Για αρχικούς χρόνους, έως $t_0 - t_{\text{peak}} \sim 10M$, οι παράμετροι είναι αρκετά ασταθείς, πράγμα που σημαίνει ότι η συμβολή τους στο σήμα δεν είναι τόσο μεγάλη σε σύγκριση με άλλες συμβολές.

Ωστόσο, μετά από $t_0 - t_{\text{peak}} \sim 20M$ για τα μοντέλα με συχνότητες $N = 1$ και $t_0 - t_{\text{peak}} \sim 10M$ για τα μοντέλα με συχνότητες $N = 2$ παρατηρούμε είτε μια ταλαντούμενη συμπεριφορά γύρω από μια ορισμένη τιμή είτε μια σύγκλιση σε μια σταθερή τιμή, αντίστοιχα. Μια διαισθητική εξήγηση για αυτή τη διαφορά θα μπορούσε να είναι ότι τα μοντέλα με κατάσταση $N = 2$ καταγράφουν καλύτερα το ταλαντούμενο μέρος του σήματος, αφήνοντας έτσι ένα σήμα που περιέχει μια πιο καθαρή μορφή της ουράς.

ΕΦΑΡΜΟΓΕΣ ΚΑΙ ΑΠΟΤΕΛΕΣΜΑΤΑ II

Σε αυτό το κεφάλαιο παρουσιάζουμε τη δεύτερη σειρά αποτελεσμάτων, εστιάζοντας στην φαινομενολογική επέκταση στο **GR ringdown**, γνωστή και ως **Parametrized Quasi-Normal Mode Framework (PF)**. Παρόμοια με πριν, παράγουμε γραμμικά κύματα **ringdown**, αλλά πάνω στο δυναμικό **GR** προσθέτουμε τροποποιήσεις δυνάμεων $1/r$ και εξάγουμε τις παραμέτρους προσαρμόζοντας τις εκθετικά αποσβεννύμενες ημιτονικές συναρτήσεις με ουρές.

ΜΕΤΑΒΟΛΗ ΜΙΑΣ ΔΥΝΑΜΗΣ ΤΗΝ ΦΟΡΑ

Προσθέτουμε μία μόνο τροποποίηση αντίστροφης δύναμης του r στο αξονικό δυναμικό **GR**. Μία μόνο τροποποίηση στην εξίσωση (4.6)), σημαίνει ότι το δυναμικό γίνεται

$$V(r) = V^{\text{GR}}(r) + \frac{1}{r_H^2} \alpha^{(k)} \left(\frac{r_H}{r} \right)^k. \quad (\text{B.14})$$

Ως εκ τούτου, η τροποποίηση ελέγχεται απόλυτα από δύο παραμέτρους, το πλάτος της $\alpha^{(k)}$ και την εκθετική παράμετρο k , για την οποία εξετάζουμε $k = 2, \dots, 7$. Ο στόχος είναι να σκιαγραφήσουμε τις συνδέσεις μεταξύ αυτών των δύο παραμέτρων και των χαρακτηριστικών των κυμάτων, τα οποία, αν αντιμετωπιστούν αντίστροφα, οδηγούν στις ιδιότητες του υποκείμενου δυναμικού.

Η μέθοδος που ακολουθούμε είναι η ίδια με αυτή που παρουσιάζεται στην Ενότητα 6.1. Σε συντομία, παράγουμε ένα κύμα προερχόμενο από τα ίδια αρχικά δεδομένα αλλά από το τροποποιημένο δυναμικό, εξάγουμε το σήμα στο πεδίο του χρόνου σταθεροποιώντας την τοποθεσία ενός παρατηρητή και προσαρμόζουμε το μοντέλο **Theory Agnostic** της εξίσωσης (B.8), το οποίο περιλαμβάνει ένα αποσυνδεδεμένο ημίτονο και μια ουρά. Εκτελούμε την προσαρμογή για διαφορετικούς χρόνους εκκίνησης, για τον καθένα επαναλαμβάνουμε τουλάχιστον 100 φορές και κρατάμε την καλύτερη προσαρμογή που παρέχει την μικρότερη απόκλιση. Ο λόγος που περιλαμβάνουμε την ουρά στις προσαρμογές μπορεί να αναχθεί στην Ενότητα 6.3. Εκεί, σε όλες τις εικόνες οι μπλε στερεές γραμμές αναφέρονται στο $N = 1 \text{ TA}$ και οι μπλε διακεκομμένες γραμμές στο μοντέλο ουράς $N = 1 \text{ TA}$. Το μοντέλο ουράς $N = 1 \text{ TA}$ παρέχει πιο ακριβή και πιο σταθερά αποτελέσματα.

Επιπλέον, στο Παράρτημα B, παρουσιάζουμε κάποιες εικόνες της ίδιας ανάλυσης αλλά για ένα μοντέλο που περιλαμβάνει μόνο τη θεμελιώδη συχνότητα χωρίς την ουρά.

Ως πρώτη ένδειξη για την επιτυχία των προσαρμογών, δείχνουμε στην Εικόνα 7.1 τις αποκλίσεις ως συνάρτηση του χρόνου εκκίνησης. Διάφορες δυνάμεις του $k \in [2, 7]$ εμφανίζονται σε κάθε πάνελ και διαφορετικές τιμές για τα πλάτη, $\alpha^{(k)} \in [-1.5, 1.5]$ εμφανίζονται στην κλίμακα χρωμάτων. Η συμπεριφορά των αποκλίσεων είναι παρόμοια, εκτός από την περίπτωση του $k = 2$ με αρνητικά πλάτη.

Από τώρα και στο εξής, στρεφόμαστε στην ποιότητα των εξαγόμενων παραμέτρων. Στην Εικόνα 7.2 παρουσιάζουμε τα καλύτερα αποτελέσματα προσαρμογής για το θεμελιώδες QNM ως συνάρτηση του πλάτους της τροποποίησης, $\omega_0(a^{(k)})$. Συγκεκριμένα, διαφορετικά πάνελ αναφέρονται σε διαφορετικές δυνάμεις k και διαφορετικοί δείκτες αναφέρονται σε δύο διαφορετικούς χρόνους εκκίνησης $t_0 - t_{\text{peak}} = 10M$ και $30M$. Η κόκκινη γραμμή αντιστοιχεί στην θεωρητική προβλεπόμενη τιμή σε παρα-perturbative επίπεδο κατά δεύτερη τάξη όπως υπολογίζεται στο [70].

Με την γκρι σκιασμένη περιοχή, δείχνουμε τη διαφορά μεταξύ των γραμμικών και των τετραγωνικών προβλέψεων και με αυτόν τον τρόπο υποδεικνύουμε το συστηματικό σφάλμα που προέρχεται από την ενσωμάτωση της τετραγωνικής διόρθωσης πάνω από τη γραμμική.

Σημειώστε ότι οι εξαγόμενες QNMs συμφωνούν με την πρόβλεψη για τις χρονικές στιγμές αργά (μπλε κύκλοι). Η μόνη διαφωνία μπορεί να παρατηρηθεί για αρνητικές τιμές του $a^{(2)}$. Ο πιο πιθανός λόγος σχετίζεται με τις κάθετες μαύρες διακεκομμένες γραμμές. Αυτές οι γραμμές προέρχονται από την εξίσωση (4.4) και υποδεικνύουν μια χονδρική εκτίμηση της μεγαλύτερης τιμής κάθε $a^{(k)}$, κάτω από την οποία η PF υποτίθεται ότι είναι ακριβής. Οι γραμμές για $k \geq 4$ βρίσκονται πέρα από τα όρια των αξόνων. Αυτός ο ανώτατος περιορισμός δείχνει την περιοχή στην οποία θα έπρεπε να λειτουργεί το πλαίσιο. Δεν σημαίνει ότι δεν θα λειτουργήσει πέρα από αυτό.

Παρατηρούμε ότι γενικά το πλαίσιο λειτουργεί ακόμη και πέρα από αυτές τις γραμμές με την μόνη εξαίρεση αυτή τη μικρή περιοχή του $a^{(2)}$.

Σημειώστε ότι για τη δεδομένη περιοχή πλάτους, η αλλαγή του πραγματικού μέρους γίνεται μικρότερη καθώς αυξάνεται το k . Αυτό είναι διαισθητικό, καθώς μεγαλύτερο k φέρνει μικρότερη τροποποίηση στο δυναμικό, επομένως μικρότερη απόκλιση στον πραγματικό μέρος. Αντίθετα, η συμπεριφορά του φανταστικού μέρους δεν είναι η ίδια και στην πραγματικότητα είναι αντίθετη: το μεγάλο k το τροποποιεί περισσότερο από την τιμή του GR σε σχέση με το μικρό k .

Στην Εικόνα 7.3 έχουμε ένα γράφημα με την ίδια δομή όπως η 7.2, όπου δείχνουμε τα σχε relative errors (που δίνονται στην εξίσωση (B.11)) μεταξύ των εξαγόμενων και των προβλεπόμενων συχνοτήτων ως συνάρτηση του πλάτους της τροποποίησης, $\delta|\omega_0|(a^{(k)})$. Διαφορετικά χρώματα αντιπροσωπεύουν διαφορετικούς χρόνους εκκίνησης της προσαρμογής.

Παρατηρήστε τις δύο συμπεριφορές του σχετικού σφάλματος. Η πρώτη είναι ότι μειώνεται καθώς αυξάνεται ο χρόνος εκκίνησης, γεγονός που είχε παρατηρηθεί ήδη στην περίπτωση GR του προηγούμενου κεφαλαίου (ειδικότερα, δείτε την Εικόνα 6.10). Η δεύτερη τάση είναι ότι τα μικρότερα σχετικά σφάλματα επιτυγχάνονται κοντά στο $a^{(k)} \simeq 0$, όπου η τροποποίηση είναι μικρή. Αυτό υποδηλώνει ότι η PF λειτουργεί καλύτερα σε αυτή την περιοχή, καθώς οι προβλέψεις της είναι πιο κοντά σε αυτές που εξάγονται από την χρονική εξέλιξη. Αυτό είναι αναμενόμενο, καθώς τα μικρά πλάτη παράγουν μικρότερη απόκλιση από την GR, επομένως η συνθήκη (4.4) εκπληρώνεται πιο αποτελεσματικά.

Οι επόμενες δύο Εικόνες ?? έχουν επίσης την ίδια διάταξη και δείχνουν το πλάτος και τη φάση της θεμελιώδους συχνότητας ως συνάρτηση του πλάτους της τροποποίησης $a^{(k)}$ (αριστερά) και το πλάτος και τους πόλους της ουράς (δεξιά).

Παρατηρήστε ότι το πλάτος και η φάση της συχνότητας τροποποιούνται διαφορετικά. Για αρνητικά $a^{(k)}$, το πλάτος μειώνεται και η φάση αυξάνεται σε σχέση με την τιμή της GR (στο

$a^{(k)} = 0$), και αντιστρόφως για θετικά πλάτη. Επίσης, η διαφορά τους από την τιμή της GR ($a^{(k)} = 0$) ελαττώνεται καθώς αυξάνεται το k . Αυτό είναι αναμενόμενο, διότι μια συγκεκριμένη τιμή του $a^{(k)}$ εισάγει μικρότερη τροποποίηση για μεγάλο k από ότι για μικρό.

Στη δεξιά εικόνα βλέπουμε ότι για ένα δεδομένο πλάτος τροποποίησης, οι παράμετροι της ουράς είναι οι ίδιες για όλες τις δυνάμεις του k , εκτός από το $k = 2$. Ο λόγος για αυτή τη διαφωνία είναι ότι ο εκθέτης για όλες τις προσαρμογές της ουράς διατηρήθηκε σταθερός και ίσος με -7 . Ωστόσο, η τροποποίηση $k = 2$ τροποποιεί αυτόν τον εκθέτη ως συνάρτηση του πλάτους της, επομένως χρησιμοποιήσαμε το λανθασμένο μοντέλο για αυτή τη δύναμη τροποποίησης και το κάναμε για χάρη της σύγκρισης μεταξύ όλων των διαφορετικών τροποποιήσεων. Παρατηρήστε ότι για όλες τις άλλες τιμές του k οι ίδιες ουρές βρίσκονται με συνέπεια.

Η επόμενη Εικόνα 7.5 έχει ως σκοπό να απεικονίσει την απόκλιση των παραμέτρων από την τιμή GR. Και πάλι, κάθε στήλη αναφέρεται σε διαφορετικές τιμές του $k \in [2, 7]$ και οι οριζόντιοι άξονες είναι τα πλάτη. Στους κατακόρυφους άξονες, απεικονίζουμε με διαφορετικά χρώματα τις παραμέτρους που προσαρμόστηκαν σε σχέση με τις αντίστοιχες τιμές τους στην GR. Παρατηρούμε ότι για το μικρότερο k (μεγαλύτερη τροποποίηση), οι παράμετροι αλλάζουν περισσότερο. Στη συνέχεια, καθώς το k αυξάνεται, η τροποποίηση μειώνεται με τον ίδιο τρόπο για τις τρεις παραμέτρους, $Re(\omega_0)$, A_0 , ϕ_0 . Ο φανταστικός μέρος παρουσιάζει διαφορετική συμπεριφορά και η τροποποίησή του είναι μεγαλύτερη για μεγαλύτερο k .

Οι στερεές γραμμές που εμφανίζονται στις προηγούμενες εικόνες προέρχονται από την προσαρμογή των σημείων του ίδιου χρώματος. Η προσαρμογή χρησιμοποιεί κυβικά πολυώνυμα $f(a^{(k)}) = \beta \cdot (a^{(k)})^3 + \gamma \cdot (a^{(k)})^2 + \delta \cdot (a^{(k)}) + \epsilon$. Η Εικόνα 7.6 δείχνει αυτούς τους συντελεστές ως συνάρτηση του k για όλες τις παραμέτρους της θεμελιώδους λειτουργίας. Όπως βλέπουμε, οι κυβικοί συντελεστές β είναι σχεδόν μηδενικοί για όλες τις παραμέτρους και το k . Επίσης, για όλες τις παραμέτρους, εκτός από τον πραγματικό μέρος, ο τετραγωνικός συντελεστής γ είναι μη μηδενικός και για όλους αυτούς ο γραμμικός συντελεστής δ είναι μη μηδενικός. Αυτό σημαίνει ότι για τα πλάτη της τροποποίησης που επιλέξαμε, η διόρθωση σε όλες τις παραμέτρους είναι τετραγωνική, ενώ για τον πραγματικό μέρος είναι γραμμική. Γι' αυτό το λόγο στην Εικόνα 7.3 το σχετικό σφάλμα του πραγματικού μέρους είναι μικρότερο από το αντίστοιχο του φανταστικού.

BIBLIOGRAPHY

- [1] A. Einstein, 'Die Feldgleichungen der Gravitation,' *Sitzungsberichte der Königlich Preussischen Akademie der Wissenschaften*, pp. 844–847, Jan. 1915.
- [2] H. Kragh, *Quantum Generations: A History of Physics in the Twentieth Century* (Book collections on Project MUSE). Princeton University Press, 2002, ISBN: 9780691095523. [Online]. Available: <https://books.google.gr/books?id=ELrFDIldlawC>.
- [3] C. M. Will, 'The Confrontation between General Relativity and Experiment,' *Living Rev. Rel.*, vol. 17, p. 4, 2014. DOI: [10.12942/lrr-2014-4](https://doi.org/10.12942/lrr-2014-4). arXiv: [1403.7377](https://arxiv.org/abs/1403.7377) [gr-qc].
- [4] S. M. Carroll, *Spacetime and Geometry: An Introduction to General Relativity*. Cambridge University Press, 2019.
- [5] M. Hobson, G. Efstathiou and A. Lasenby, *General Relativity: An Introduction for Physicists* (General Relativity: An Introduction for Physicists). Cambridge University Press, 2006, ISBN: 9780521829519.
- [6] K. Sfetsos, *General theory of relativity: Notes in brief*, 2024.
- [7] N. Chatzifiotis and E. Papantonopoulos, *General relativity notes*.
- [8] D. Tong, *General relativity, university of cambridge part iii mathematical tripos*. [Online]. Available: <https://www.damtp.cam.ac.uk/user/tong/gr.html>.
- [9] V. Ferrari, L. Gualtieri and P. Pani, *General Relativity and its Applications: Black Holes, Compact Stars and Gravitational Waves*. CRC Press, 2020, ISBN: 9780429957802.
- [10] C. Bambi, 'Astrophysical Black Holes: A Review,' *PoS*, vol. MULTIF2019, p. 028, 2020. DOI: [10.22323/1.362.0028](https://doi.org/10.22323/1.362.0028). arXiv: [1906.03871](https://arxiv.org/abs/1906.03871) [astro-ph.HE].
- [11] R. P. Kerr, 'Gravitational field of a spinning mass as an example of algebraically special metrics,' *Phys. Rev. Lett.*, vol. 11, pp. 237–238, 5 1963. DOI: [10.1103/PhysRevLett.11.237](https://doi.org/10.1103/PhysRevLett.11.237). [Online]. Available: <https://link.aps.org/doi/10.1103/PhysRevLett.11.237>.
- [12] C. Bambi, 'Testing the Kerr black hole hypothesis,' *Mod. Phys. Lett. A*, vol. 26, pp. 2453–2468, 2011. DOI: [10.1142/S0217732311036929](https://doi.org/10.1142/S0217732311036929). arXiv: [1109.4256](https://arxiv.org/abs/1109.4256) [gr-qc].
- [13] K. Schwarzschild, 'Über das Gravitationsfeld eines Massenpunktes nach der Einsteinschen Theorie,' *Sitzungsberichte der Königlich Preussischen Akademie der Wissenschaften*, pp. 189–196, Jan. 1916.
- [14] B. S. Sathyaprakash and B. F. Schutz, 'Physics, astrophysics and cosmology with gravitational waves,' *Living Reviews in Relativity*, vol. 12, no. 1, Mar. 2009, ISSN: 1433-8351. DOI: [10.12942/lrr-2009-2](https://doi.org/10.12942/lrr-2009-2). [Online]. Available: <http://dx.doi.org/10.12942/lrr-2009-2>.
- [15] B. P. Abbott *et al.*, 'GW170817: Observation of Gravitational Waves from a Binary Neutron Star Inspiral,' *Phys. Rev. Lett.*, vol. 119, no. 16, p. 161101, 2017. DOI: [10.1103/PhysRevLett.119.161101](https://doi.org/10.1103/PhysRevLett.119.161101). arXiv: [1710.05832](https://arxiv.org/abs/1710.05832) [gr-qc].
- [16] A. Goldstein *et al.*, 'An Ordinary Short Gamma-Ray Burst with Extraordinary Implications: Fermi-GBM Detection of GRB 170817A,' *Astrophys. J. Lett.*, vol. 848, no. 2, p. L14, 2017. DOI: [10.3847/2041-8213/aa8f41](https://doi.org/10.3847/2041-8213/aa8f41). arXiv: [1710.05446](https://arxiv.org/abs/1710.05446) [astro-ph.HE].
- [17] D. A. Coulter *et al.*, 'Swope Supernova Survey 2017a (SSS17a), the Optical Counterpart to a Gravitational Wave Source,' *Science*, vol. 358, p. 1556, 2017. DOI: [10.1126/science.aap9811](https://doi.org/10.1126/science.aap9811). arXiv: [1710.05452](https://arxiv.org/abs/1710.05452) [astro-ph.HE].
- [18] C. Cutler and K. S. Thorne, *An overview of gravitational-wave sources*, 2002. arXiv: [gr-qc/0204090](https://arxiv.org/abs/gr-qc/0204090) [gr-qc]. [Online]. Available: <https://arxiv.org/abs/gr-qc/0204090>.
- [19] [Online]. Available: https://www.esa.int/Science_Exploration/Space_Science/LISA/Capturing_the_ripples_of_spacetime_LISA_gets_go-ahead.
- [20] M. C. *et al.*, *Lisa definition study report*, 2024. arXiv: [2402.07571](https://arxiv.org/abs/2402.07571) [astro-ph.CO]. [Online]. Available: <https://arxiv.org/abs/2402.07571>.
- [21] B. e. A. Abbott, 'Observation of gravitational waves from a binary black hole merger,' *Physical Review Letters*, vol. 116, no. 6, Feb. 2016, ISSN: 1079-7114. DOI: [10.1103/physrevlett.116.061102](https://doi.org/10.1103/physrevlett.116.061102). [Online]. Available: <http://dx.doi.org/10.1103/PhysRevLett.116.061102>.

- [22] M. Maggiore, *Gravitational Waves: Volume 1: Theory and Experiments* (Gravitational Waves). OUP Oxford, 2008, ISBN: 9780198570745.
- [23] A. Buonanno, *Gravitational waves*, 2007. arXiv: 0709.4682 [gr-qc]. [Online]. Available: <https://arxiv.org/abs/0709.4682>.
- [24] D. Buskirk and M. C. B. Hamilton, 'A complete analytic gravitational wave model for undergraduates,' *European Journal of Physics*, vol. 40, no. 2, p. 025603, Jan. 2019, ISSN: 1361-6404. DOI: 10.1088/1361-6404/aaf81e. [Online]. Available: <http://dx.doi.org/10.1088/1361-6404/aaf81e>.
- [25] R. M. Wald, *Introduction to gravitational self-force*, 2009. arXiv: 0907.0412 [gr-qc]. [Online]. Available: <https://arxiv.org/abs/0907.0412>.
- [26] A. Buonanno and T. Damour, 'Effective one-body approach to general relativistic two-body dynamics,' *Physical Review D*, vol. 59, no. 8, Mar. 1999, ISSN: 1089-4918. DOI: 10.1103/physrevd.59.084006. [Online]. Available: <http://dx.doi.org/10.1103/PhysRevD.59.084006>.
- [27] A. Ashtekar, B. Berger, J. Isenberg and M. MacCallum, *General Relativity and Gravitation: A Centennial Perspective*. Cambridge University Press, 2015, ISBN: 9781107037311. [Online]. Available: <https://books.google.gr/books?id=qZXwCAAQBAJ>.
- [28] O. Dreyer, B. Kelly, B. Krishnan, L. S. Finn, D. Garrison and R. Lopez-Aleman, 'Black-hole spectroscopy: Testing general relativity through gravitational-wave observations,' *Classical and Quantum Gravity*, vol. 21, no. 4, 787–803, Jan. 2004, ISSN: 1361-6382. DOI: 10.1088/0264-9381/21/4/003. [Online]. Available: <http://dx.doi.org/10.1088/0264-9381/21/4/003>.
- [29] N. Franchini and S. H. Völkel, 'Testing General Relativity with Black Hole Quasi-Normal Modes,' May 2023. arXiv: 2305.01696 [gr-qc].
- [30] M. Maggiore, *Gravitational Waves* (Gravitational Waves τ . 2). Oxford University Press, 2008, ISBN: 9780198570899.
- [31] T. Regge and J. A. Wheeler, 'Stability of a schwarzschild singularity,' *Phys. Rev.*, vol. 108, pp. 1063–1069, 4 1957. DOI: 10.1103/PhysRev.108.1063. [Online]. Available: <https://link.aps.org/doi/10.1103/PhysRev.108.1063>.
- [32] F. J. Zerilli, 'Gravitational field of a particle falling in a schwarzschild geometry analyzed in tensor harmonics,' *Phys. Rev. D*, vol. 2, pp. 2141–2160, 10 1970. DOI: 10.1103/PhysRevD.2.2141. [Online]. Available: <https://link.aps.org/doi/10.1103/PhysRevD.2.2141>.
- [33] F. J. Zerilli, 'Effective potential for even-parity regge-wheeler gravitational perturbation equations,' *Phys. Rev. Lett.*, vol. 24, pp. 737–738, 13 1970. DOI: 10.1103/PhysRevLett.24.737. [Online]. Available: <https://link.aps.org/doi/10.1103/PhysRevLett.24.737>.
- [34] D. Griffiths and D. Schroeter, *Introduction to Quantum Mechanics*. Cambridge University Press, 2019, ISBN: 9781108103145. [Online]. Available: <https://books.google.gr/books?id=zU3bDwAAQBAJ>.
- [35] D. J. Griffiths, *Introduction to Electrodynamics*, 4th ed. Cambridge University Press, 2017.
- [36] C. V. Vishveshwara, 'Scattering of Gravitational Radiation by a Schwarzschild Black-hole,' *Nature*, vol. 227, pp. 936–938, 1970. DOI: 10.1038/227936a0.
- [37] C. V. Vishveshwara, 'Stability of the schwarzschild metric,' *Phys. Rev. D*, vol. 1, pp. 2870–2879, 10 1970. DOI: 10.1103/PhysRevD.1.2870. [Online]. Available: <https://link.aps.org/doi/10.1103/PhysRevD.1.2870>.
- [38] B. S. Kay and R. M. Wald, 'Linear stability of schwarzschild under perturbations which are non-vanishing on the bifurcation 2-sphere,' *Classical and Quantum Gravity*, vol. 4, no. 4, p. 893, 1987. DOI: 10.1088/0264-9381/4/4/022. [Online]. Available: <https://dx.doi.org/10.1088/0264-9381/4/4/022>.
- [39] P. J. Nee, S. H. Völkel and H. P. Pfeiffer, 'Role of black hole quasinormal mode overtones for ringdown analysis,' *Phys. Rev. D*, vol. 108, no. 4, p. 044032, 2023. DOI: 10.1103/PhysRevD.108.044032. arXiv: 2302.06634 [gr-qc].
- [40] V. Baibhav, M. H.-Y. Cheung, E. Berti, V. Cardoso, G. Carullo, R. Cotesta, W. Del Pozzo and F. Duque, 'Agnostic black hole spectroscopy: Quasinormal mode content of numerical relativity waveforms and limits of validity of linear perturbation theory,' *Phys. Rev. D*, vol. 108, no. 10, p. 104020, 2023. DOI: 10.1103/PhysRevD.108.104020. arXiv: 2302.03050 [gr-qc].
- [41] M. Giesler, M. Isi, M. A. Scheel and S. Teukolsky, 'Black Hole Ringdown: The Importance of Overtones,' *Phys. Rev. X*, vol. 9, no. 4, p. 041060, 2019. DOI: 10.1103/PhysRevX.9.041060. arXiv: 1903.08284 [gr-qc].
- [42] H.-P. Nollert, 'Quasinormal modes: The characteristic 'sound' of black holes and neutron stars,' *Classical and Quantum Gravity*, vol. 16, no. 12, R159, 1999. DOI: 10.1088/0264-9381/16/12/201. [Online]. Available: <https://dx.doi.org/10.1088/0264-9381/16/12/201>.

- [43] H. Pain, *The Physics of Vibrations and Waves*. Wiley, 1983, ISBN: 9780471901815. [Online]. Available: https://books.google.gr/books?id=_iN0AQAAIAAJ.
- [44] M. Kac, 'Can one hear the shape of a drum?' *The American Mathematical Monthly*, vol. 73, no. 4, pp. 1–23, 1966, issn: 00029890, 19300972. [Online]. Available: <http://www.jstor.org/stable/2313748> (visited on 23/10/2024).
- [45] K. D. Kokkotas and B. G. Schmidt, 'Quasinormal modes of stars and black holes,' *Living Rev. Rel.*, vol. 2, p. 2, 1999. doi: [10.12942/lrr-1999-2](https://doi.org/10.12942/lrr-1999-2). arXiv: [gr-qc/9909058](https://arxiv.org/abs/gr-qc/9909058).
- [46] S. Chandrasekhar, *The Mathematical Theory of Black Holes* (International series of monographs on physics). Clarendon Press, 1998, ISBN: 9780198503705. [Online]. Available: <https://books.google.gr/books?id=LBOVcrzFfhsC>.
- [47] R. A. Konoplya and A. Zhidenko, 'Quasinormal modes of black holes: From astrophysics to string theory,' *Rev. Mod. Phys.*, vol. 83, pp. 793–836, 2011. doi: [10.1103/RevModPhys.83.793](https://doi.org/10.1103/RevModPhys.83.793). arXiv: [1102.4014](https://arxiv.org/abs/1102.4014) [gr-qc].
- [48] N. Andersson, 'Evolving test fields in a black-hole geometry,' *Physical Review D*, vol. 55, no. 2, 468–479, Jan. 1997, issn: 1089-4918. doi: [10.1103/physrevd.55.468](https://doi.org/10.1103/physrevd.55.468). [Online]. Available: <http://dx.doi.org/10.1103/PhysRevD.55.468>.
- [49] H.-P. Nollert and R. H. Price, 'Quantifying excitations of quasinormal mode systems,' *J. Math. Phys.*, vol. 40, pp. 980–1010, 1999. doi: [10.1063/1.532698](https://doi.org/10.1063/1.532698). arXiv: [gr-qc/9810074](https://arxiv.org/abs/gr-qc/9810074).
- [50] E. S. C. Ching, P. T. Leung, W. M. Suen and K. Young, 'Wave propagation in gravitational systems: Completeness of quasinormal modes,' *Physical Review D*, vol. 54, no. 6, 3778–3791, Sep. 1996, issn: 1089-4918. doi: [10.1103/physrevd.54.3778](https://doi.org/10.1103/physrevd.54.3778). [Online]. Available: <http://dx.doi.org/10.1103/PhysRevD.54.3778>.
- [51] V. P. Frolov and I. D. Novikov, *Black Hole Physics: Basic Concepts and New Developments* (Fundamental Theories of Physics), 1st ed. Dordrecht: Springer Dordrecht, 1998, vol. 96, pp. XXI, 770. doi: [10.1007/978-94-011-5139-9](https://doi.org/10.1007/978-94-011-5139-9).
- [52] R. H. Price, 'Nonspherical perturbations of relativistic gravitational collapse. i. scalar and gravitational perturbations,' *Phys. Rev. D*, vol. 5, pp. 2419–2438, 10 1972. doi: [10.1103/PhysRevD.5.2419](https://doi.org/10.1103/PhysRevD.5.2419). [Online]. Available: <https://link.aps.org/doi/10.1103/PhysRevD.5.2419>.
- [53] E. S. C. Ching, P. T. Leung, W. M. Suen and K. Young, 'Wave propagation in gravitational systems: Late time behavior,' *Phys. Rev. D*, vol. 52, pp. 2118–2132, 4 1995. doi: [10.1103/PhysRevD.52.2118](https://doi.org/10.1103/PhysRevD.52.2118). [Online]. Available: <https://link.aps.org/doi/10.1103/PhysRevD.52.2118>.
- [54] C. Molina, P. Pani, V. Cardoso and L. Gualtieri, 'Gravitational signature of Schwarzschild black holes in dynamical Chern-Simons gravity,' *Phys. Rev. D*, vol. 81, p. 124021, 2010. doi: [10.1103/PhysRevD.81.124021](https://doi.org/10.1103/PhysRevD.81.124021). arXiv: [1004.4007](https://arxiv.org/abs/1004.4007) [gr-qc].
- [55] S. Chandrasekhar and S. L. Detweiler, 'The quasi-normal modes of the Schwarzschild black hole,' *Proc. Roy. Soc. Lond. A*, vol. 344, pp. 441–452, 1975. doi: [10.1098/rspa.1975.0112](https://doi.org/10.1098/rspa.1975.0112).
- [56] E. W. Leaver, 'An Analytic representation for the quasi normal modes of Kerr black holes,' *Proc. Roy. Soc. Lond. A*, vol. 402, pp. 285–298, 1985. doi: [10.1098/rspa.1985.0119](https://doi.org/10.1098/rspa.1985.0119).
- [57] E. Berti, V. Cardoso and A. O. Starinets, 'Quasinormal modes of black holes and black branes,' *Class. Quant. Grav.*, vol. 26, p. 163001, 2009. doi: [10.1088/0264-9381/26/16/163001](https://doi.org/10.1088/0264-9381/26/16/163001). arXiv: [0905.2975](https://arxiv.org/abs/0905.2975) [gr-qc].
- [58] B. F. Schutz and C. M. Will, 'Black hole normal modes - a semianalytic approach,' *The Astrophysical Journal*, vol. 291, 1985. [Online]. Available: <https://api.semanticscholar.org/CorpusID:123084825>.
- [59] R. A. Konoplya, 'Quasinormal behavior of the d-dimensional Schwarzschild black hole and higher order WKB approach,' *Phys. Rev. D*, vol. 68, p. 024018, 2003. doi: [10.1103/PhysRevD.68.024018](https://doi.org/10.1103/PhysRevD.68.024018). arXiv: [gr-qc/0303052](https://arxiv.org/abs/gr-qc/0303052).
- [60] B. Mashhoon, 'Quasinormal modes of a black hole,' in *3rd Marcel Grossmann Meeting on the Recent Developments of General Relativity*, 1982.
- [61] V. Ferrari and B. Mashhoon, 'Oscillations of a black hole,' *Phys. Rev. Lett.*, vol. 52, pp. 1361–1364, 16 1984. doi: [10.1103/PhysRevLett.52.1361](https://doi.org/10.1103/PhysRevLett.52.1361). [Online]. Available: <https://link.aps.org/doi/10.1103/PhysRevLett.52.1361>.
- [62] S. Flügge, *Practical Quantum Mechanics* (Classics in Mathematics). Springer Berlin Heidelberg, 2012, ISBN: 9783642619953. [Online]. Available: <https://books.google.gr/books?id=Md5sCQAQBAJ>.
- [63] L. Barack *et al.*, 'Black holes, gravitational waves and fundamental physics: a roadmap,' *Class. Quant. Grav.*, vol. 36, no. 14, p. 143001, 2019. doi: [10.1088/1361-6382/ab0587](https://doi.org/10.1088/1361-6382/ab0587). arXiv: [1806.05195](https://arxiv.org/abs/1806.05195) [gr-qc].

- [64] S. Shankaranarayanan and J. P. Johnson, ‘Modified theories of gravity: Why, how and what?’ *Gen. Rel. Grav.*, vol. 54, no. 5, p. 44, 2022. doi: [10.1007/s10714-022-02927-2](https://doi.org/10.1007/s10714-022-02927-2). arXiv: [2204.06533](https://arxiv.org/abs/2204.06533) [gr-qc].
- [65] E. Berti *et al.*, ‘Testing General Relativity with Present and Future Astrophysical Observations,’ *Class. Quant. Grav.*, vol. 32, p. 243001, 2015. doi: [10.1088/0264-9381/32/24/243001](https://doi.org/10.1088/0264-9381/32/24/243001). arXiv: [1501.07274](https://arxiv.org/abs/1501.07274) [gr-qc].
- [66] V. Cardoso, M. Kimura, A. Maselli, E. Berti, C. F. B. Macedo and R. McManus, ‘Parametrized black hole quasinormal ringdown: Decoupled equations for nonrotating black holes,’ *Phys. Rev. D*, vol. 99, no. 10, p. 104077, 2019. doi: [10.1103/PhysRevD.99.104077](https://doi.org/10.1103/PhysRevD.99.104077). arXiv: [1901.01265](https://arxiv.org/abs/1901.01265) [gr-qc].
- [67] R. McManus, E. Berti, C. F. B. Macedo, M. Kimura, A. Maselli and V. Cardoso, ‘Parametrized black hole quasinormal ringdown. II. Coupled equations and quadratic corrections for nonrotating black holes,’ *Phys. Rev. D*, vol. 100, no. 4, p. 044061, 2019. doi: [10.1103/PhysRevD.100.044061](https://doi.org/10.1103/PhysRevD.100.044061). arXiv: [1906.05155](https://arxiv.org/abs/1906.05155) [gr-qc].
- [68] P. A. Cano, L. Capuano, N. Franchini, S. Maenaut and S. H. Völkel, ‘A parametrized quasi-normal mode framework for modified Teukolsky equations,’ Jul. 2024. arXiv: [2407.15947](https://arxiv.org/abs/2407.15947) [gr-qc].
- [69] D. Lovelock, ‘The four-dimensionality of space and the einstein tensor,’ *J. Math. Phys.*, vol. 13, pp. 874–876, 1972. doi: [10.1063/1.1666069](https://doi.org/10.1063/1.1666069).
- [70] S. H. Völkel, N. Franchini and E. Barausse, ‘Theory-agnostic reconstruction of potential and couplings from quasinormal modes,’ *Phys. Rev. D*, vol. 105, no. 8, p. 084046, 2022. doi: [10.1103/PhysRevD.105.084046](https://doi.org/10.1103/PhysRevD.105.084046). arXiv: [2202.08655](https://arxiv.org/abs/2202.08655) [gr-qc].
- [71] N. Franchini and S. H. Völkel, ‘Parametrized quasinormal mode framework for non-schwarzschild metrics,’ *Physical Review D*, vol. 107, no. 12, Jun. 2023, issn: 2470-0029. doi: [10.1103/physrevd.107.124063](https://doi.org/10.1103/physrevd.107.124063). [Online]. Available: <http://dx.doi.org/10.1103/PhysRevD.107.124063>.
- [72] S. Alexander and N. Yunes, ‘Chern-Simons Modified General Relativity,’ *Phys. Rept.*, vol. 480, pp. 1–55, 2009. doi: [10.1016/j.physrep.2009.07.002](https://doi.org/10.1016/j.physrep.2009.07.002). arXiv: [0907.2562](https://arxiv.org/abs/0907.2562) [hep-th].
- [73] V. Cardoso and L. Gualtieri, ‘Perturbations of Schwarzschild black holes in Dynamical Chern-Simons modified gravity,’ *Phys. Rev. D*, vol. 80, p. 064008, 2009, [Erratum: *Phys.Rev.D* 81, 089903 (2010)]. doi: [10.1103/PhysRevD.81.089903](https://doi.org/10.1103/PhysRevD.81.089903). arXiv: [0907.5008](https://arxiv.org/abs/0907.5008) [gr-qc].
- [74] R. Burden, J. Faires and A. Burden, *Numerical Analysis*. Cengage Learning, 2015, isbn: 9781305465350. [Online]. Available: <https://books.google.de/books?id=9DV-BAAAQBAJ>.
- [75] W. Press, *Numerical Recipes 3rd Edition: The Art of Scientific Computing* (Numerical Recipes: The Art of Scientific Computing). Cambridge University Press, 2007, isbn: 9780521880688. [Online]. Available: <https://books.google.de/books?id=1aA0dzK3FegC>.
- [76] K. Madsen, H. Nielsen and O. Tingleff, *Methods for Non-Linear Least Squares Problems (2nd ed.)* English. 2004.
- [77] [Online]. Available: <https://pages.jh.edu/eberti2/ringdown/>.
- [78] E. Berti, V. Cardoso, J. A. Gonzalez, U. Sperhake, M. Hannam, S. Husa and B. Bruegmann, ‘Inspiral, merger and ringdown of unequal mass black hole binaries: A Multipolar analysis,’ *Phys. Rev. D*, vol. 76, p. 064034, 2007. doi: [10.1103/PhysRevD.76.064034](https://doi.org/10.1103/PhysRevD.76.064034). arXiv: [gr-qc/0703053](https://arxiv.org/abs/gr-qc/0703053).
- [79] S. H. Völkel, ‘On the Gravitational Wave Spectrum of Compact Relativistic Objects,’ Ph.D. dissertation, U. Tübingen, 2020. doi: [10.15496/publikation-42527](https://doi.org/10.15496/publikation-42527).
- [80] A. Ashtekar, B. Berger, J. Isenberg and M. MacCallum, *General Relativity and Gravitation: A Centennial Perspective*. Cambridge University Press, 2015, isbn: 9781107037311. [Online]. Available: <https://books.google.gr/books?id=qZXwCAAQBAJ>.
- [81] H. R. Beyer, ‘On the completeness of the quasinormal modes of the pöschl-teller potential,’ *Communications in Mathematical Physics*, vol. 204, no. 2, 397–423, Jul. 1999, issn: 1432-0916. doi: [10.1007/s002200050651](https://doi.org/10.1007/s002200050651). [Online]. Available: <http://dx.doi.org/10.1007/s002200050651>.
- [82] A. F. Cardona and C. Molina, ‘Quasinormal modes of generalized pöschl–teller potentials,’ *Classical and Quantum Gravity*, vol. 34, no. 24, p. 245002, Nov. 2017, issn: 1361-6382. doi: [10.1088/1361-6382/aa9428](https://doi.org/10.1088/1361-6382/aa9428). [Online]. Available: <http://dx.doi.org/10.1088/1361-6382/aa9428>.
- [83] R. H. Price, ‘Nonspherical perturbations of relativistic gravitational collapse. ii. integer-spin, zero-rest-mass fields,’ *Phys. Rev. D*, vol. 5, pp. 2439–2454, 10 1972. doi: [10.1103/PhysRevD.5.2439](https://doi.org/10.1103/PhysRevD.5.2439). [Online]. Available: <https://link.aps.org/doi/10.1103/PhysRevD.5.2439>.
- [84] P. Wagle, N. Yunes and H. O. Silva, ‘Quasinormal modes of slowly-rotating black holes in dynamical Chern-Simons gravity,’ *Phys. Rev. D*, vol. 105, no. 12, p. 124003, 2022. doi: [10.1103/PhysRevD.105.124003](https://doi.org/10.1103/PhysRevD.105.124003). arXiv: [2103.09913](https://arxiv.org/abs/2103.09913) [gr-qc].

- [85] S. Iyer and C. M. Will, 'Black-hole normal modes: A wkb approach. i. foundations and application of a higher-order wkb analysis of potential-barrier scattering,' *Phys. Rev. D*, vol. 35, pp. 3621–3631, 12 1987. doi: [10.1103/PhysRevD.35.3621](https://doi.org/10.1103/PhysRevD.35.3621). [Online]. Available: <https://link.aps.org/doi/10.1103/PhysRevD.35.3621>.
- [86] S. H. Völkel, 'Quasinormal modes from bound states: The numerical approach,' *Phys. Rev. D*, vol. 106, no. 12, p. 124009, 2022. doi: [10.1103/PhysRevD.106.124009](https://doi.org/10.1103/PhysRevD.106.124009). arXiv: [2210.02069](https://arxiv.org/abs/2210.02069) [gr-qc].
- [87] B. P. t. Abbott, 'Observation of gravitational waves from a binary black hole merger,' *Phys. Rev. Lett.*, vol. 116, p. 061102, 6 2016. doi: [10.1103/PhysRevLett.116.061102](https://doi.org/10.1103/PhysRevLett.116.061102). [Online]. Available: <https://link.aps.org/doi/10.1103/PhysRevLett.116.061102>.
- [88] K. D. et al., *Laser interferometer space antenna*, 2017. arXiv: [1702.00786](https://arxiv.org/abs/1702.00786) [astro-ph.IM]. [Online]. Available: <https://arxiv.org/abs/1702.00786>.
- [89] P. Pani, 'Advanced Methods in Black-Hole Perturbation Theory,' *Int. J. Mod. Phys. A*, vol. 28, V. Cardoso, L. Gualtieri, C. Herdeiro and U. Sperhake, Eds., p. 1340018, 2013. doi: [10.1142/S0217751X13400186](https://doi.org/10.1142/S0217751X13400186). arXiv: [1305.6759](https://arxiv.org/abs/1305.6759) [gr-qc].

COLOPHON

This thesis was authored using Overleaf² and typeset based on the La Trobe PhD Thesis Template³ (customization of the classicthesis⁴ L^AT_EX template),

² <https://www.overleaf.com/>

³ <https://github.com/bashimao/ltu-thesis>

⁴ <https://bitbucket.org/amiede/classicthesis>